FATIGUE BEHAVIOUR OF FORGED BEPM TI-6AL-4V

FATIGUE BEHAVIOUR OF FORGED TI-6AL-4V MADE FROM BLENDED ELEMENT POWDER METALLURGY

By NOEL HAYNES, B. ENG

A Thesis Submitted to the School of Graduate Studies in

Partial Fulfilment of the Requirements for the

Degree of Master of Applied Science

McMaster University

McMaster University MASTER OF APPLIED SCIENCE (2016)

Hamilton, Ontario (Materials Science and Engineering)

TITLE: Fatigue Behaviour of Forged Ti-6Al-4V Made From Blended Element Powder Metallurgy

AUTHOR: Noel Haynes, B. Eng (McMaster University)

SUPERVISOR: Dr. Hatem S. Zurob

NUMBER OF PAGES: xix, 110

Lay Abstract

The mechanical properties of a metal are dictated primarily by the metal's microstructure. The microstructure of a metal made from metal powder that has been pressed and heated to bind the powder together generally contains residual porosity. This generally leads to a reduction in metal fatigue resistance versus a metal that is pore-free.

In studying metal fatigue of a titanium alloy made from metal powder, the resistance to metal fatigue varied considerably and did not achieve the same resistance of pore-free material, despite the titanium alloy in question being nearly pore-free. This titanium alloy was studied to determine what the cause of the poor metal fatigue resistance was. Through a methodical testing program, it was determined that volume fraction of a particular crystalline phase in the microstructure was more damaging than the pores themselves.

Abstract

A detailed metallurgical analysis was conducted to correlate microstructure to axial strain-controlled high cycle fatigue of Ti-6Al-4V forgings made from cold isostatic pressed and sintered preforms of blended element powder metallurgy (BEPM) incorporating hydrogenated titanium. Analysis included fractographic examination by SEM, microstructure examination by optical microscopy, texture examination via EBSD, chemical analysis and fatigue strain mapping via digital image correlation (DIC). From a literature review and observations of findings, factors that were of primary concern were: maximum pore diameter, primary α volume fraction, primary α width, primary α particle count, oxygen equivalency (*OE*) and texture of the α phase.

The primary α volume fraction was found to have the single most influential effect on fatigue, whereby decreasing volume fraction increased fatigue life. Using statistical analysis, multivariable regression analyses were performed to evaluate combinations of predictors on fatigue life. The resulting outcome of volume fraction and maximum pore diameter, having a 3.3 to 1 weighting, was the most significant at predicting the fatigue response. Improving fatigue life of forged Ti-6Al-4V made from BEPM should thus be primarily focused on microstructure refinement. It is suggested future experimentation also consider the effects of the number of primary α particles and OE when modeling fatigue strength.

Acknowledgements

I would like to thank my supervisor Dr. Hatem Zurob for his expertise and encouragement. A great deal of thanks goes to my mentor at UTC Aerospace Systems, Dr. Roque Panza-Giosa, for his technical expertise and support. Additionally, I thank UTC Aerospace Systems for providing financial support, and my colleagues at UTC Aerospace Systems, especially Ben Evans, for the opportunity to perform this work. I also thank Dr. Vladimir Duz at ADMA Products for his insight on research activities in this field of study. I extend my gratitude to my peers at McMaster University and those who assisted with laboratory testing. Most importantly, to my loving and supportive wife Natalia.

Table of Contents

List of Figures

List of Tables

List of Appendices

List of Abbreviations and Symbols

α	Alpha
α’	Alpha prime
α’’	Alpha double prime
Al Eq.	Aluminum equivalent
β	Beta
β’	Beta prime
BE	Blended element
BEPM	Blended element powder metallurgy
BCC	Body centered cubic
DIC	Digital Image Correlation
F	Shape factor
GA	Gas atomized (GA)
GB_α	Grain boundary alpha
HCF	High cycle fatigue
HCP	Hexagonal close packed
HDH	Hydride-dehydride
HIP	Hot isostatic pressed
IM	Ingot material
IQR	Inter quartile range
Ksi	Kilopound per square inch
k_t	Stress concentration

L	Longitudinal grain direction
LT	Long-transverse grain direction
Mo Eq.	Molybdenum equivalent
MPa	Megapascal
M_s	Martensitic-start temperature
ω	Omega
OEE	Other element, each
OE	Oxygen equivalency
PM	Powder metallurgy
PREP	Plasma rotating electrode process
R	Stress ratio
Ra	Mean surface roughness
R.T.	Room temperature
STA	Solution treated and aged
STOA	Solution treated and over aged
TOE	Other element, total
µin	Micro-inch
µm	Micro-meter
V_f	Volume fraction

Declaration of Academic Achievement

The named author is the primary author of this thesis. Contributions included: hypothesis, literature review, project definition, administering various supporting laboratories, metallurgical analysis, analyzing of data and presentation of results, including figures.

This thesis was prepared under the supervision of Dr. Hatem Zurob, supervisor at McMaster University, and Dr. Roque Panza-Giosa, consultant at United Technologies Aerospace Systems – Landing Systems (UTAS-LS). Dr. Vladimir Duz, Director of Research & Development at ADMA Products Inc., provided the relevant conference proceedings. Fatigue testing and chemical analysis were outsourced to laboratories that serve the aerospace industry. Michael Bruhis and McMaster University undergraduate Caitlyn Dever were primary contributors to DIC testing and data collection. Chris Butcher, McMaster University staff, performed EBSD measurements in the presence of the author.

CHAPTER 1: INTRODUCTION

For over 70 years, the primary method to produce titanium metal is via the Kroll process. This process is energy intensive and requires double or triple vacuum melting operations to remove impurities. Use of titanium alloys is generally limited to the aerospace and medical industries where the benefits outweigh the high cost of manufacture.

The benefits of titanium alloys versus other structural alloys are: low density, excellent high temperature mechanical properties and corrosion resistance. In comparison to steels and aluminum alloys, titanium alloys have a greater strength-to-weight ratio. It is a common misconception that titanium alloys are higher in strength than steels; in fact it is the opposite. Rather, the difference in strength-to-weight ratios comes from the density of titanium alloys being nearly half that of steel. In comparison to aluminum alloys, titanium alloys are denser but can achieve higher strengths. Because of its superior corrosion resistance in air, titanium alloys require no protective paint or coatings, unlike steel and aluminum. Further, titanium alloys excellent high temperature properties makes it suitable for turbine engine components.

Ti-6Al-4V is the most widely used titanium alloy. Its widespread use is attributed to its well-rounded mechanical attributes for strength, fatigue, and fracture toughness. Additionally, it is amongst the easiest titanium alloy to process and is readily weldable. Not long ago, 80 - 90 percent of all titanium alloys found in airframes were manufactured from Ti-6Al-4V [1].

Powder metallurgy for producing near net shape titanium parts is a known alternative manufacturing process which can offset the high cost. This is accomplished by reducing the raw material cost by increasing the 'buy-to-fly' ratio, which is the ratio of the bar or forging weight to finish machined weight, and in turn, reducing the number of machining operations. Recently, the introduction of the 'modified-Kroll' [2] process for the manufacture of hydrogenated titanium powder overcame the necessity for intermediate multiple vacuum melting operations to produce titanium sponge from which traditional powders are manufactured from (i.e. hydride-dehydride [HDH] and gas atomised [GA]). Thus, it is of interest to the aerospace industry to explore the effects of consolidation techniques on fatigue properties, in particular a Ti-6Al-4V component, made from hydrogentated titanium powder.

CHAPTER 2: LITERATURE REVIEW

This chapter will provide a background on commonly known metallurgical principles of titanium alloys including phase diagrams, microstructure, crystallography and methods of manufacture. Building on this background information, research works pertaining to how microstructure can influence mechanical properties, in particular fatigue, of both conventional and powder metallurgy processed titanium alloys will be reviewed. The literature review will be primarily focused on titanium alloy Ti-6Al-4V.

2.1 An overview of titanium metallurgy

2.1.1 Fundamentals of Titanium Alloys

Pure titanium at room temperature has a hexagonal closed pack (hcp) crystal structure referred to as the α phase. When heated above 1620°F (882°C), the crystal structure changes to a body centered cubic (bcc) arrangement, referred to as the β phase. The temperature at which the structure transforms to 100 percent β is known as the β transus (β_T).

Many alloying element additions will stabilize either the α or β phases upon cooling to room temperature from elevated temperatures. α stabilizing elements, such as aluminum, oxygen, nitrogen and carbon, will retain α phase. β stabilizing elements, which are further subdivided as β isomorphous such as vanadium, molybdenum, and β eutectoid, such as chromium and iron, will retain the β phase. α stabilizers tend to increase the β_T, while β stabilizers decreases the β_T as shown in the Figure 2.1 pseudo phase diagrams. Other alloying elements, like

zirconium and tin, are considered neutral additions, as they have little influence on the β_T. However, the term 'neutral' is a misnomer as neutral additions strengthen the α phase.

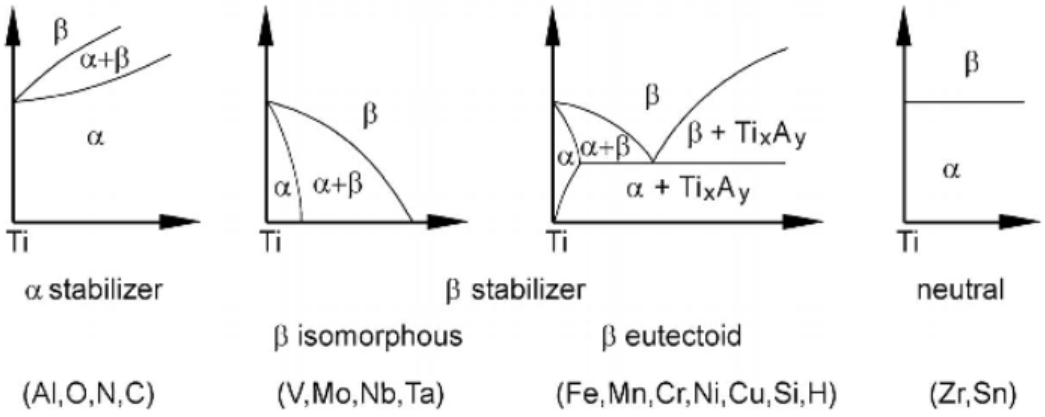

Figure 2.1: Effect of alloying additions on phase diagrams of Ti-X [3]

Titanium alloys are classified as being either α, β, or α + β. By arbitrarily choosing aluminum and molybdenum as a baseline, the α stability of an alloy is based on the aluminum equivalent (Al Eq) and β stability by the molybdenum equivalent (Mo Eq):

$$\text{Al Eq} = 1.0\,\text{Al} + 0.33\,\text{Sn} + 0.17\,\text{Zr} + 10\,[\text{O} + \text{C} + 2\text{N}] \quad (1)\ [4]$$

$$\text{Mo Eq} = 1.0\,\text{Mo} + 0.67\,\text{V} + 0.44\,\text{W} + 0.28\,\text{Nb} + 0.22\,\text{Ta} + 2.9\,\text{Fe} + 1.6\,\text{Cr} - 1.0\,\text{Al} \quad (2)\ [5]$$

The naming convention of titanium alloys is thus an indication of the α or β stability as determined by the amount of alloying additions.

The classification convention is traditionally shown overlaid on a pseudo binary β isomorphous phase diagram as in Figure 2.2. A number of traits are apparent for the different alloy classifications. α alloys are seen as those that

contain only α at room temperature. Thus, α alloys do not respond to heat treatment, rather their strength comes from interstitial strengthening. The α + β alloys extend up to the martensite start (M_s) temperature, and responds to heat treatment of as the β phase is retained at room temperature. Both α and α + β alloys can undergo martensitic transformation under fast rates of cooling. Hexagonal martensite, designated α', is associated with alloys having lower solute content. α' is subdivided into massive (or lath) martensite typical for high purity titanium, and acicular martensite for alloys having a higher solute content. With increasing solute content, the crystal structure of martensite changes to orthorhombic, designated α''. β alloys are subdivided into metastable and stable β. Metastable β alloys are susceptible to heat treatment. The microstructure at room temperature is generally more fine as compared to α + β alloys. At low temperatures, uniformly distributed, extremely fine precipitates can form. For heavily stabilized β alloys, the precipitate is referred to as β', and for decreasing β stabilizers, the ω phase. The ω phase can form for both β and α + β alloys, having a trigonal crystal structure in more heavily β stabilized alloys, and hexagonal structure for alloys with less β stabilizers. β' precipitates have a bcc crystal structure, and are solute lean compared to the surrounding bcc β matrix. The β' and omega phases are not shown in Figure 2.2 for clarity, as they do not relate to the classification convention. The boundaries separating each classification can be further subdivided into near α or near β for a more refined description of the response to heat treatment. [3]

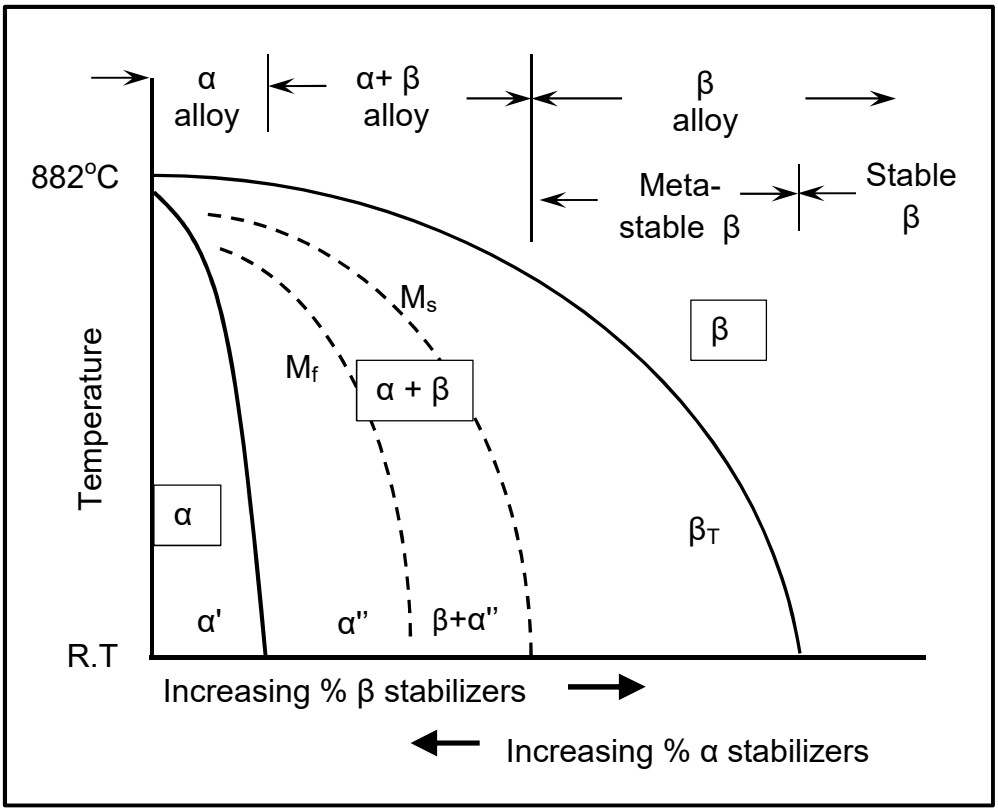

Figure 2.2: Pseudo-binary phase diagram of titanium for an α or β stabilizer element with classification convention overlain. Phase boundaries represented by solid lines, Martensitic start and finish represented by dashed lines [5] [6] [7]

2.1.2 Processing of Titanium and It's Alloy Ti-6Al-4V

With an understanding of the susceptibility to heat treatment, a range of mechanical properties through microstructure control can be achieved by differing thermomechanical treatments. For the traditional method of manufacture, high purity titanium sponge produced by the Kroll process, together with alloying additions, are vacuum arc remelted two to three times to produce an ingot. The coarse β microstructure of the ingot is broken down through a number of forging operations in the β phase field. Following ingot breakdown, recrystallization (homogenization) is usually done by heat treating in the β phase field. For α+β

alloys including Ti-6Al-4V, the final forging operation is done in the α+β region to impart a fine microstructure suitable for final heat treatment. The most common heat treatments for industrial applications include bi-modal annealing, solution heat treatment and aging, or mill annealing. Of these heat treatments, the range of microstructure include bi-modal (primary α and lamellar α+β), Widmanstätten (α lamella in a β matrix), equiaxed α+β, or globular (partially recrystallized α) [9].

The heat treatment temperature and cooling rate have an effect on the microstructure, as shown for Ti-6Al-4V in Figure 2.3. In general, heat treating above the β_T region results in a Widmanstätten structure, whereas heating below the β_T results in a bi-modal or equiaxed structure. Heating well below the β_T results in a globular structure. Increasing the cooling rate generally results in a finer structure. A fast cooling rate results in α', provided the initial temperature is above the Ms temperature.

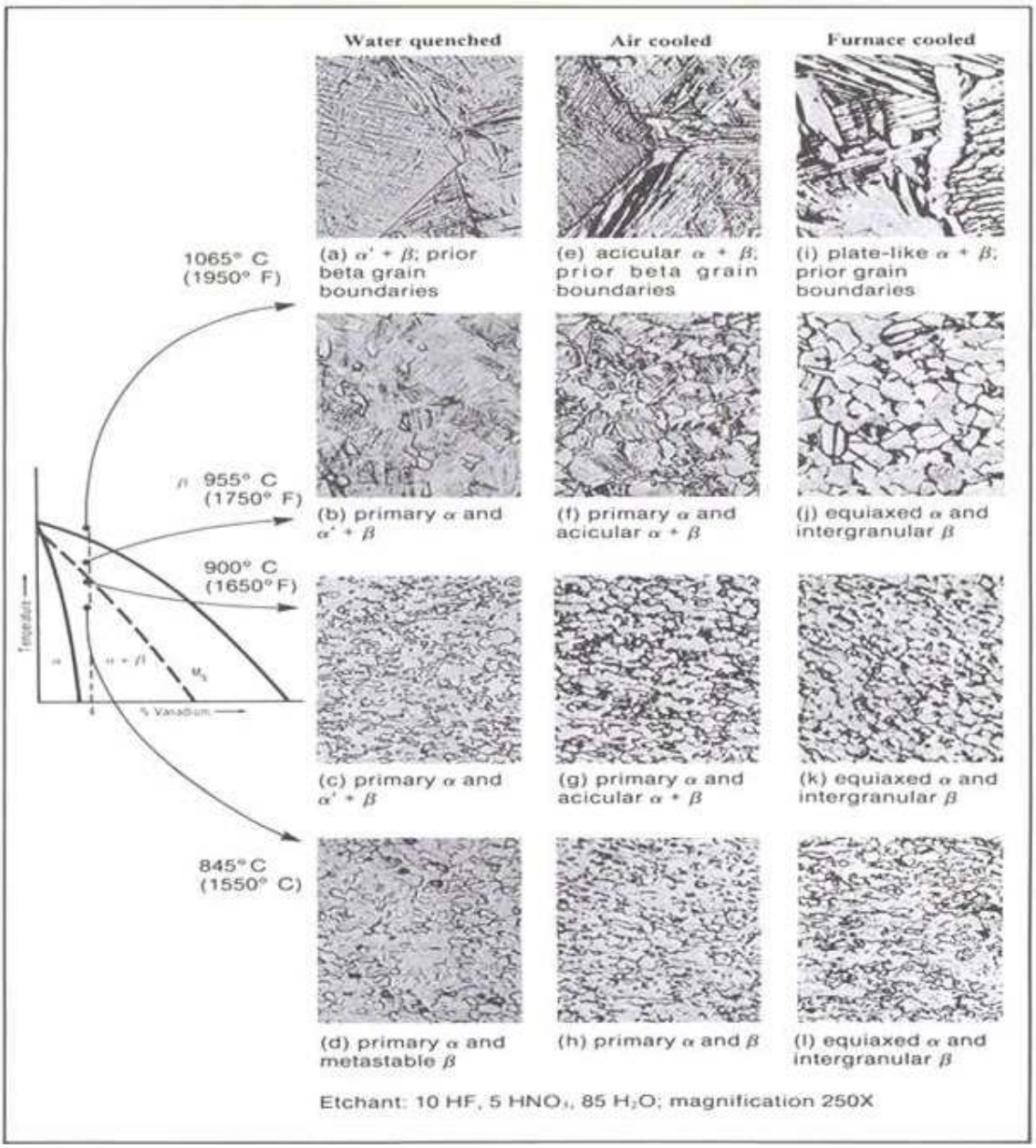

Figure 2.3: Effect on heat treating temperature and cooling rate on microstructural transformations which can occur in Ti-6Al-4V [8].

The thermomechanical processing route to achieve a bi-modal microstructure is shown in Figure 2.4. As defined by Lutjering [3] [11], the cooling rate following homogenization after ingot breakdown is a critical process parameters as it dictates the width of α lamella, which in turn determines the primary α size following annealing. A fast cooling rate will favour a narrower α lamella and prior grain boundary α width, resulting in a finer primary α after annealing. The homogenization time and cooling rate, however, has no effect on the prior β grain size which is always considerably large. Following homogenization, deformation in the α+β region is carried out to deform the lamellar structure. Crystallographic textures can develop based on the type of deformation (to be discussed in the following section). The stored work dictates the amount of recrystallization during heat treatment. During annealing in the α+β region, primary α forms at the triple points of prior β grains whereby the volume fraction is determined by the annealing temperature in relation to the β_T. The heat treatment cooling rate affects the transformed β matrix colony size and α lamellar colony size. The combination of these two parameters, annealing temperature affecting primary α V_f and cooling rate affecting primary α size, determines the maximum size (distance between) of primary α grains. The aging treatment acts as a stress relief if the temperature is sufficiently high. At lower temperature, age hardening occurs by precipitation of Ti_3Al particles.

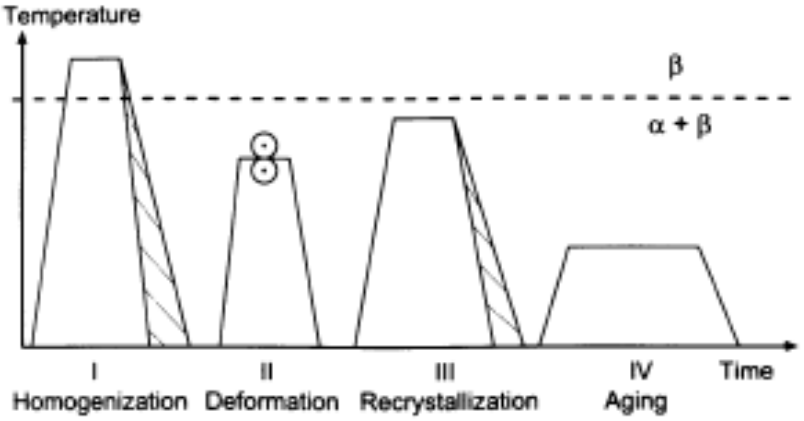

Figure 2.4: Typical processing route of α+β titanium alloys [3] [11].

2.1.3 Crystallographic Texture

It was previously mentioned the type of deformation used when processing α+β alloys like Ti-6Al-4V can introduce differing crystal textures. This crystal texture can be controlled separately from microstructure and gives rise to anisotropic properties [12]. It is therefore important to discuss how texture affects mechanical properties for the purpose of this study. Mechanical properties are influenced based on the orientation of the HCP α phase to the direction of applied load, which leads to deformation by crystallographic slip. For the HCP crystal structure, the principal planes for slip are the basal (0001), prismatic $\{10\bar{1}0\}$ and pyramidal $\{10\bar{1}1\}$ planes as depicted in Figure 2.5. However, the basal and prismatic planes are the most commonly observed slip planes for bi-modal structured titanium alloys [13] [14].

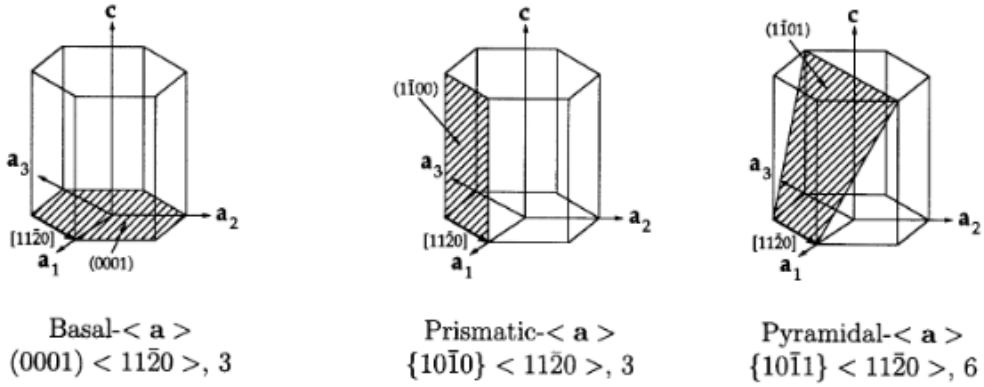

Figure 2.5: Dominant planes for slip of the HCP unit cell [13]

For bi-modal structured titanium, banding of primary α grains having similar crystal orientation are referred to as macrozones [14] [15] [16]. Macrozones, which are formed from prior β grains, can be detrimental to fatigue properties by acting as a single unit having a lower resistance to slip.

2.2 Fatigue Behaviour of Wrought Ti-6Al-4V

2.2.1 Fatigue Testing and Characterization

As the primary focus of this research is fatigue, it is necessary to describe the way in which fatigue damage is determined. Cumulative damage theory is the traditional method of fatigue life prediction. It involves physical testing of samples to correlate the number of cycles to failure, *N*, to the applied stress or strain range, *S*, resulting in the so-called *S/N* curve. Fatigue cracks in metals can be said to occur in two stages. Stage I is the crack initiation phase caused by shear cracking along crystallographic slip planes. Stage II is the characterized by fatigue striations once a crack nucleates. The crack propagates normal to the applied loading direction until ultimate failure ensues from an inability to withstand

load due to the reduced cross section area. A more detailed description is given by Cui [17]. Descriptive parameters that accompany *S/N* curves are the stress ratio, R, and stress intensity, k_t. The stress ratio is a ratio of the maximum applied stress (or strain) to the minimum stress. Stress intensity depends on the geometry of a notch in the sample gage length (k_t = 1.0 implies a smooth sample). For use in design, it is useful to describe an endurance limit, i.e. the stress (or strain) below which a crack will not propagate. When a plateau does not occur in the S/N curve, the endurance limit is typically taken at $N = 10^7$ cycles. S/N data is usually accompanied by large scatter as subtle variations in microstructure, crystallographic texture, surface texture and preparation, or testing environment can affect fatigue life.

2.2.2 Effect of microstructure

Thermomechanical working of Ti-6Al-4V can be tailored to achieve a range of microstructures ranging from bi-modal to lamella, equiaxed and globular, based on mechanical properties desired. In general, thermomechanical work that decreases the primary α volume fraction [3], the size of primary α grains [20], or both [18] [19] results in an increase in fatigue strength. Note the previous cited references are summaries on works ranging from 1971 to 2012 on how microstructure affects fatigue life for α+β titanium alloys. Fast cooling rates (water quenching) can further increase fatigue performance through the creation of martensitic α [18] [21]. However, in commercial practice the deliberate creation of martensite for strengthening purposes is avoided due to embrittling concerns

from further processing [10]. S/N curves of a variety of heat treatments and microstructures that show how microstructure affects HCF is shown in Figure 2.6.

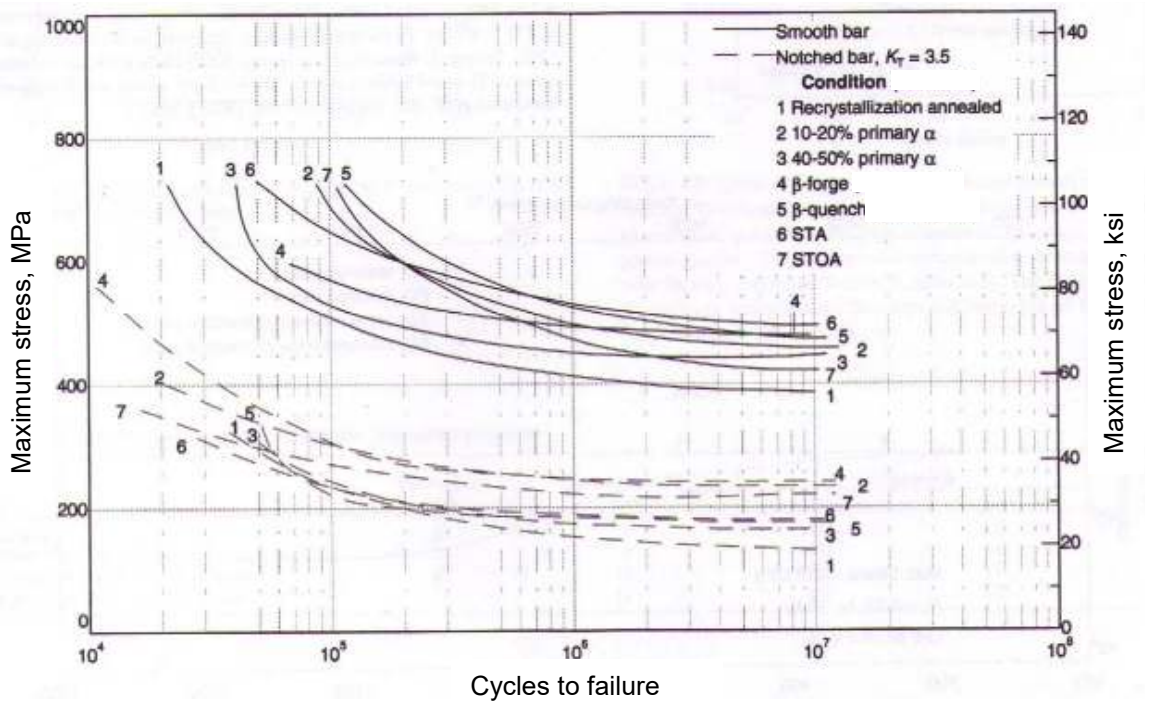

Figure 2.6: Effect on heat treatment on HCF of IM Ti-6Al-4V [18]

As summarized by Wu [19], there is conflicting evidence as to whether a lamellar or bi-modal structure has a higher HCF resistance. One possible explanation is the difference in crack growth, which is faster for bi-modal and slower for lamella structures [22]. Thus, resistance to crack *initiation* is more critical to bi-modal structure than is resistance to crack *propagation*, which is critical for lamellar. In one instance, the bi-modal structure was described as having the best balance between tensile strength and fatigue properties [23]. However, in another instance specific to bi-modal titanium, HCF resistance is said to not adequately be described by one individual microstructural feature [24].

2.2.3 Effect of texture

In addition to microstructure, texture can affect Ti-6Al-4V fatigue performance by crystallographic slip. Stroh's theory [25] suggests fatigue cracks propagate by dislocation pile-up generated by stresses offloaded from the weak (basal oriented) grain onto the stronger (prismatic) grain, which eventually shears the stronger grain. This phenomenon is referred to as load shedding.

Lutjering and Willams [3] describe how the HCF strength of bi-modal and lamella microstructures is primarily driven by slip length, which in turn is determined by the size of primary α grain size. A secondary contributor is the alloy element partitioning effect, which increases with increasing primary α grain size. Increases in the alloy element partitioning soften the transformed β colony region, which lowers the fatigue strength.

In considering the relationship of HCF on primary α grain size, reducing the α grain size (volume fraction) of bi-modal microstructure, as a method to reduce slip length and alloy element partitioning effect, would improve fatigue life. Conversely, with increasing primary α grain size, the slip length increases, allowing fatigue damage to occur with relative ease [26] [27]. Further increase in primary α grain size leads to interconnected primary α grains which act as one unit for slip to occur [22]. Bands of interconnected primary α grains oriented favourably for slip, deemed macrozones, can further accelerate fatigue damage [15].

For wrought titanium, fatigue initiation sites are associated with quasi-cleavage facets commonly having a basal plane orientation [28]. A sketch of facet formation is shown in Figure 2.7. Initiation sites are generally at the surface in the LCF regime, and subsurface in the HCF regime.

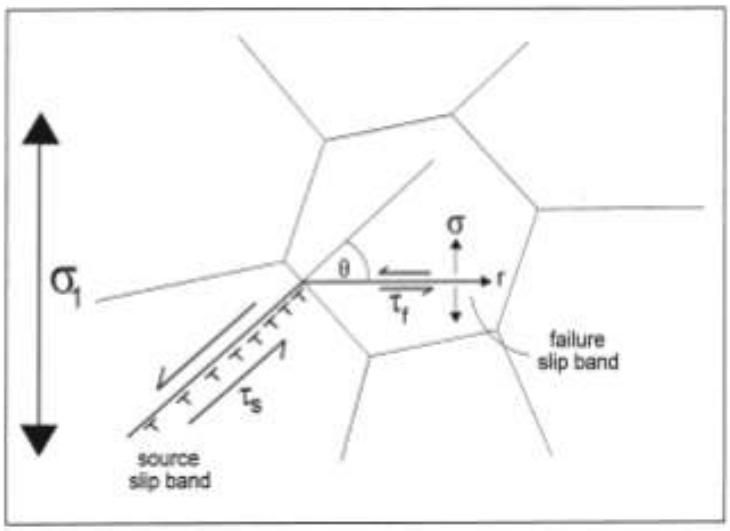

Figure 2.7: Slip band modal depicting facet formation and load shedding in titanium alloys [28]

Bache [28] demonstrated the transverse direction of unidirectional rolled bi-modal Ti-6Al-4V (Figure 2.8) had a higher fatigue life than the longitudinal direction under load control, while the relationship was reversed for strain control fatigue. This was a result of the greater number of slip (prismatic) systems in the longitudinal direction which allowed for stress relaxation and thus longer life at the same strain level.

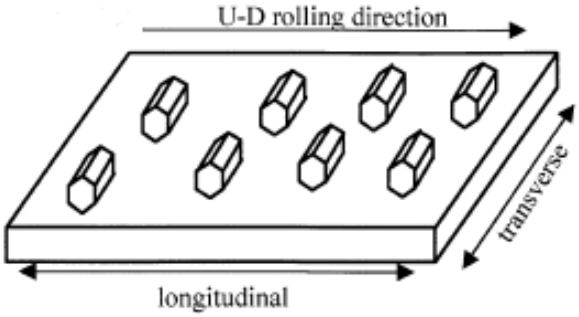

Figure 2.8: Preferred HCP crystal orientation from uni-directional rolling of a Ti-6Al-4V alloy. Longitudinal direction has the highest strain controlled fatigue life, and transverse direction the highest load control fatigue life. [29]

Bantounas [30] observed macrozones to cause large areas of faceted fracture when oriented with the macrozone c-axis parallel to the loading direction, while macrozones with their c-axis perpendicular to the loading direction resisted slip. Biavent [31] observed local strain variations of +/-15% caused by a difference in macrozone orientation for a bi-modal Ti-6AL-4V notched fatigue specimen, which resulted in a high scatter band.

2.2.4 Effect of interstitials

Oxygen, carbon and nitrogen are known to affect the mechanical properties of titanium and titanium alloys by interstitial solute strengthening. These interstitials have a combined, additive effect on alloy strength as described by the oxygen equivalency (OE) defined by Ogden and Jaffee [32]:

$$OE = O + 2N + 2/3C \quad (1)$$

Generally for titanium alloys, with increasing strength, the fatigue strength can also be expected to increase. The *OE* may then also be applicable to fatigue strength in some fashion.

Subtle variations to Ogden and Jaffee's OE equation have been suggested by Harwig et. al. [33] when studying effects of hardness, ductility and strength on CP titanium welds. CP titanium owes its strength primarily to interstitial solute strengthening as it cannot be heat treated and is thus well suited for investigation of an OE. Despite a more accurate OE equation that included an iron term (an impurity in CP titanium), the Ogden and Jaffee OE equation was found to apply reasonably well. This demonstrates the robustness and suitability of the *OE* equation to apply to other titanium alloys.

Liu and Welsh [34] studied the effects of oxygen and heat treatment for α + β and β alloys. Despite different alloying additions and heat treatments, the hardness of the α+β and β alloy increased by the same degree to the square root of oxygen concentration. They commented alloy hardness was greatly affected by minute differences in oxygen concentration compared to substitutional alloy additions, despite being in substantially greater quantities. While there is no relationship between hardness and strength for titanium alloys, with increasing hardness, the tensile strength would also be expected to increase. This further highlights how the OE may dictate fatigue strength. Further, as the alloys studied were coarse grained, the hardness could be further influenced by grain refinement described by the Hall-Petch relationship. Thus, a combination of microstructure and *OE* may dictate fatigue strength of titanium alloys.

2.3 Fatigue Behaviour of Powder Ti-6Al-4V

2.3.1 Sintered fatigue performance

In contrast to fatigue controlling features of IM, the dominating fatigue characteristic of PM titanium is porosity size. While tensile properties are relatively unaffected by porosity with a density near 100 percent theoretical, fatigue resistance can be reduced markedly (10 – 30 percent) with a density of only 98 – 99 percent of theoretical [35]. This greater sensitivity of porosity on fatigue demonstrates that tensile strength may not be a reliable predictor for fatigue strength, as was proven for IM Ti-6AL-4V [20].

In comparing fatigue resistance of sintered PM compacts to ingot casting, Ivasishin [36] demonstrated the bending fatigue limit of lamella structured PM Ti-6Al-4V was equivalent to ingot castings. However, in comparing sample geometries having smooth versus sharp corners, the PM compacts had a profound reduction in fatigue life for the sharp corner geometry, while ingot castings were unaffected. This lower fatigue life of PM material was attributed to porosity open to the surface and compounded by the artificial stress riser of the sharp edge geometry. This observation shows the need for fatigue specimens made from PM Ti-6Al-4V to have rounded edges to ensure an adequate comparison to IM.

The correlation between pore size and fatigue resistance of lamella PM Ti-6Al-4V PM after sintering and annealing was also studied by Cao [38]. For similar stress levels, it was demonstrated that cracks initiating from surface porosity led

to a lower fatigue life than cracks that initiated from interior porosity. Further, crack initiations from smaller sinter-pores had an improved fatigue life than larger cave-pores for both surface and interior crack initiations. The relationship between fatigue life and pore size correlated well to the stress intensity factor of the equivalent pore size diameter, considering separate groups of surface versus interior initiation.

A relationship between pore shape factor and fatigue life of sintered PM Ti-6Al-4V was proposed by Yan [39]. A correlation was demonstrated between the shape factor and stress intensity of the pore that cause fatigue crack initiation. Fatigue cracks initiating from pores with increasing shape factor[1] had longer fatigue lives. A relationship between increasing lamella colony size and decreasing fatigue endurance limit was also shown. It was also suggested the differing oxygen percentages of the PM compacts investigated may have influenced the endurance limit. This highlights the importance when studying fatigue of PM material to consider all factors known to affect fatigue, and not those which are the most obvious, such as porosity.

2.3.2 Consolidated powder fatigue performance

In an attempt to improve the fatigue properties of sintered PM titanium alloys, a hot working operation such as hot isostatic pressing (HIP), hot forging or extrusion is employed after sintering to increase densification.

[1] (Circle) Shape Factor, $F = (4\pi A)/P^2$, where A is pore area and P is the perimeter

During the 1980's, mechanical properties, including fatigue, for HIPed BEPM Ti-6Al-4V made from sponge fines was investigated. Mechanical properties suffered due to the chlorine content in sponge fines. A density of 99.8% was found to meet the lower HCF bound of annealed IM, but ultimately only 100% dense material could achieve fatigue properties equivalent to IM [40]. Some improvement in fatigue strength was made using low chloride powders [41]. More recently, Zhang [42] and Guo [43] have achieved nearly identical fatigue properties of IM from HIPed PM Ti-6Al-4V. However, powders used in these studies were pre-alloyed and manufactured by gas atomized (GA), plasma rotating electrode process (PREP) or hydride-dehydride (HDH), rather than BE hydrogenated titanium powder used in the present study. Zhang also attributes the high fatigue strength to carbon diffusion from the HIP steel canister and would thus not be considered a comparable alloy to IM. In general from the previous literature on HIPed titanium alloys made from powder, the dynamic mechanical properties are more sensitive to porosity than tensile properties, believed to be attributed to the high stress concentration caused by porosity.

Forging after pressing and sintering of Ti-6Al-4V made from hydrogenated titanium powder has been shown to produce equivalent fatigue properties as IM. Researchers at Pacific Northwest National Laboratory (PNNL) [44] demonstrated bi-modal microstructured PM Ti-6Al-4V having near full density exceeded the endurance limit of IM. However, no characterization of grain size or chemistry was mentioned. It is estimated by the author of this thesis that the fine structure

achieved from thermomechanical processing of the PM material likely offset the detrimental effects (high stress concentration) of residual porosity. This assumption is based on the size of porosity being smaller than the primary α grain size shown in Figure 2.9. Thus, the fatigue life is believed to be limited to the same microstructurally weak features as with IM.

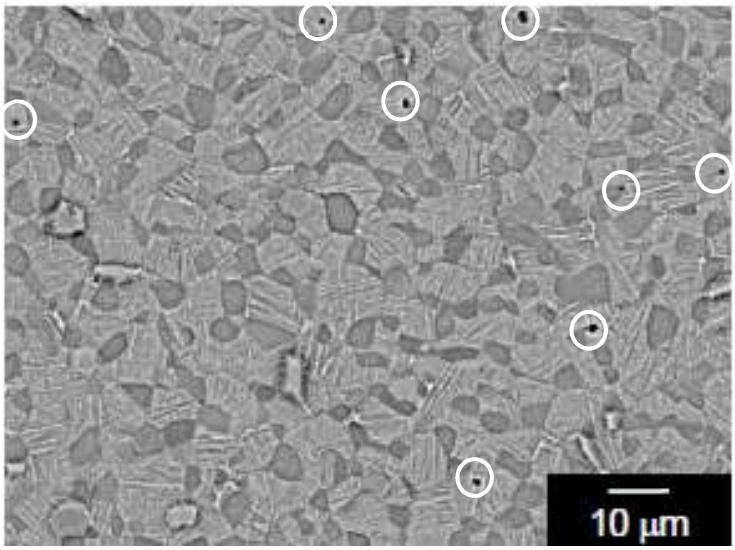

Figure 2.9: Bi-modal microstructure of sintered and hot rolled Ti-6Al-4V PM with residual porosity (encircled) produced by PNNL having an endurance limit exceeding wrought IM (SEM image) [44]

A similar outcome was achieved by El-Soudani et al. [45] who performed canless extrusion of sintered PM Ti-6Al-4V using hydrogenated titanium powder. The resulting material was ‘near fully dense’ having a lamella structure and within the chemical composition requirements, including interstitials, for aerospace grade IM. Mechanical and fatigue strength exceeded the extruded IM baseline. However, the characterization of microstructural features necessary to

understand the failure mechanism, including density, pore size and grain size, were not mentioned.

Additional work by El-Soudani et al. on sintered and hot rolled Ti-6Al-4V PM plate and sheet [46] [47] was also successful at meeting and exceeding the endurance limit of IM. The author of this thesis plotted these results of El-Soudani et al, as shown in Figure 2.10, and determined that a minimum thickness reduction ratio[2] of 4:1 was essential to achieve the endurance limit. However, further reduction lowered the endurance limit by coarsening of primary α, seen in Figure 2.11. Additionally, reduction beyond the 4:1 minimum did not guarantee complete densification. As seen in Figure 2.12, porosity having a length up to approximately 15 μm did not affect the endurance limit, provided there was sufficient grain refinement from forging. Further, porosity having a length up to approximately 40 μm still remained after a reduction ratio of 17:1, which coupled with a coarse bi-modal structure, had poor endurance limit.

These results on fatigue properties of forged Ti-6Al-4V made from PM all demonstrate the need to consider microstructural features in addition to porosity size. Additionally, the mechanism responsible for fatigue strength of forged titanium alloys made from PM has not been addressed; rather the prior research focus has been strictly mechanical property characterization.

[2] The forging reduction ratio was reported in the study as the initial and final wall thickness. This was calculated into a percent reduction: $R\% = (L_i - L_f)/L_i$. This is in contract to the traditional area reduction formula, $R\% = (A_i - A_f)/A_i$

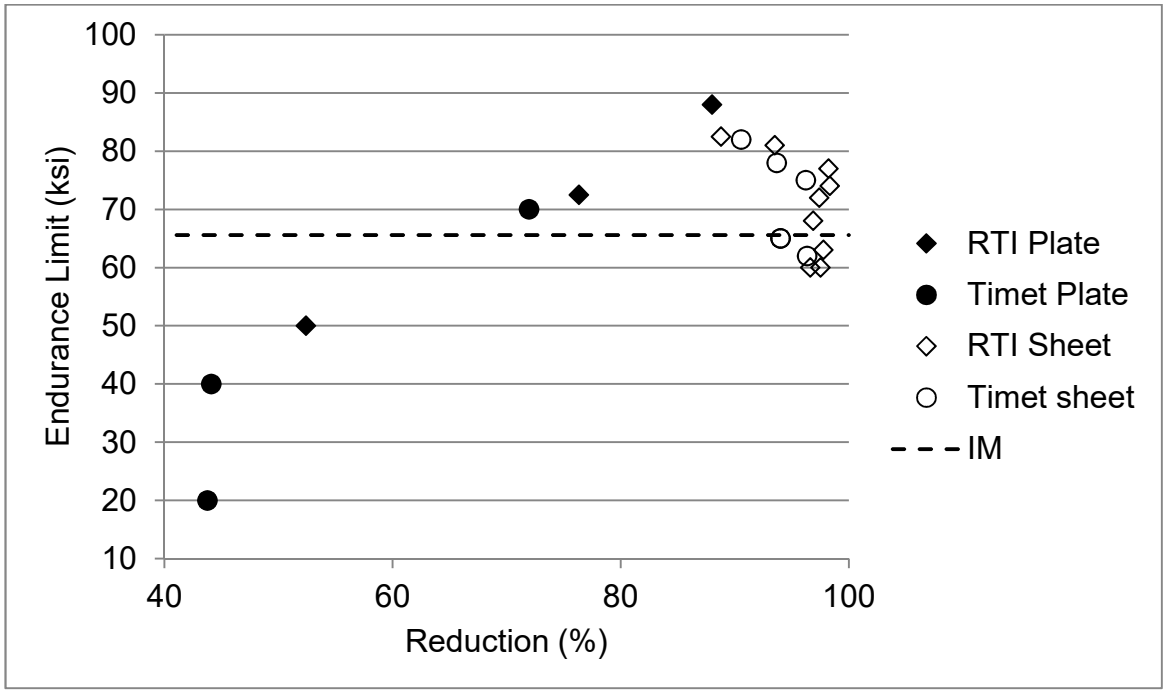

Figure 2.10: Axial fatigue endurance limit versus percent reduction, $R\%=(L_i-L_f)/L_i$, from hot rolling pressed and sintered BE Ti-6Al-4V PM [46] [47]

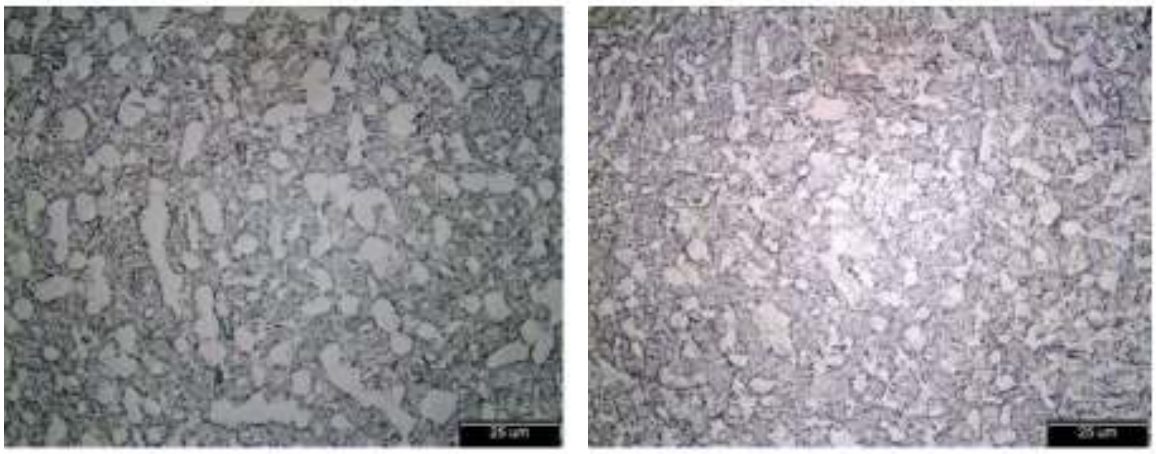

Figure 2.11: Bi-modal structure of sintered and hot rolled Ti-6Al-4V PM sheet with full density having endurance limit and total rolling reduction of 60 ksi at 30:1 (Left) and 82.5 ksi at 9:1 (Right) [47]

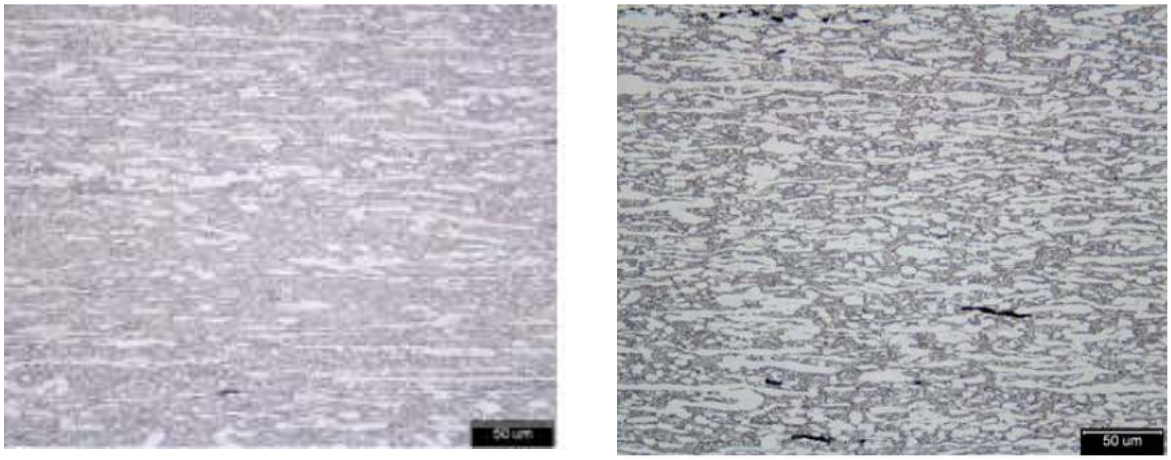

Figure 2.12: Bi-modal structure of sintered and hot rolled Ti-6Al-4V PM sheet with residual porosity having a fatigue endurance limit and total rolling reduction of 82 ksi at 11:1 (left), and 65 ksi at 17:1 (right) [46]

2.4 Research Objective

The increase in use of titanium alloys and importance of Ti-6Al-4V to the aerospace industry was introduced. In order to meet this increase in demand, a novel manufacturing method incorporating BEPM has been studied recently for Ti-6Al-4V. Prior works have demonstrated forged Ti-6Al-4V made from PM is capable of meeting properties of IM through a reduction in porosity and refinement in the microstructure grain size. However, not much effort has been paid to correlate the physical relationship of microstructure to fatigue strength of PM Ti-6Al-4V. This is important for the aerospace industry to understand as it was shown forged BEPM Ti-6Al-4V can meet or exceed the fatigue endurance of IM Ti-6Al-4V, despite there being residual pores in the material.

It was previously stated that no single microstructural parameter can adequately describe fatigue performance. This was demonstrated for the

endurance limit of IM Ti-6Al-4V which was strongly influenced by primary α volume fraction, size of primary α, and crystal texture. Solute strengthening, which can be correlated to tensile strength, may also play a role. In contrast to sintered BEPM Ti-6Al-4V, the endurance limit was found to be strongly influenced by porosity size, shape factor and/or density. It is hypothesized a combination of the controlling units known for IM and that for sintered product are required to accurately describe the fatigue endurance limit of forged BEPM Ti-6Al-4V.

The present research will investigate the fatigue performance of BEPM Ti-6Al-4V that has been ring forged and hot rolled. By using two product forms, it is believed the results will lead to a broader applicability. The research will be broken down into three components. The first component will be mechanical testing. Secondly, a detailed metallurgical characterization will be conducted to gather data on known controlling factors for fatigue including microstructural features, texture and chemistry. A subset of the second component will be an investigation into whether residual porosity affects global and/or local strain distribution, and subsequently fatigue crack initiation and growth. Finally, the data collected from the second component will be used to perform a statistical analysis to identify the controlling microstructural parameters on the fatigue life of BEPM Ti-6Al-4V. A ranking of the most influential parameters on fatigue will also be given.

CHAPTER 3: MATERIALS & METHODS

This chapter will begin with an outline on the method of manufacture for the two different products forms of forged Ti-6Al-4V made from BEPM. Process diagrams are also given. The various methods of testing will then be discussed. This will include fatigue testing and digital image correlation (DIC). Sample preparation for the various test methods and analysis techniques (optical microscope, SEM, EBSD and chemical) are discussed, along with accompanying extraction and sample geometry diagrams.

3.1 Manufacture of powder forgings

3.1.1 Powder Billet Manufacture

The powder used for this study was hydrogenated titanium produced by ADMA Products Inc. Hydrogenated titanium sponge was ground and sieved through a 100 mesh leading to a particle size of <150 μm. The resulting powder was irregular, angular shaped as shown in Figure 3.1. The chemical composition was that shown in Table 3.1.

Three solid round billets of blended elemental Ti-6Al-4V were manufactured by ADMA Products Inc. The billets were made from three different powder lots (separate blending and sintering operations) identified as ‘A’, ‘B’ and ‘C’. Aluminum-Vanadium master alloy having a composition of 60% Al – 40% V was sourced by ADMA and blended with hydrogenated titanium powder in proportions corresponding to the composition of industry grade Ti-6Al-4V. The powder mixture was cold isostatic pressed and vacuum sintered. Following sintering, the

weight percent of oxygen increased while hydrogen decreased as shown in Table 2. Processing parameters related to temperatures, compaction pressure, processing time and weights are proprietary to ADMA Products Inc.

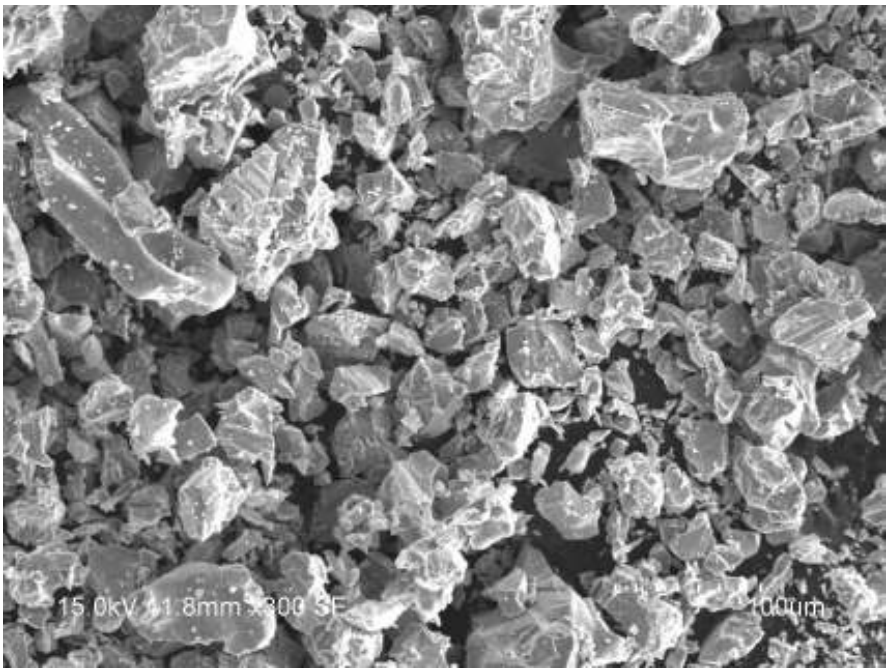

Figure 3.1: Angular morphology of crushed hydrogenated powder

Table 3.1: Chemical Composition of Hydrogenated Titanium Powder

Element	Cl	H	O	N	C	Fe	Si	Ni	Ti
wt %	0.060	3.40	0.110	0.030	0.010	0.070	0.010	0.020	Bal

Table 3.2: Chemical Composition of BEPM Billets After Sintering

Element	Al	V	H	O	N	C	Fe	Si	OOE	TOE	Ti
Lot A	5.83	3.96	.0052	.211	.015	.008	.15	.14	<.10	<.40	Bal
Lot B	6.06	3.99	.0097	.217	.017	.009	.16	.13	<.10	<.40	Bal

3.1.2 Manufacture of Seamless Rings

Two of the three pressed and sintered billets were saddle forged by Schlosser Forge Inc. While ring rolling was specified in order to achieve a more uniform microstructure, Schlosser Forge opted instead to perform saddle forging. A process overview for manufacturing the forged rings is shown in Figure 3.2. Billets were β drawdown and upset forged, and sectioned into mults. The mults were α+β drawdown and upset forged, pierced, and α+β ring forged. Forged preforms were then α+β annealed in air. Each forged ring is referred to by a dash number, (-1, -2) following the billet letter. Processing parameters related to temperatures, reduction ratios and processing times are proprietary to Schlosser Forge Inc. Due to excessive time at temperature between forging reheats, the total hydrogen content measured after heat treating was beyond the industry standard maximum of 150 ppm [48] due to hydrogen pickup from the air atmosphere. All preforms were subsequently vacuum degassed at the same time and temperature as done for annealing. The resulting chemistry is shown in Table 3.

Table 3.3: Chemical Composition of PM Preforms After All Processing (wt %)

Element	Al	V	H	O	N	C	Fe	Si	OOE	TOE	Ti
Lot A	6.2	4.1	.0125	.216	.025	.007	.16	.02	<.10	<.40	Bal
Lot B	5.98	3.98	.0120	.194	.045	.007	.15	.02	<.10	<.40	Bal

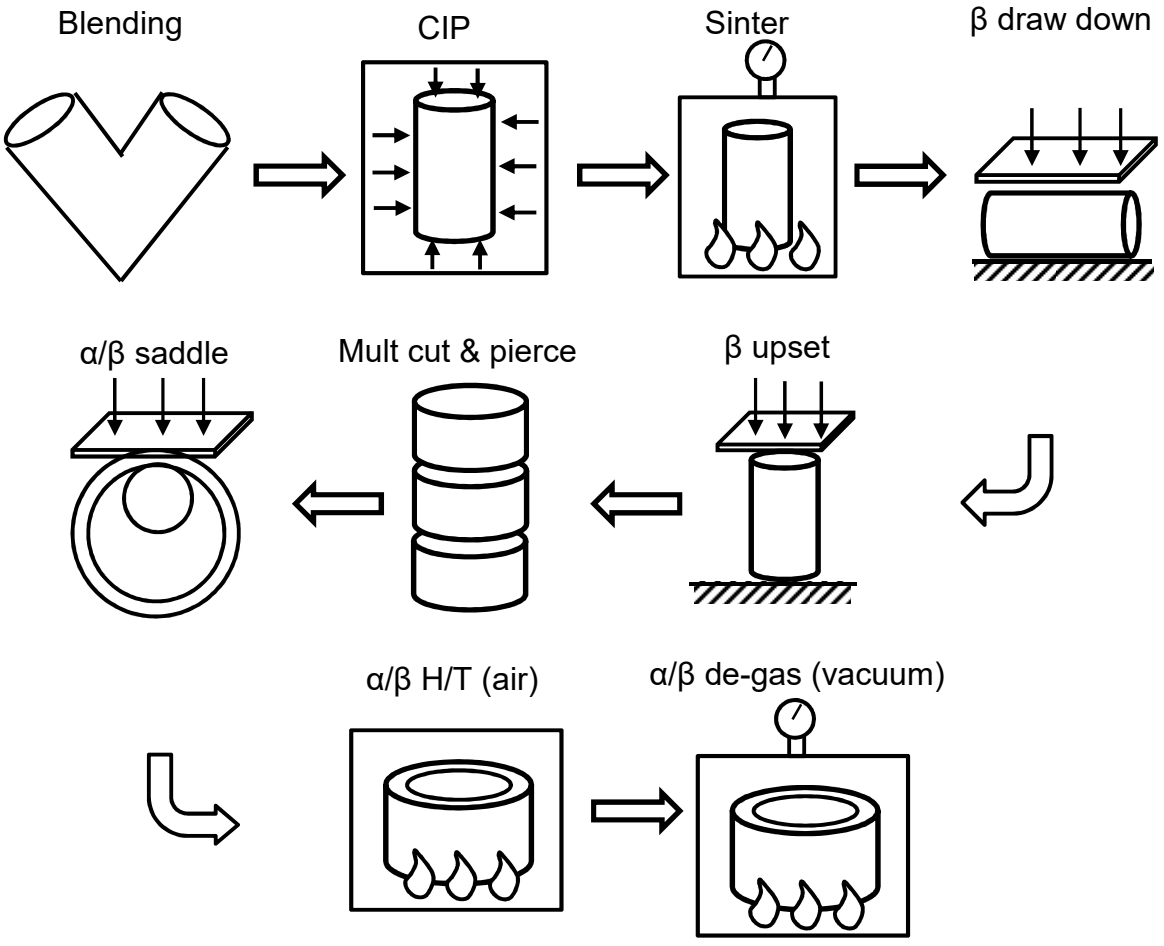

Figure 3.2: Powder billets for ring forging were blended, CIP and sintered. Billets were open die β upset and draw down forged over multiple passes. Billets were cut into mults and forged into a single ring. Forged rings were annealed then de-gassed to remove excess hydrogen.

3.1.3 Manufacture of Hot Rolled Plate

The final pressed and sintered billet was hot rolled by an established titanium forging company. A process overview for manufacturing the forged rings is shown in Figure 3.3. The billet was sectioned into mults prior to rolling, of which only one mult was used for this study. The mult was rolled in the α+β region to a predetermined plate thickness over the course of multiple passes. The resulting plate was α+β annealed in air at the same processing time and temperature as the forged rings. Processing parameters related to temperatures, reduction ratios and processing times are proprietary to ADMA Products Inc.

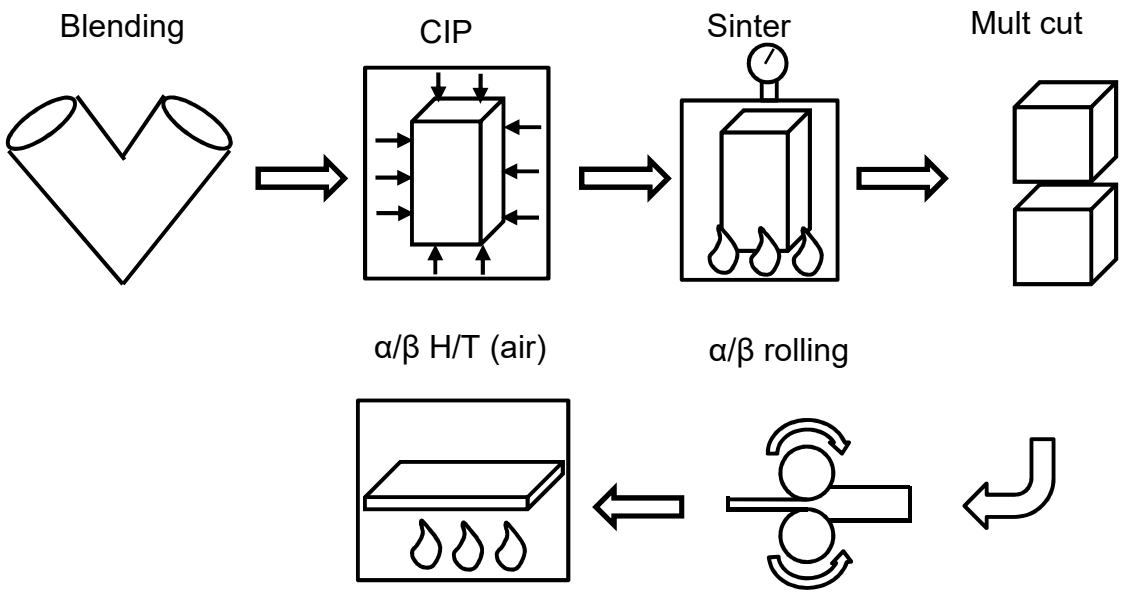

Figure 3.3: Powder billets for hot rolling were blended, CIP and sintered. Billets were cut into mults. A single mult was hot rolled over multiple passes and annealed.

3.2 Fatigue Testing

3.2.1 Fatigue Endurance Testing

Fatigue testing was conducted to determine the endurance limit of the forged material. Testing was performed at an accredited aerospace test laboratory using a hydraulic, computer controlled MTS 810 frame with a FlexTest SE 2-channel controller. Specimens were cycled axially under strain-control according to ASTM E 606 [49] using a triangular load profile at a frequency of 0.5 Hz. Smooth (K_t = 0) round bar specimens were used. The actual gage diameter was measured prior to each test.

Tensile testing was performed prior to fatigue testing for comparison to industry minimum tensile properties of wrought Ti-6Al-4V. Testing was performed according to ASTM E 8 [50] using a hydraulic, computer controlled 50kip MTS frame. The actual gage diameter was measured prior to each test.

3.2.2 Digital Image Correlation

The change in global and local strain distribution during cyclic deformation and crack tip growth was determined by Digital Image Correlation (DIC). A hydraulic, computer controlled MTS 810 frame with an Instron 8800 control system was used for cyclic testing, coupled with an ARAMIS system by GOM. Specimens were cycled axially under load control in a triangular profile at a frequency of 0.5 Hz. Although strain control would have been preferred for direct correlation to fatigue endurance testing, there was a lack of confidence in the strain readout. Attempts were made to stabilize the strain readings with differing

O-rings, knife edges, and extensometers to no avail. Due to the strain level being within the elastic region of the material, the specimen response under load control can be considered similar to strain control.

Global strain was measured by applying a stochastic pattern to the gage length of a flat specimen, as shown in Figure 3.4, by alternating passes of white and black spray paint. A single CCD camera was positioned directly in front of the specimen and captured images every 25 seconds, or 1 image per 50 cycles.

Figure 3.4: Drawing of stochastic mask on flat specimen used for global strain DIC

Local strain was measured by DIC. Microhardness indentations were made along the gage length centreline of a polished and etched flat specimen as reference points shown in Figure 3.5. Micrographs centred on the indentations were made prior to testing using a compound microscope equipped with a digital camera. The specimen was physically removed following 8,000, 16,000, 24,000,

32,000 and 51,962 (failure) cycles to have micrographs taken from the same reference locations. The etched microstructure acted as the stochastic pattern for computation of local strains.

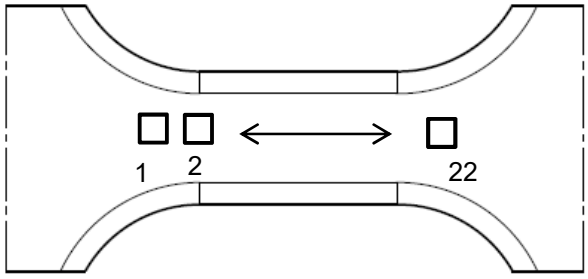

Figure 3.5: Microhardness indentation locations representing individual view fields for local strain DIC of straight gage flat specimens

The basic principle of DIC consists of tracking a reference location on the surface of a material over time that is being deformed. The change in displacement of the reference location compared to the initial position is used to calculate strain. By using a grid of reference locations, one can calculate the strain field (strain map). This is accomplished by taking a series of digital images whereby the grey level of an individual pixel is used as the reference location. In practice, an individual pixel is not tracked as many pixels can have the same grey level and would lead to measurement error. Rather, this is accomplished by tracking neighbouring pixels, referred to as a facet. For 2-D measurements using a single camera, the distance from the sample surface to the digital camera must be fixed, as changes in the focal distance can cause measurement error. The grey level pattern must also be unique (non-repeating, high contrast and

isotropic) such that computer software can recognize each facet. A random, or stochastic pattern is applied for this purpose. The lighting conditions during image capturing must also be sufficient to ensure high contrast images.

The way a computer algorithm determines strain is by calculating changes in the facet center position, which is determined by the position of the facet corners. An example is shown in Figure 3.6 where for a facet size of 6 x 6 pixels, it can be seen to translate right by two pixels and upwards by two pixels. In practice, the facet can not only translate in two dimensions, but also rotate and become deformed (non-square). The facet size is determined by the user based on the resolution desired and generally overlaps with one another. A smaller facet size has higher resolution, but is ultimately limited to the resolution of the stochastic pattern. An example of a deformed facet grid is shown in Figure 3.7. The displacement of each facet center is calculated into a strain map which is presented to the user as a colour contour plot. For the interested reader, a more thorough and detailed explanation of the computations for DIC is given by Sutton, Ortue and Schreier [52].

For this study, a facet size of 49 x 49 pixels was used, which corresponds to a resolution of 20μm. Due to complications with specimen surface preservation between interruptions and non-uniformity in grey level, each facet selection had to be done manually. The coarse facet size used was not ideal, but was determined to be the best compromise between resolution and noise filtering.

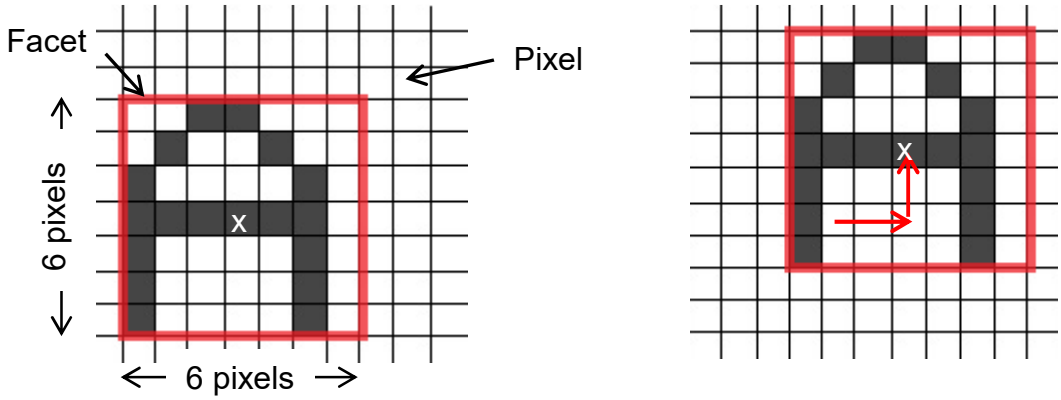

Figure 3.6: Theoretical facet grid for DIC, before and under loading, showing change in displacement of centre point, 'x'

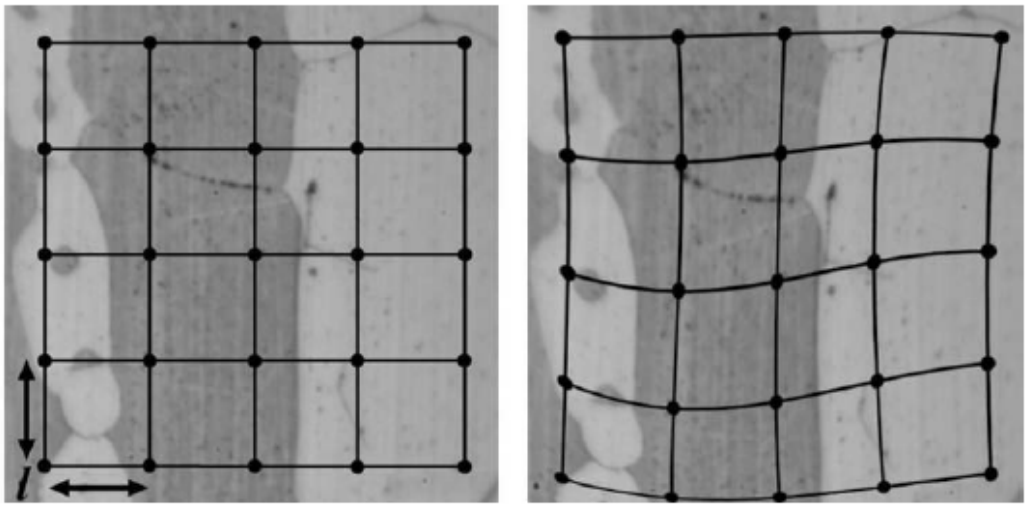

Figure 3.7: Example of the change in displacement between an unloaded (left) and loaded (right) sample for a 4x4 grid of facets with size '*l*x*l*'. The etched microstructure acts as the stochastic pattern [51]

3.3 Sample Preparation and Testing

3.3.1 Tensile

Tensile specimens were extracted near the mid-section thickness. Specimens were round gage conforming to the dimensions in Figure 3.8. Testing was conducted in accordance with ASTM E 8 [50].

3.3.2 Fatigue

Specimens for determination of the endurance limit were smooth (k_t = 0) round gage, conforming to the dimensions in Figure 3.9 and tested according to ASTM E 606 [49]. The gage length was low stress ground and polished in the axial direction. The surface was finished to 8 (μin) Ra to prevent micro k_t features (machining lines) from influencing crack initiation.

3.3.3 DIC

Specimens for DIC were straight gage, flat plate-type specimens conforming to the dimensions in Figure 3.10. The corners were rounded to one-third the specimen width to limit k_t effects of having sharp notch. One face was mechanically ground with silicon carbide paper, polished with 9μm diamond paste and OPS + 10% H_2O_2, and etched with Kroll's Reagent to reveal the microstructure for local strain mapping. The opposing face was ground, the edges hand sanded and polished to reduce stresses from machining marks, and a stochastic pattern applied for global strain measurement.

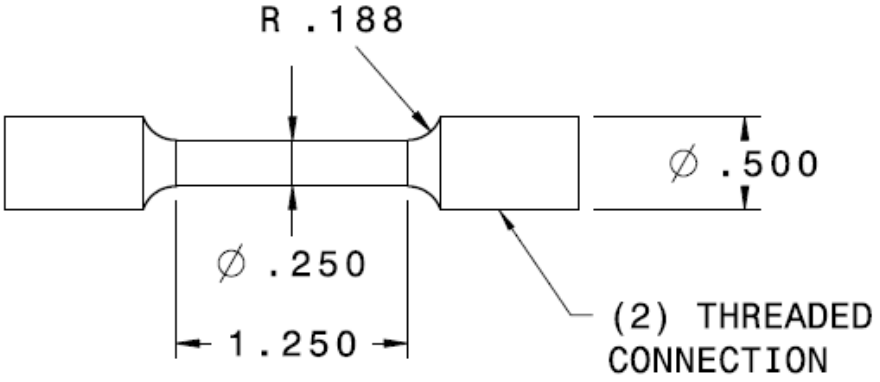

Figure 3.8: Drawing of round tensile specimen
(Dimensioned in inches)

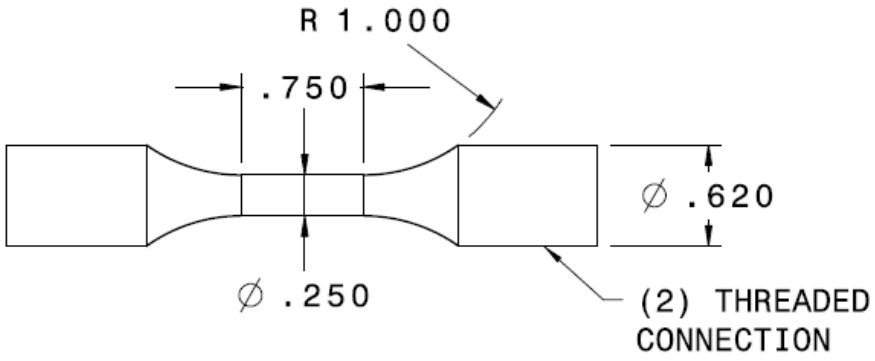

Figure 3.9: Drawing of round fatigue specimen used for S/N curve development
(Dimensioned in inches)

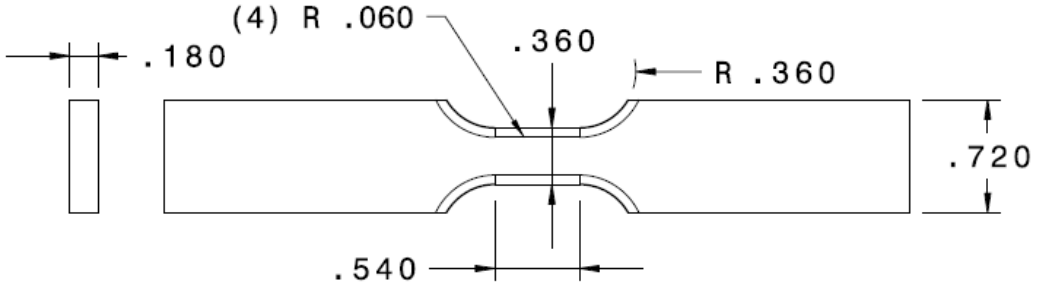

Figure 3.10: Drawing of flat straight gage specimen used for interrupted fatigue testing (Dimensioned in inches)

Specimens for tensile and fatigue testing were extracted both in the longitudinal and long-transverse grain directions. The longitudinal direction was taken as the primary rolling direction, which was the circumferential direction in the case of the forged rings. Only the forged rings had flat plate specimens extracted for DIC, for which the orientations of the gage areas are shown in Figure 3.11. Fatigue specimens were identified as:

‘Grain direction’ - ‘Powder lot’ - ‘Specimen number’

For example, L-A1 refers to a longitudinal specimen from powder lot A. A summary of powder lot letters is given in Table 3.4.

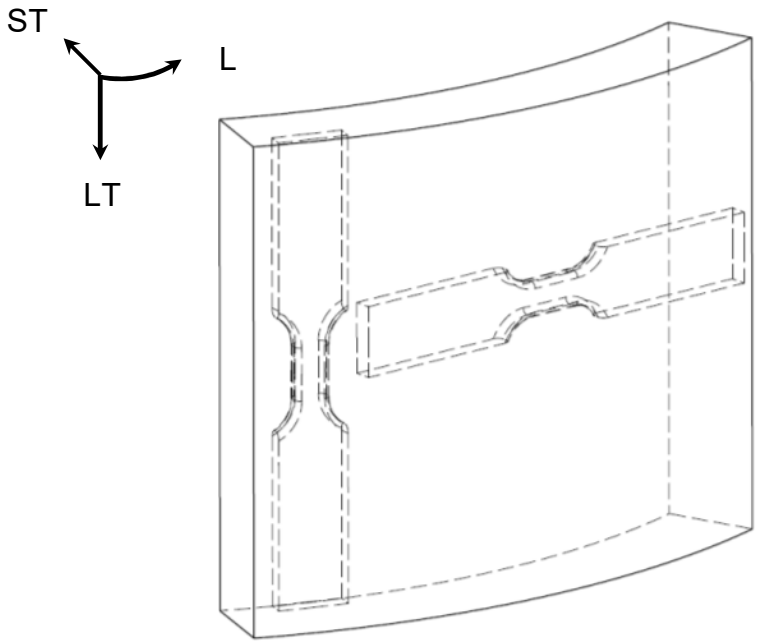

Figure 3.11: Portion of the forged ring showing specimen extraction in the longitudinal and long-transverse directions

Table 3.4: Specimen Identification Matrix

	Grain Directions	Powder Lot	No.
Forged Rings	L, LT	A	2
	L, LT	B	2
Forged Plate	L, LT	C	3

3.3.4 Optical Microscopy

Fracture faces and microstructure samples were examined optically using a compound microscope. Fracture surfaces were ultrasonically cleaned in acetone immediately prior to examination and then handled with gloves. Samples for microstructure evaluation were extracted from the threads of fatigue samples as shown in Figure 3.12. First, a line was scored along the length of the fatigue specimen corresponding to the location of fatigue initiation identified by optical microscopy. Then, samples were sectioned so as to maintain traceability of the crack origin. Samples were metallurgically mounted, ground using silicon carbide paper and polished with OPS + 10% H_2O_2. Examination for residual porosity was done by observing the as-polished surface. Microstructure was revealed by etching in Kroll's Reagent. I-Solution DT software was used for microstructure imaging and analysis of the width, aspect ratio and volume fraction of primary α.

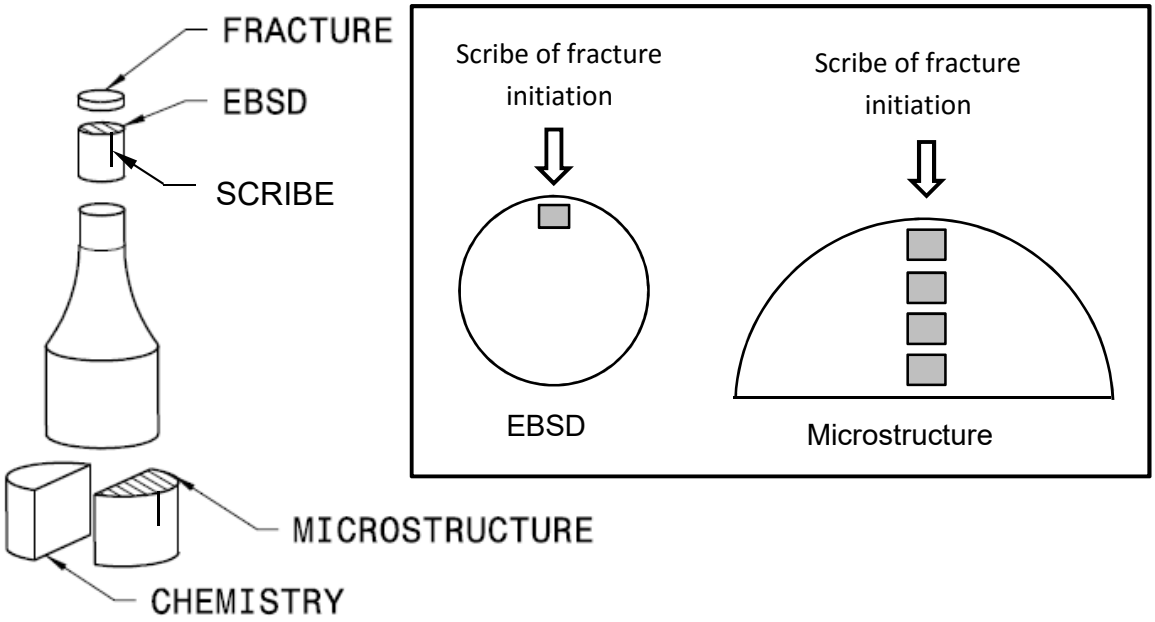

Figure 3.12: Fatigue specimen sectioning diagram for EBSD, microstructure and chemical analysis, and imaging fields of view for EBSD and microstructure

3.3.5 SEM

Fracture surfaces were examined using a Hitachi S3700N scanning electron microscope (SEM) for identification of the failure origin, mechanism and fatigue crack extent. Portions of fatigue samples containing the fracture face were sectioned using a silicon carbide cut off wheel to facilitate handling, ultrasonically cleaned in acetone immediately prior to examination and handled with gloves.

The microstructure samples prepared for optical examination were observed with the SEM for confirmation of porosity. Samples were rinsed with isopropanol and dried with compressed air. Silver paint was applied to the mounted specimen to ensure a conductive path for stable imaging.

Select fatigue samples were examined by electron backscatter diffraction (EBSD) to correlate the role of crystal texture to fatigue propagation. EBSD samples were sectioned 1 – 2 mm (.039 – .079 inch) from the fracture surface, as shown in Figure 3.12, using a Struers precision diamond cut-off wheel. Samples were metallurgically mounted, ground using silicon carbide paper and polished with OPS + 10% H_2O_2. Polished samples were preserved with Sturers RepliSet and broken free of the mount immediately prior to examination. EBSD patterns were gathered with a JOEL JSM-7000F field emission gun-scanning electron microscope (FEG-SEM) equipped with an Oxford Synergy systems EBSD. EBSD post-processing was completed using HKL and Channel 5 software.

3.3.6 Chemistry

Chemistry was measured to explore the role of interstitials on the fatigue endurance limit. Portions of the threads for each fatigue specimen were extracted as shown in Figure 3.12. Analysis for hydrogen was conducted in accordance with ASTM E1447 [53], and oxygen and nitrogen in accordance with ASTM E1409 [54].

CHAPTER 4: EXPERIMENTAL RESULTS

This chapter opens with the results of fatigue endurance testing. The generic microstructure, along with some observed abnormalities, is introduced. Measurements of microstructural features for each fatigue sample, including porosity distribution, are shown, along with chemical variations. Crystal texture maps and strain maps obtained during cyclic loading are presented. Fracture surfaces are characterized and are compared to microstructural features.

4.1 Fatigue Endurance Testing

All round bar, smooth fatigue specimens failed to meet the endurance limit of wrought annealed Ti-6Al-4V: 10 million cycles at 0.41% strain (converted from 67 ksi having a typical Young's modulus of 165 msi [45] [18]). A ratio of the cycles-to-failure versus the endurance limit criterion of 10 million cycles is shown in Figure 4.1 for all specimens tested within a strain range of 0.325% to 0.350%. Samples from the rolled plate in the longitudinal direction had both the best and third worst fatigue performance. Additionally, the Lot A forged ring specimen had a significant improvement in fatigue life for the longitudinal direction, having the second highest life, than in the long-transverse direction, having the lowest fatigue life. However, longitudinal and long-transverse specimens of the Lot B forged ring had similar fatigue lives. Thus, the influence of grain direction and product form is not obvious.

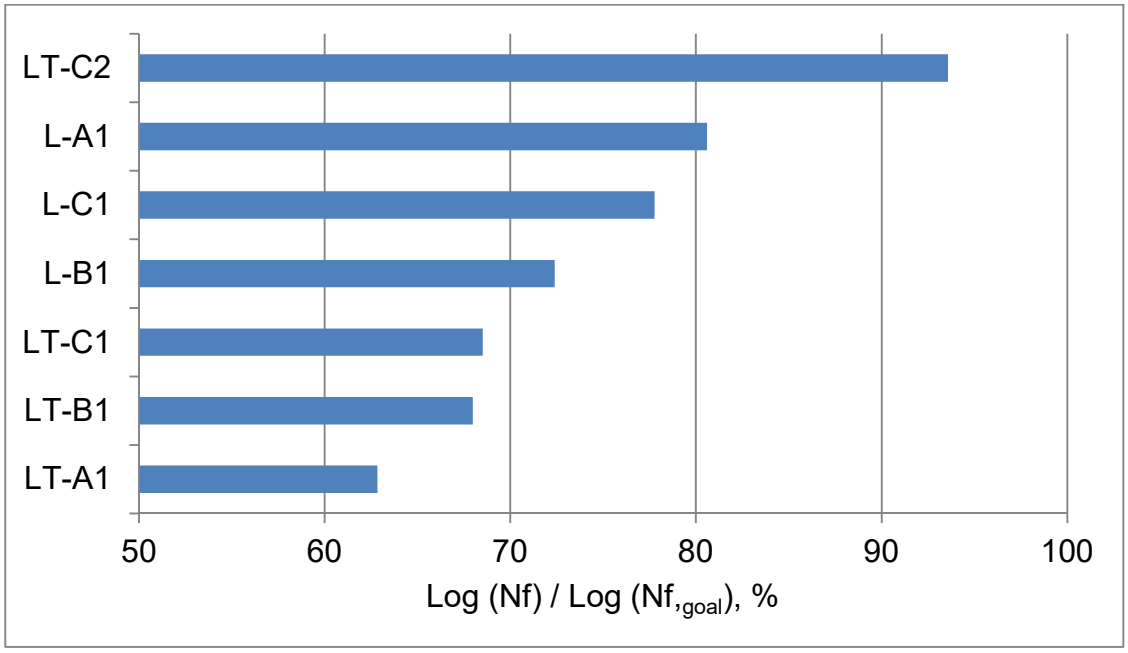

Figure 4.1: Percent difference in (log) failure cycles vs. endurance limit (10 million cycles). R=-1, K_t = 0, round gage, room temperature, 0.325 – 0.350% strain range

4.2 Characterization of Initial Material Condition

4.2.1 Microstructure

The microstructure for all forged product was bi-modal, consisting of primary α grains and lamellar α+β colonies (transformed β). As shown in Figure 4.2, the majority of primary α for the rolled plate was severely elongated in the rolling direction, while the ring forging had slightly elongated primary α. While the lot of ring forgings were to be processed similarly, there were obvious differences in microstructure between forgings and even between fields of view of the same sample. Firstly, for L-A1 only, when viewing in the primary forging (ring rolling) direction, primary α grains were found to be elongated in a swirling pattern as shown in Figure 4.3. In the centre of this field of view, the long axis of elongated

grains can be seen oriented 90 degrees to one another. Secondly, primary α volume fraction and grain size were seen to vary from one field of view to another most notably for the forged rings. An example is shown in Figure 4.4 which illustrates the most extreme variation in microstructure observed (LT-B1). Additionally, regions of the forged rings had primary α grains that were adjacent to one another. This variability in microstructure and primary α interconnectivity was less for the forged plate. However, as only one forged plate sample was provided, it cannot be stated with certainty that microstructure variation would be limited with hot rolling.

While some variation in microstructure between product forms was to be expected, large variations in microstructure for the ring forgings were unexpected. Nonetheless, these microstructural variations are well suited for exploring the relationship of microstructural features on HCF strength.

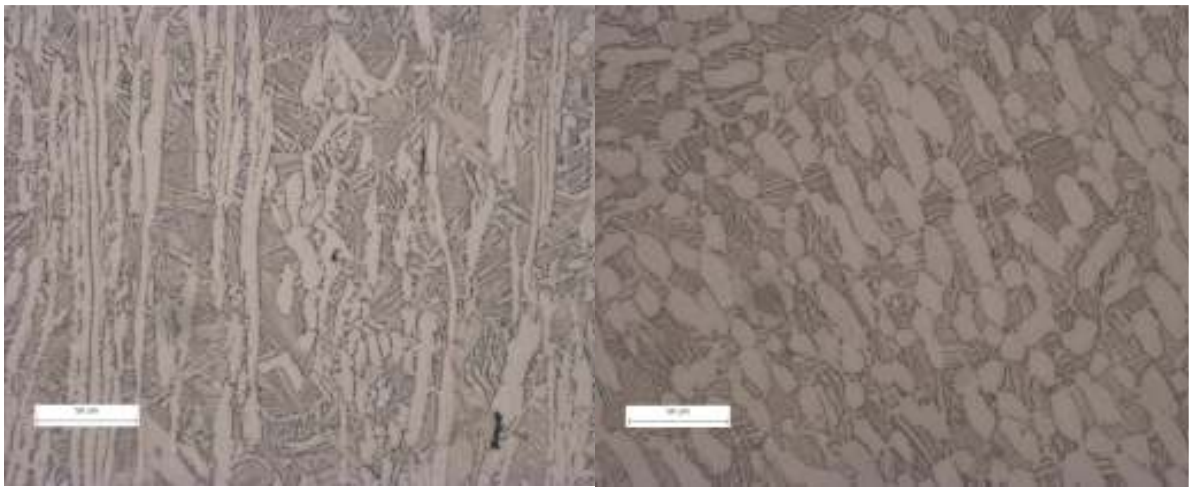

Figure 4.2: Differing microstructure of rolled plate (L-C1) and forged ring (LT-A1)

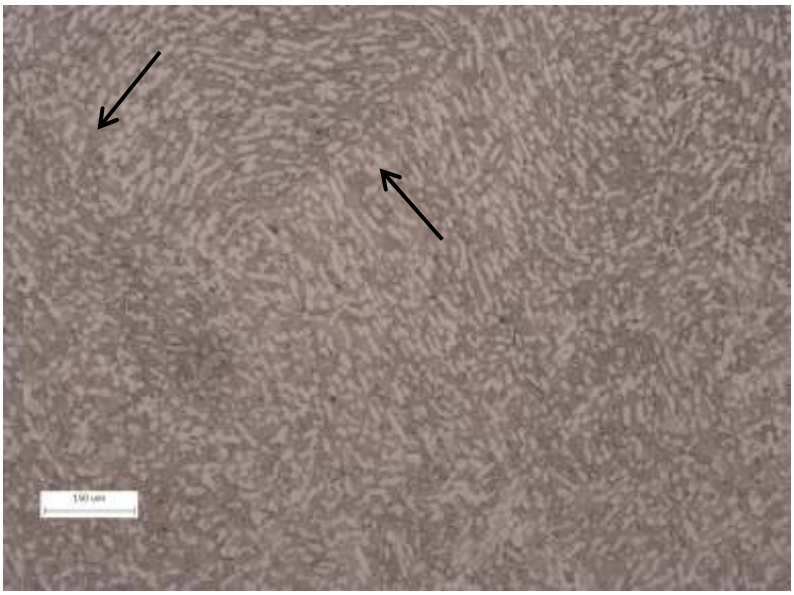

Figure 4.3: Swirling microstructure of L-A1

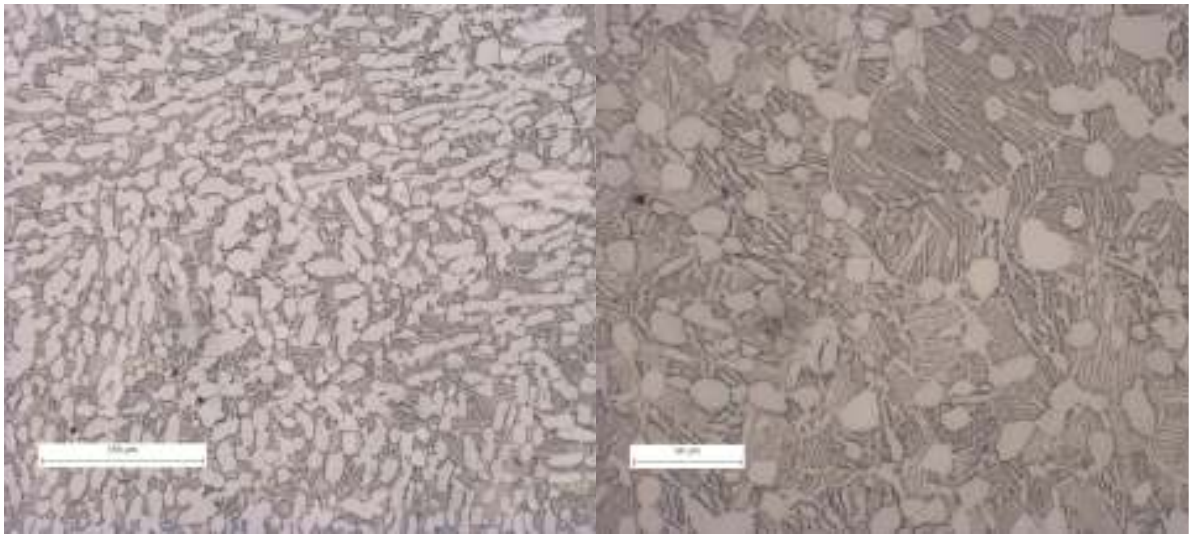

Figure 4.4: Differing view fields of longitudinal LT-B1 having coarse and fine primary α particles

4.2.1.1 Primary α Volume Fraction

Dimensional parameters of primary α were measured by computer imaging software and further manipulated manually as needed, such as to separate conjoining primary α grains at the grain boundaries. The volume fraction of primary α versus cycles-to-failure is shown in Figure 4.5. The primary α volume fraction of forged rings ranged from 39 – 47 %, which was greater than that of the rolled plate, ranging from 29 – 39 %. The variation in primary α volume fraction reported previously among adjoining fields of view was also confirmed, whereby a 20 percent variation in the average value of three fields of view was observed for L-B1.

Variation in grain direction within the same forging was also seen, whereby sample A1 had both the highest and lowest average volume fraction for the forged rings. A trend in grain direction was observed where generally the longitudinal direction had a higher volume fraction than the long-transverse for both product forms.

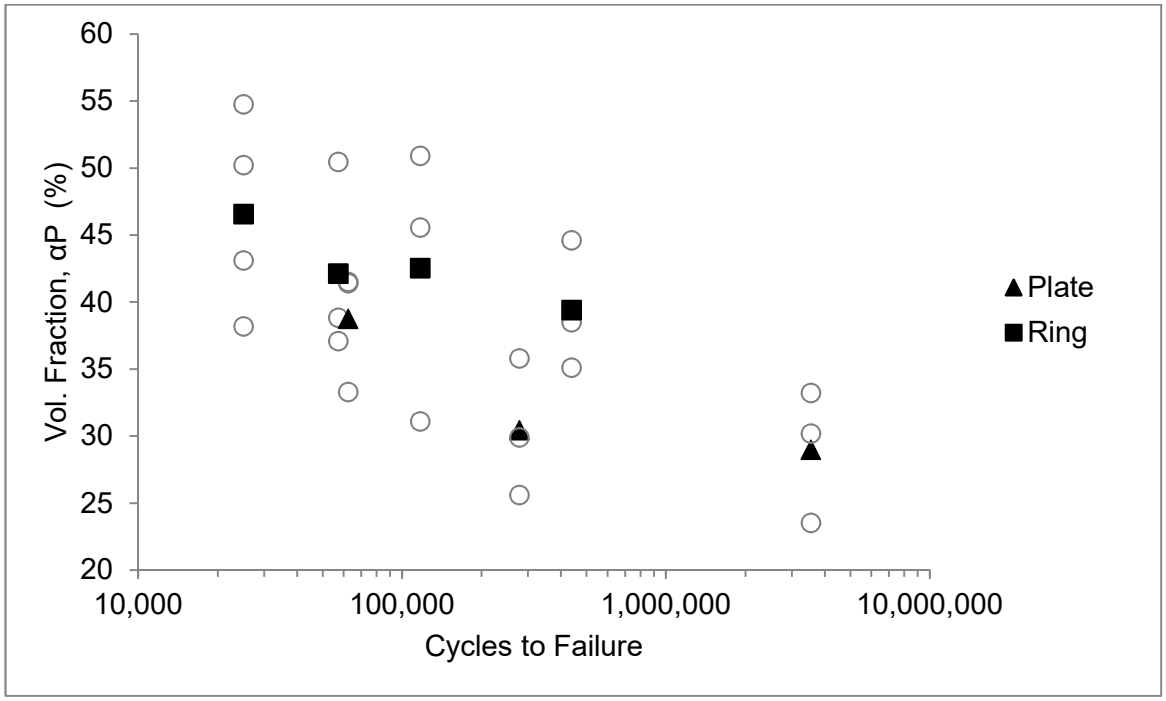

Figure 4.5: Volume fraction of primary α versus cycles to failure. Forged ring has greater variation and higher average than rolled plate. Average value shown by filled icon, individual values shown by open circles.

4.2.1.2 Number of Primary α Grains

The number of primary α grains per field of view versus cycles-to-failure is shown in Figure 4.6. In general, the transverse direction had more primary α grains than the longitudinal direction when considering the same forging lot. Most samples, including those of different product forms, averaged 250 primary α grains per field of view. The exception was the transverse direction of the rolled plate, L-C1, which had 458, and the ring forged sample LT-A1 having 171. The sample with the lowest number of primary α grains per field of view had the lowest fatigue life, although the sample with the highest number of grains had a moderate fatigue life.

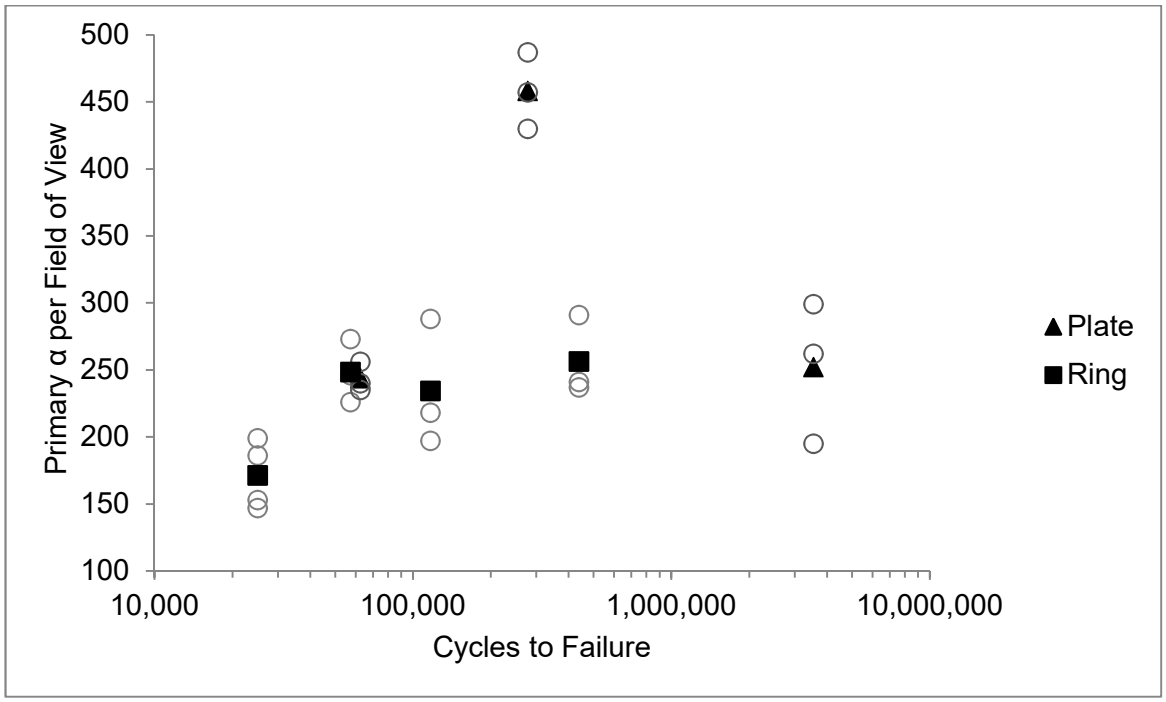

Figure 4.6: Quantity of primary α grains per individual view field versus cycles to failure. Average value shown by filled icon, individual values shown by open circles.

4.2.1.3 Primary α Width

The primary α width versus cycles-to-failure is shown in Figure 4.7. The width was determined as the minor ellipse diameter of an individual grain. The average primary α width of the forged ring ranged from 9.0 – 11.5 μm, which was greater than that of the rolled plate ranging from 4.4 – 6.1 μm. In general when considering the whole population, a decrease in primary α width resulted in an increase in fatigue life.

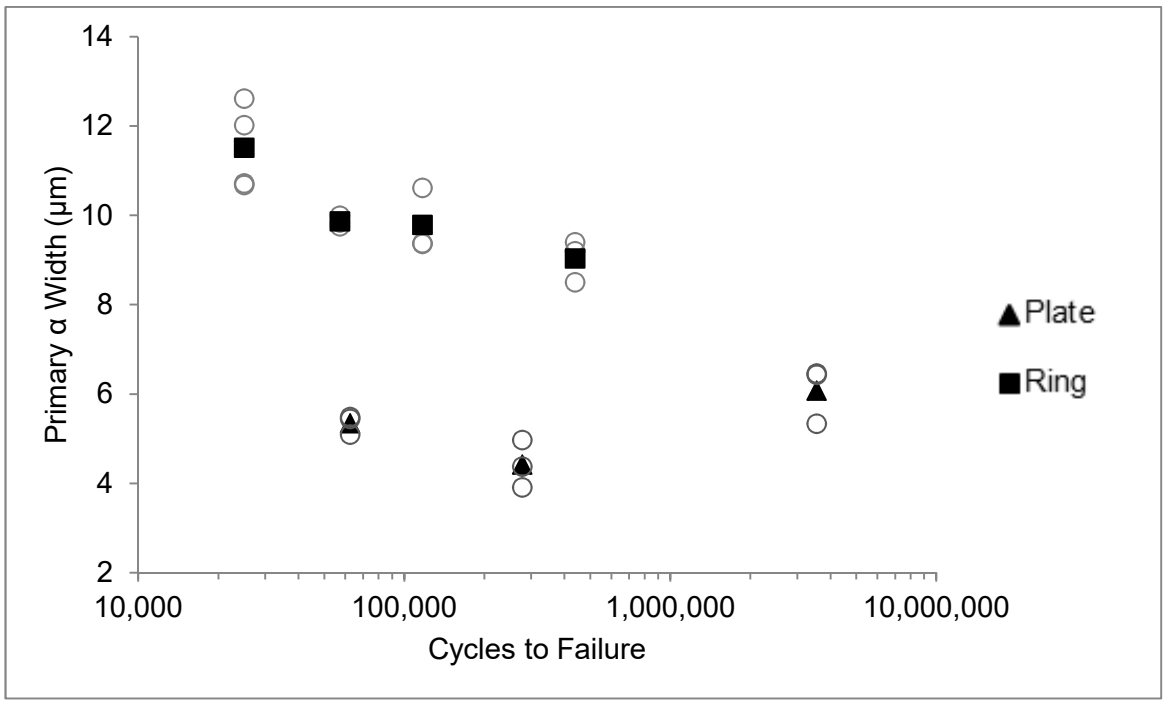

Figure 4.7: Primary α width versus cycles to failure. Average value shown by filled icon, individual values shown by open circles.

4.2.1.4 Primary α Length

The primary α length versus cycles-to-failure is shown in Figure 4.8. The length was determined as the major ellipse diameter of an individual grain. The average values for the forged ring and rolled plate were similar. This was counterintuitive to the visual observation discussed previously as the rolled plate was shown visually to have more elongated primary α grains. However, these severely deformed and elongated primary α grains were fewer than the more numerous, shorter primary α grains. In general, the length of primary α did not appear to influence fatigue life.

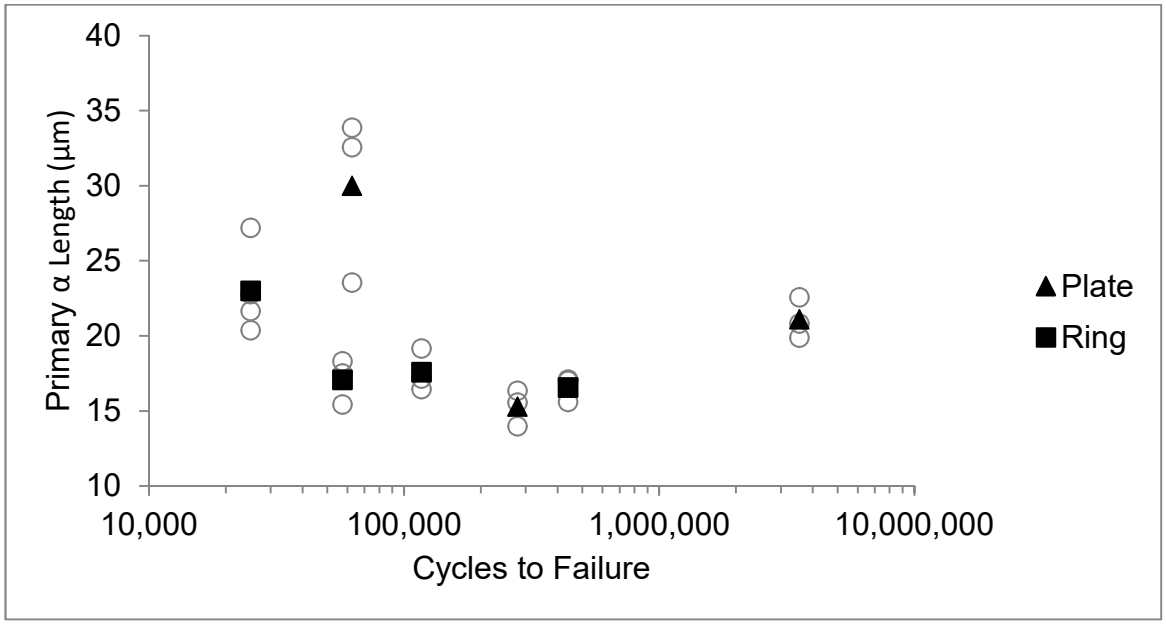

Figure 4.8: Primary α length (ellipse major diameter) versus cycles to failure. Average value shown by filled icon, individual values shown by open circles.

4.2.1.5 Primary α Aspect Ratio

The primary α aspect ratio versus cycles-to-failure is shown in Figure 4.9. The aspect ratio was determined as the ratio of the major and minor ellipse diameter of an individual α grain. The average aspect ratio of the rolled plate was greater than that of the forged ring. This was in line with previous visual observations of severely deformed and elongated grains. Additionally, the aspect ratio was similar for all forged rings in the longitudinal and long-transverse grain direction (approximately 1.8). However, some variability was observed for the rolled plate as transverse sample LT-C1 had a greater average aspect ratio (5.4) than the other transverse LT-C2 (3.5). There was no apparent trend of primary α aspect ratio and fatigue life.

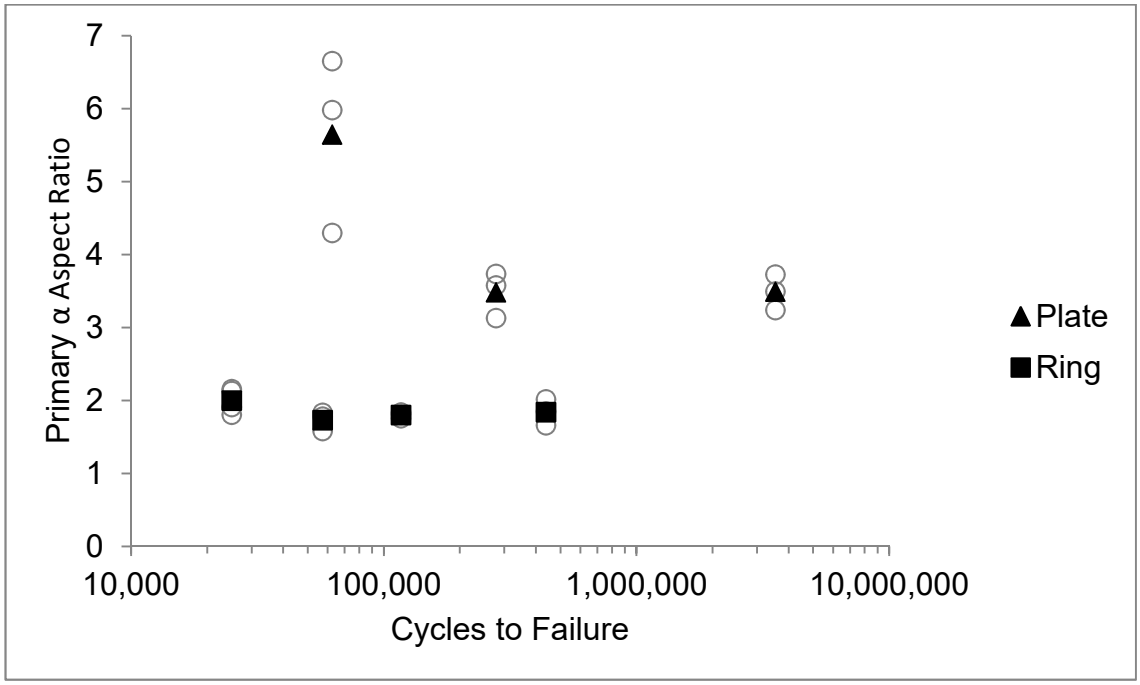

Figure 4.9: Aspect ratio versus cycles to failure for forged ring and rolled plate. Average value shown by filled icon, individual values shown by open circles.

4.2.1.6 Transformed β

The colony size of the transformed β region versus cycles-to-failure is shown in Figure 4.10. A colony was viewed as the region of transformed β that had the same direction of α laths. These measurements were determined manually due to difficulties in automated image analysis. The colony size of the forged ring was on average greater than the rolled plate. Additionally, the longitudinal direction had a greater average colony size (17 μm) than the transverse direction (14 μm) of the same ring forging. Average colony size of the rolled plate varied from 12 to 13 μm, irrespective of grain direction.

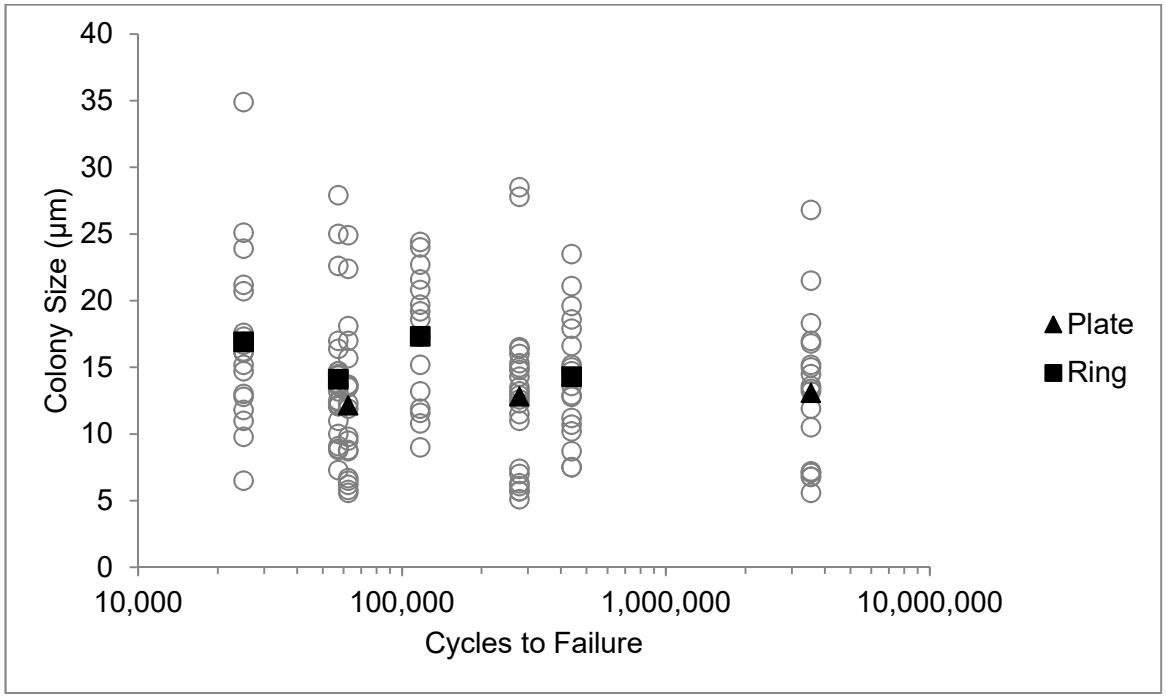

Figure 4.10: Colony size per individual view field versus cycles to failure

The α lath width of the transformed β region versus cycles-to-failure is shown in Figure 4.11. While there was large variation among individual laths, there was little variation in the average lath width, ranging from 1.5 to 3 μm. The different product forms also had similar averages. For the scale shown in Figure 4.11, α lath width did not appear to have an effect on fatigue life.

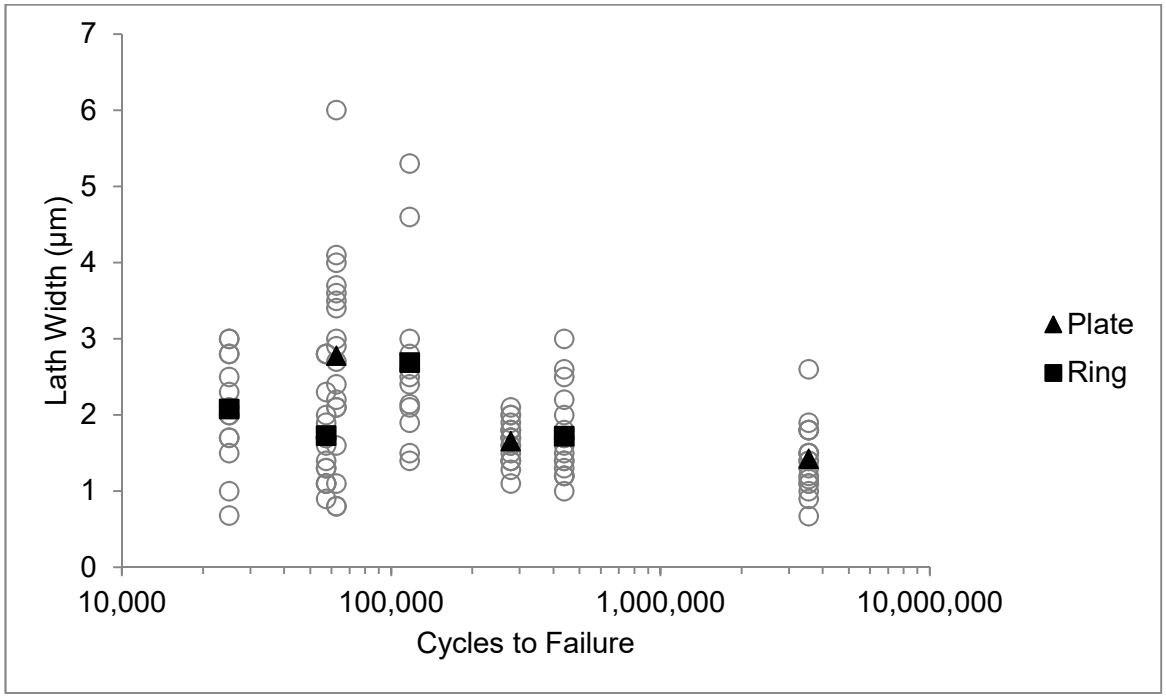

Figure 4.11: Lath width per individual view field versus cycles to failure

4.2.2 Chemistry

The hydrogen, nitrogen and oxygen content for each individual fatigue sample are shown in Figure 4.12. The rolled plate generally had lower hydrogen (61 - 81ppm), oxygen (0.16 wt%) and nitrogen (90 - 120 ppm) than the forged rings (108 – 134 ppm H, 0.19 – 0.22 wt% O, 180 – 440 ppm N). With exception of oxygen for forged ring A1, all were within maximum allowance for IM titanium [48]: 150ppm H, 0.20 wt% O, 500 ppm N. While not measured for each individual sample, the value for carbon was taken from the material certifications as shown in Table 3.3 for forging lots A and B, and 0.009 wt% for forging lot C.

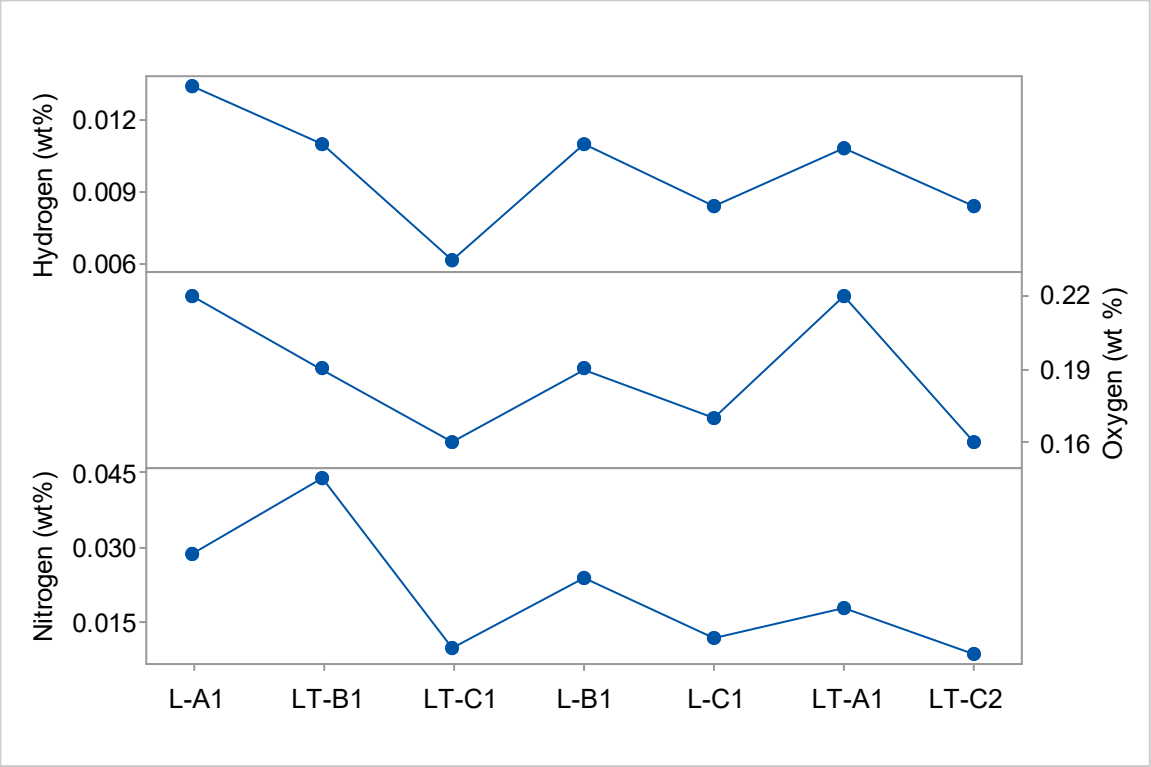

Figure 4.12: Weight percent of nitrogen, oxygen and hydrogen measured in each sample for increasing cycles to failure

4.2.3 Porosity Distribution

Porosity was measured across the whole evaluation area shown in Figure 3.12 by computer imaging software. Pore length was determined as the major ellipse diameter. Results are presented as box plots for which a sketch of common labels and symbols (median, 1st and 3rd quartile [Q1 and Q3] and interquartile range [IQR]) is provided for reference in Figure 4.13. A box plot of pore length is shown Figure 4.14. The majority of measurements, those within Q1 and Q3, ranged between 3 and 17 μm, having a median ranging from 5.9 – 12.4

μm. In all samples, with exception of LT-A1, there existed a single large pore that ranged in size from 27 μm (L-A1) to 38 μm (LT-C1).

A box plot of circle shape factor is shown Figure 4.15. The median ranged from 0.56 (L-A1) to 0.37 (L-C1). The range in shape factor was similar for all samples. Values ranged from near circular (1.0) to flat and elongated (0.1 to 0.2).

As embedded abrasive, contamination or inclusions can have a similar appearance to porosity when viewed with a light microscope (a small, dark feature against a light background), the features identified as porosity for measurement were verified by two methods. Firstly, the feature was verified to have depth with an as-sintered interior appearance by adjusting the focal plane of the microscope. Secondly, a metallography prepared sample was viewed with the SEM. The typical appearance shown Figure 4.16 confirmed these features were pores.

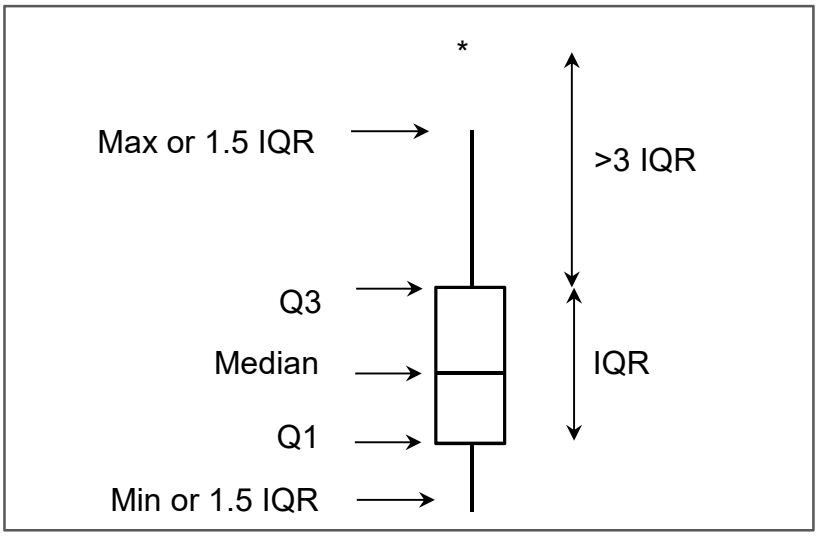

Figure 4.13: Diagram of box plot

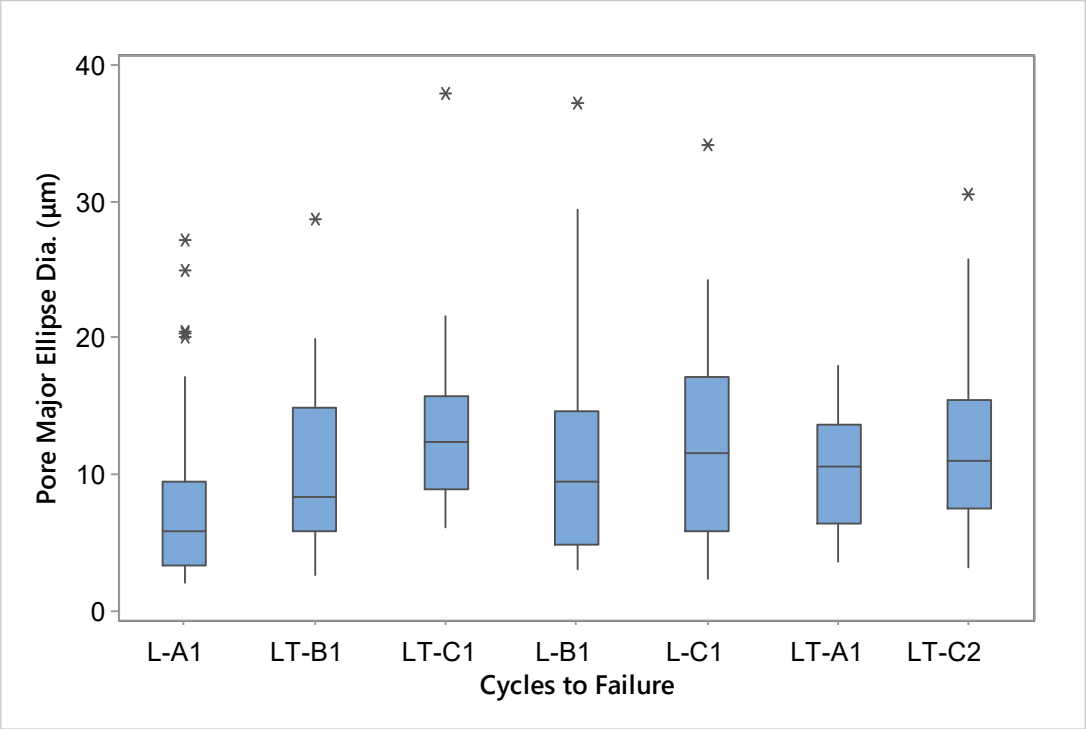

Figure 4.14: Distribution in pore length per sample

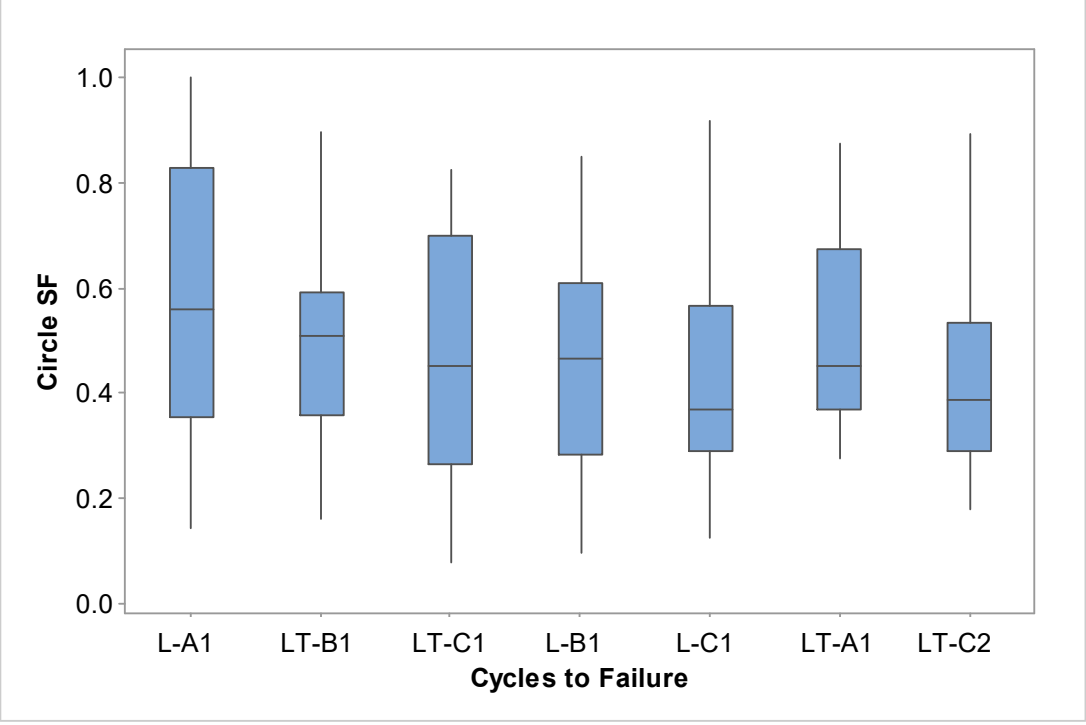

Figure 4.15: Distribution in pore circle shape factor per sample

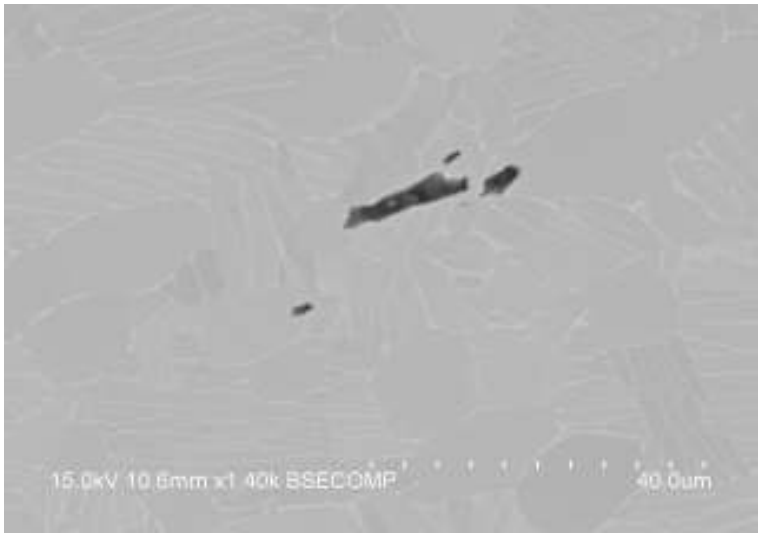

Figure 4.16: SEM-BSE image confirming suspected porosity seen by optical microscope

4.2.4 EBSD

The best and worst performing ring forged samples from endurance testing were examined for texture by EBSD. Inverse pole figure maps for samples LT-A1 and L-A1 are shown in Figure 4.17 and Figure 4.18. The detail (laths) of the transformed β regions was not visible due to the coarse resolution necessary for large area imaging. This would only affected the fraction of β phase detected (1.5%) which is believed to be lower than the true value. Texture component maps of HCP α grains having a basal or prismatic plane orientation within 20 degrees normal to the image (the direction of applied strain) are shown in Figure 4.19. The percent of α with basal planes oriented normal to the image was 7 percent for L-A1 and 5 percent for sample LT-A1. The percent α with prism planes oriented normal to the image was 5 percent for L-A1 and 27 percent for sample LT-A1.

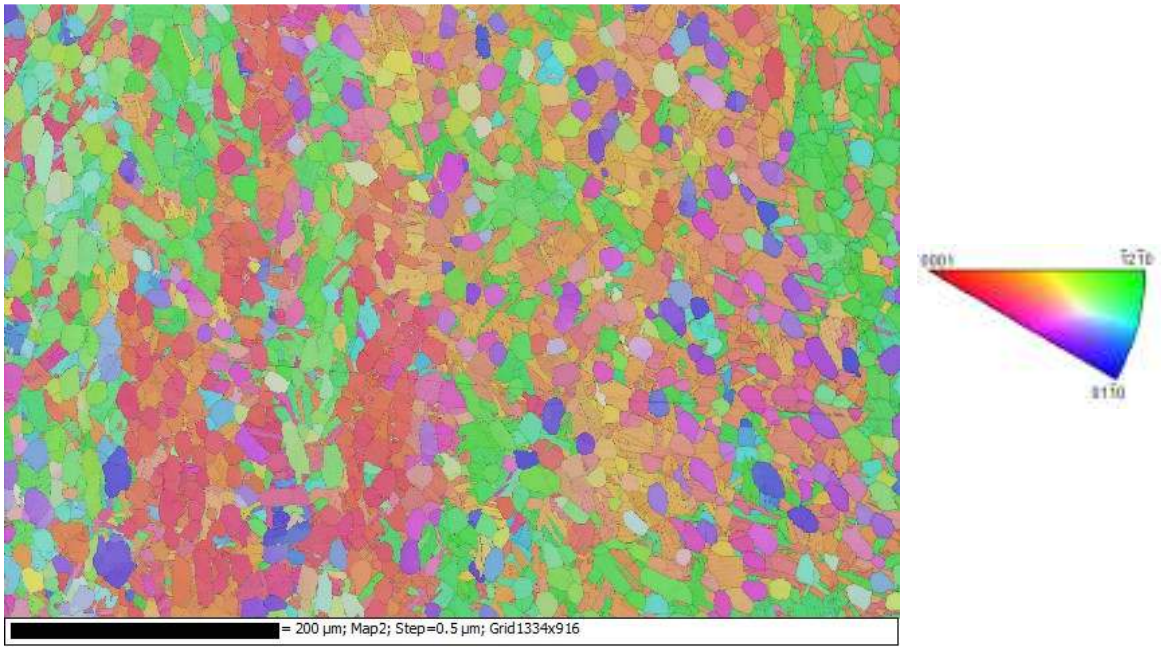

Figure 4.17: Inverse pole figure map of L-A1 in normal direction to applied strain. Crack propagation direction is approximately vertical

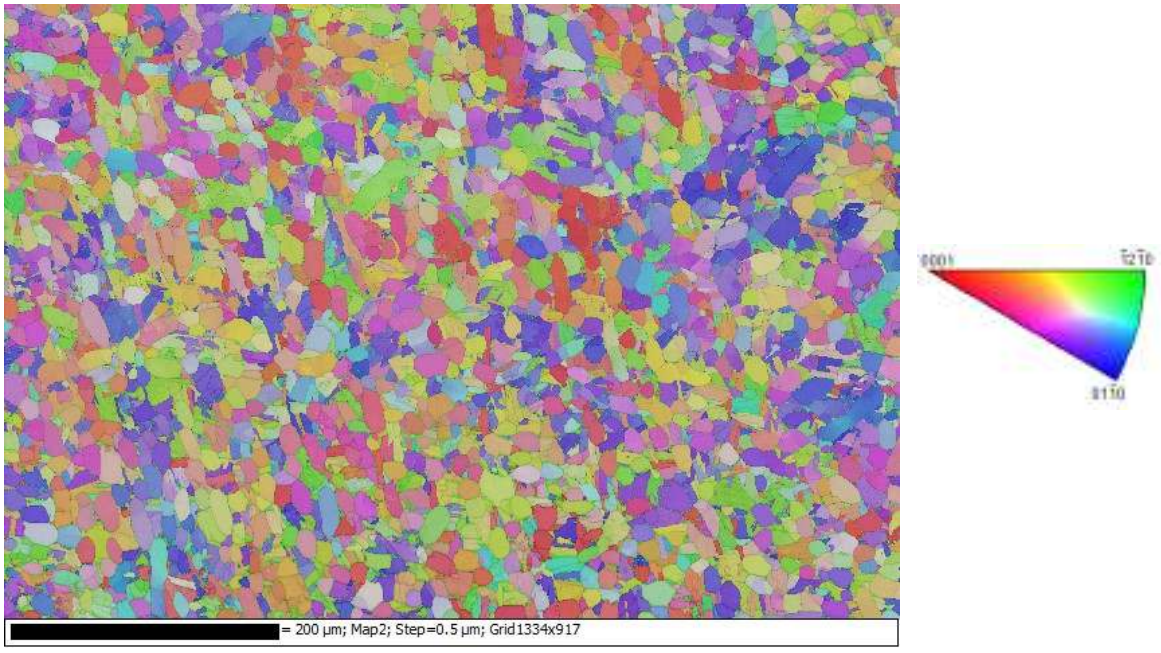

Figure 4.18: Inverse pole figure map of LT-A1 in normal direction to applied strain. Crack propagation direction is approximately vertical

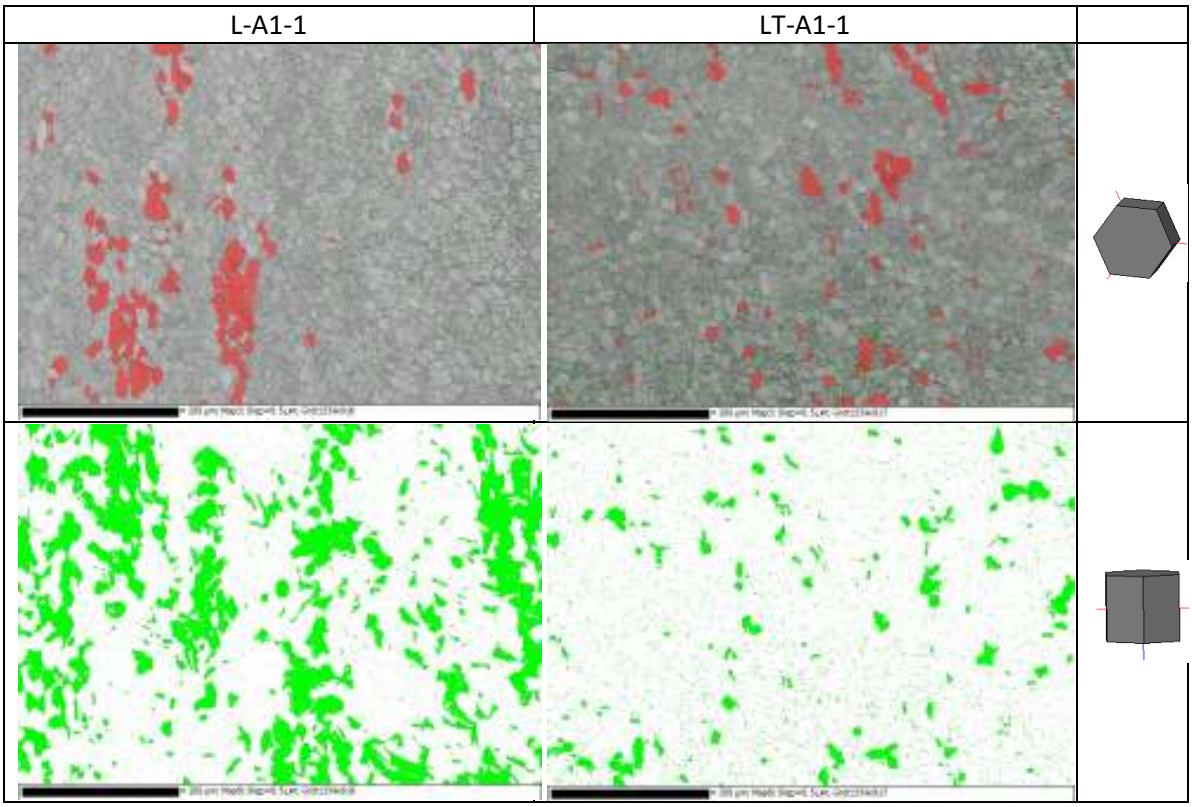

Figure 4.19: Texture component maps of HCP Basal planes (top) and prism planes (bottom) oriented within 20 degrees of the normal axis for ring samples L-A1 and LT-A1

4.3 Fractography

The fracture surfaces were examined for all round gage diameter fatigue samples using the scanning electron microscope. Samples having the 1st, 2nd and 4th longest fatigue lives all had subsurface multi-faceted crack initiation as shown in Figure 4.20 for L-B1. Fracture of sample L-C1, having the 3rd longest fatigue life, initiated from a subsurface pore approximately 50 μm in length as shown in Figure 4.21. The fracture of the sample with the 5th longest life, LT-C1, initiated from a single large subsurface facet shown in Figure 4.22. Fracture of the

remaining two samples having the shortest lives initiated at the surface from multiple facets shown in Figure 4.23 and Figure 4.24. Facets were seen extending nearly 25 percent the across the fracture surface, having the long axis of facets oriented in the direction of crack propagation for LT-B1, and a perpendicular orientation to crack propagation for L-A1.

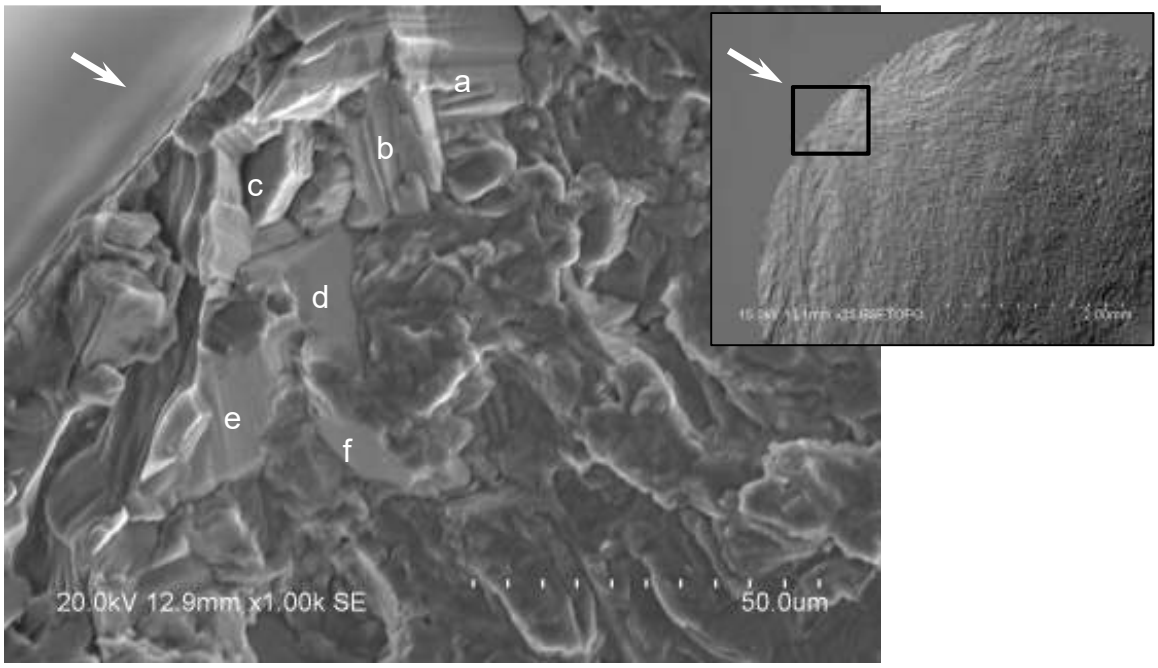

Figure 4.20: Multi-faceted subsurface initiation (facets labelled a through f) of L-B1 (typical of LT-C2, LT-A1). Arrow indicates initiation region

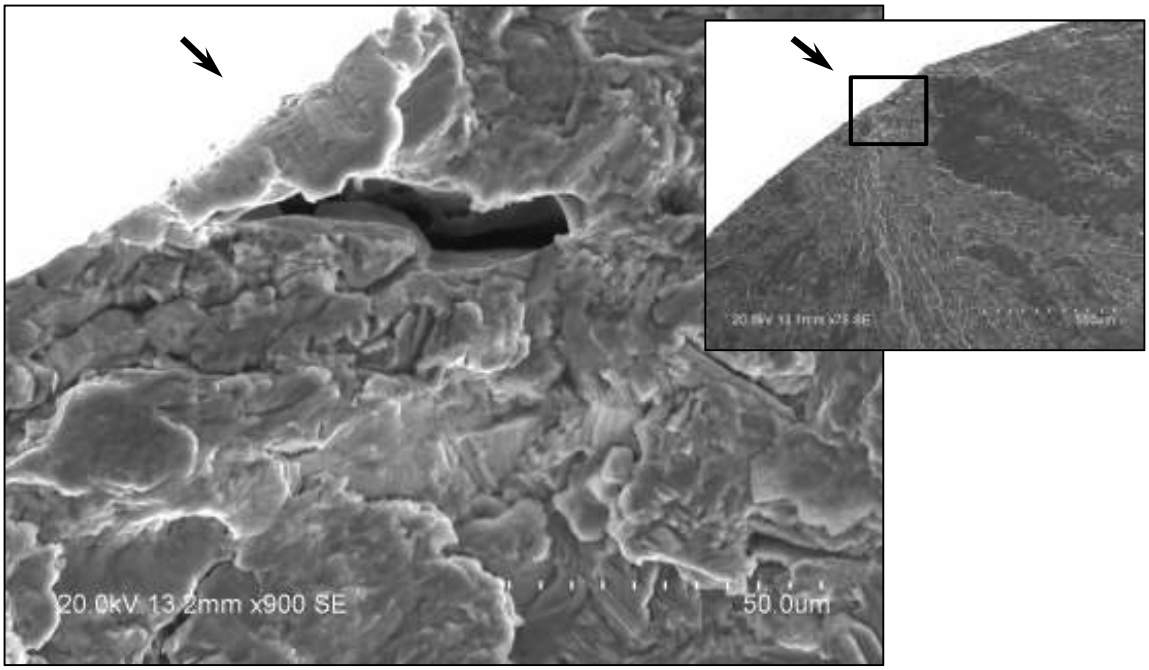

Figure 4.21: Subsurface pore initiation of L-C1. Arrow indicates initiation region

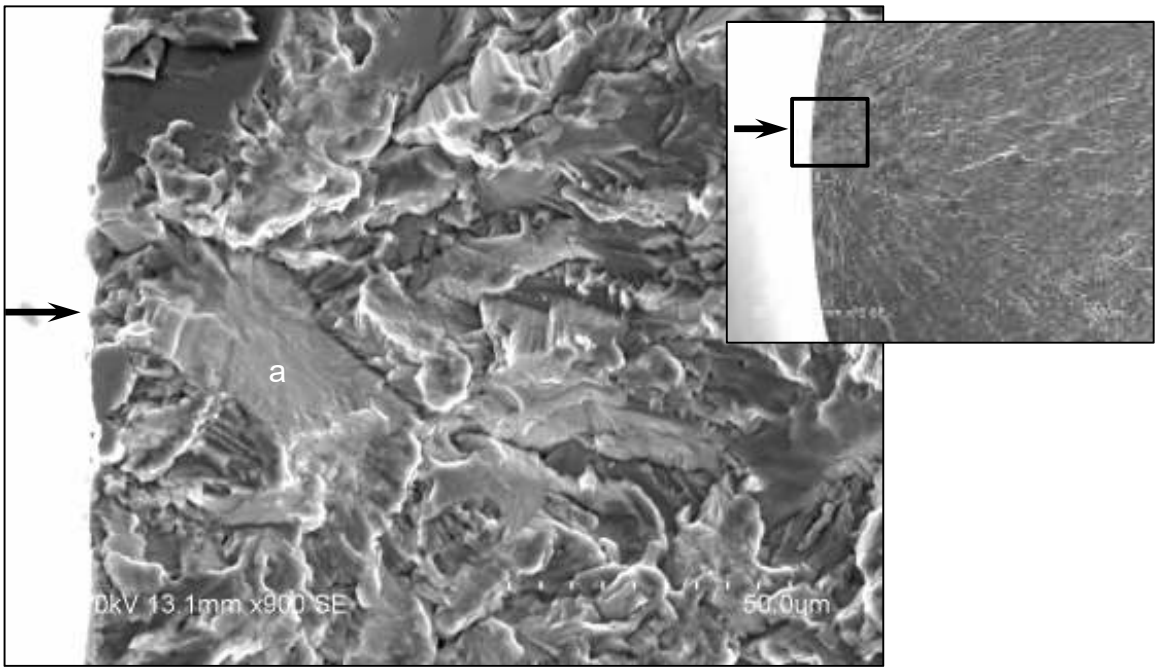

Figure 4.22: Subsurface initiation from single large facet (labelled ‘a’) of LT-C1. Arrow indicates initiation region

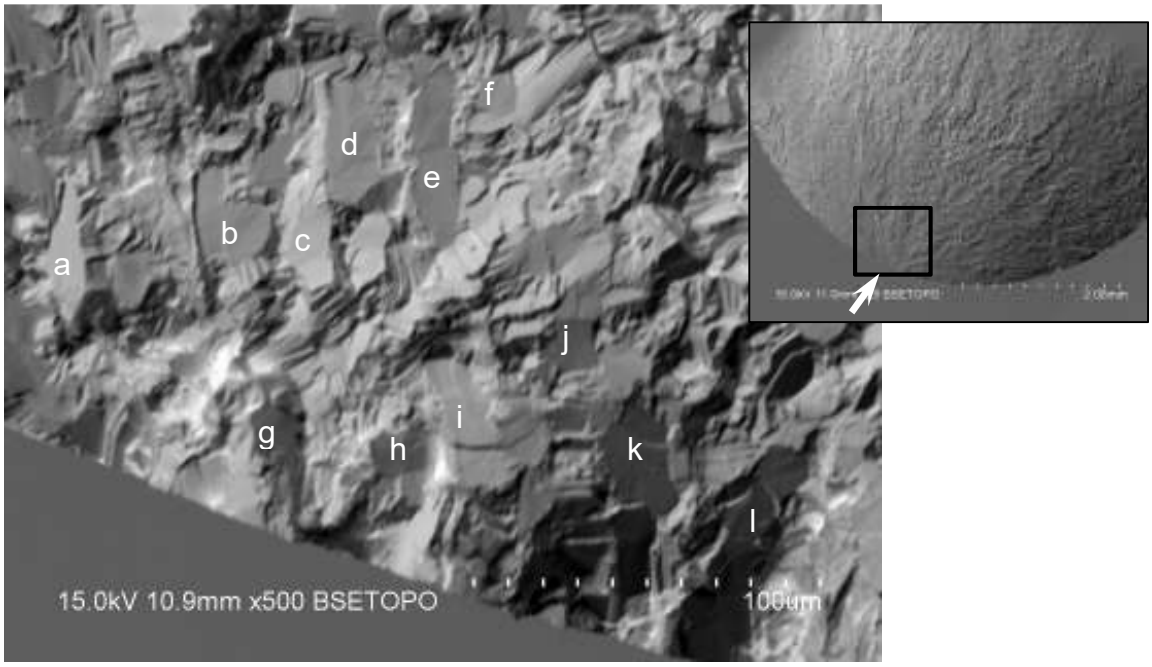

Figure 4.23: Multiple surface initiations and large, multi-faceted subsurface region (facets labelled a through l) of LT-B1. Arrow indicates initiation region

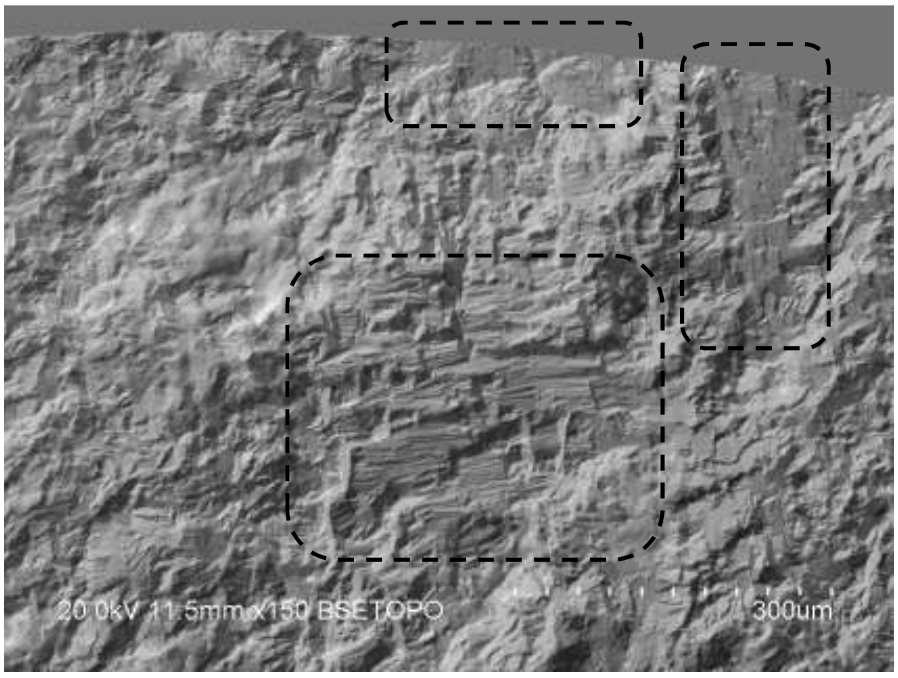

Figure 4.24: Large, multi-faceted surface initiation extending well below surface, and horizontal multi-faceted region subsurface of L-A1. Faceted regions encircled

Faceted features extending along the fracture surface prior to the development of striations (Stage II growth) were seen for all samples as shown in Figure 4.25 through Figure 4.28. The extent of these faceted regions was seen to decrease for samples having progressively longer cycles to failure. The faceted region for the longest lived sample (LT-C2) was limited to the area of initiation. By contrast, fracture surfaces having a moderate fatigue life had a faceted region that spanned a quarter of the fracture surface. Additionally, the sample with the lowest fatigue life, LT-A1, had a faceted region that spanned half of the fracture surface.

Faceted features correlated well to the shape of primary α for the particular sample. As shown in Figure 4.25 for sample LT-C1, the severely deformed and elongated primary α matches that of the ‘snake’ like faceted features typically seen in the plate material. Further, the near circular primary α of the forged ring matches the appearance of the ‘clamshell’ like faceted features in Figure 4.26. These features would have acted as preferential sites for Stage II fatigue striations as shown in Figure 4.27. The elongated ‘pickle’ like facets seen near the initiation site of LT-B1 (refer to Figure 4.23) correlated to elongated primary α, as seen in Figure 4.28.

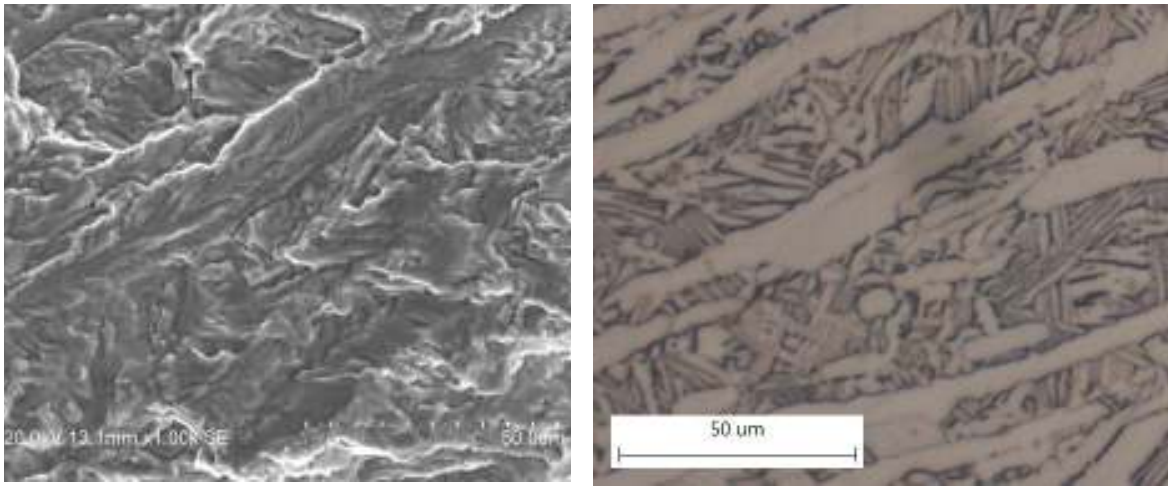

Figure 4.25: LT-C1 SEM fracture face and transverse optical microstructure showing correlation of cleavage feature to primary α strings

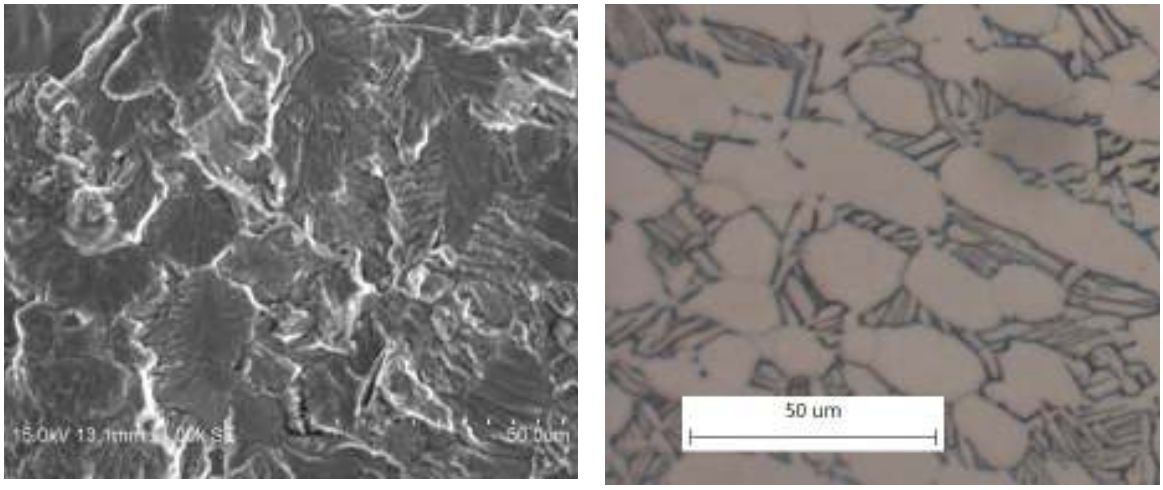

Figure 4.26: LT-B1 SEM fracture face and transverse optical microstructure showing correlation of cleavage feature to primary α

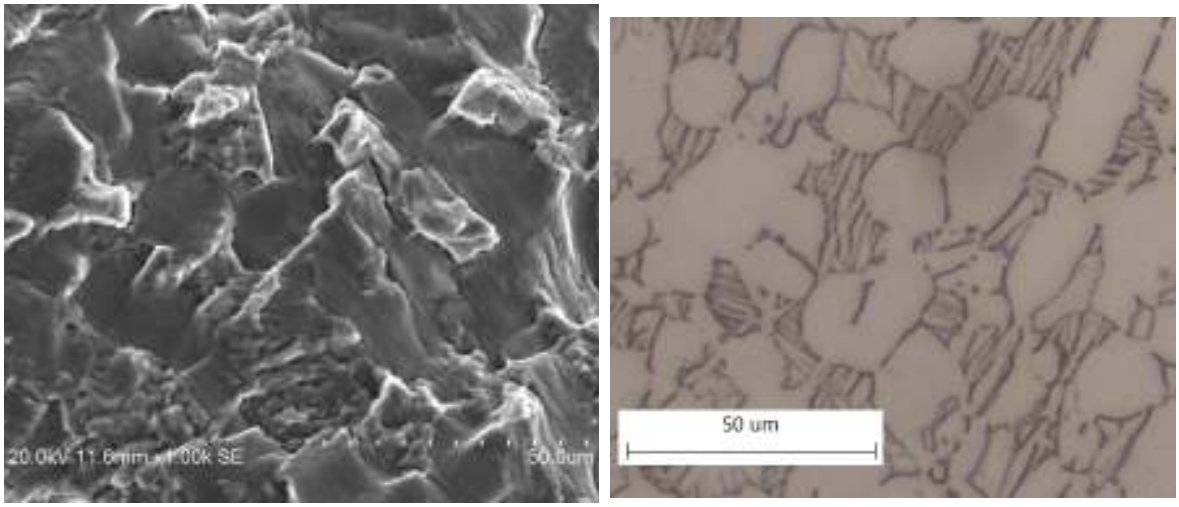

Figure 4.27: LT-A1 SEM fracture face and transverse optical microstructure showing correlation of cleavage feature to primary α

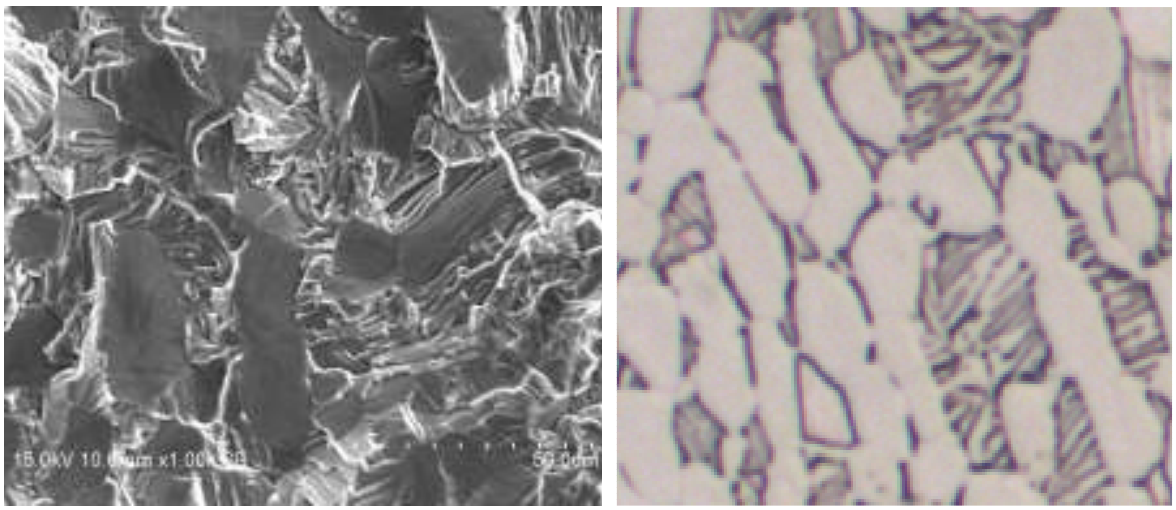

Figure 4.28: LT-B1 SEM fracture face and transverse optical microstructure showing correlation of cleavage feature to primary α

4.4 Digital Image Correlation

The strain map for location 15 is shown in Figure 4.29 for cycle intervals of 8,000 up to failure (8,000, 16,000, 24,000 and 51,925 cycles). Following each interruption, the tracked surface became increasingly scratched, thus the strain map for 32,000 cycles is not shown as the measurement was unreliable. The strain scale was fixed at -1.0 to 1.0 % for ease of comparison and for identifying subtle variations in strain early on. Following failure, the tracked surface was re-polished and etched. Patterns of local strain inhomogeneity developed early in the test and became greater in range as cycling progressed. Variations of strain inhomogeneity were subtle for 8,000 and 16,000 cycles, and then developed into numerous elongated 'hot spots' of tensile and compressive strains at 24,000 and 51,925 cycles. These hot spots were approximately 3 times greater than the applied strain of +/-0.325 %, and spanned multiple primary α grains in the direction of the applied strain.

Location 15 is shown in particular as it was the only region that the crack propagated through, as shown in Figure 4.30. However, due to the fast propagation rate and wide spaced sampling intervals, the crack propagation was not captured. Thus, changes in strain distribution at the crack tip could not be determined.

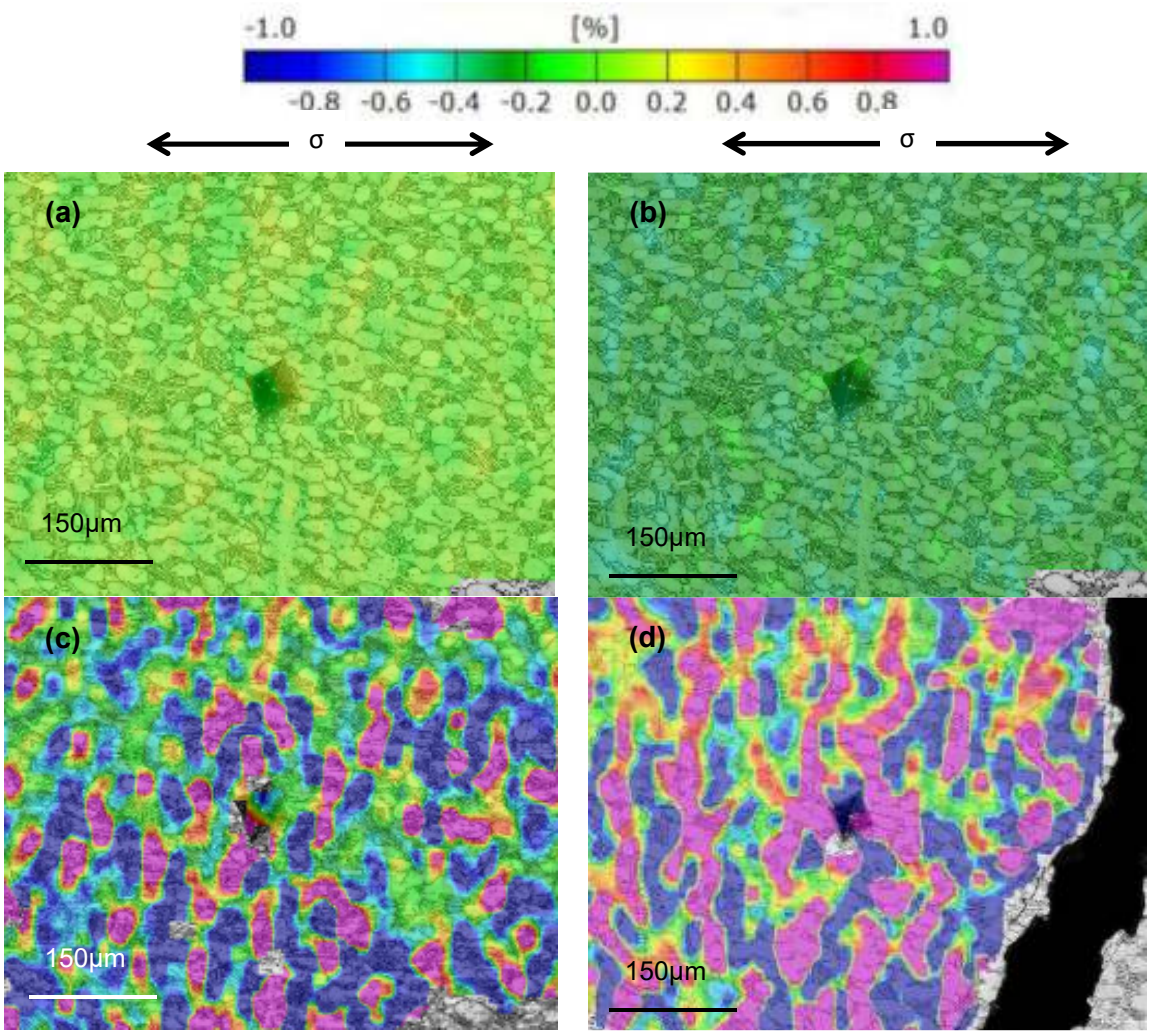

Figure 4.29: Strain map for location 15 at cycles a) 8,000 b) 16,000 c) 24,000 and d) 51,925

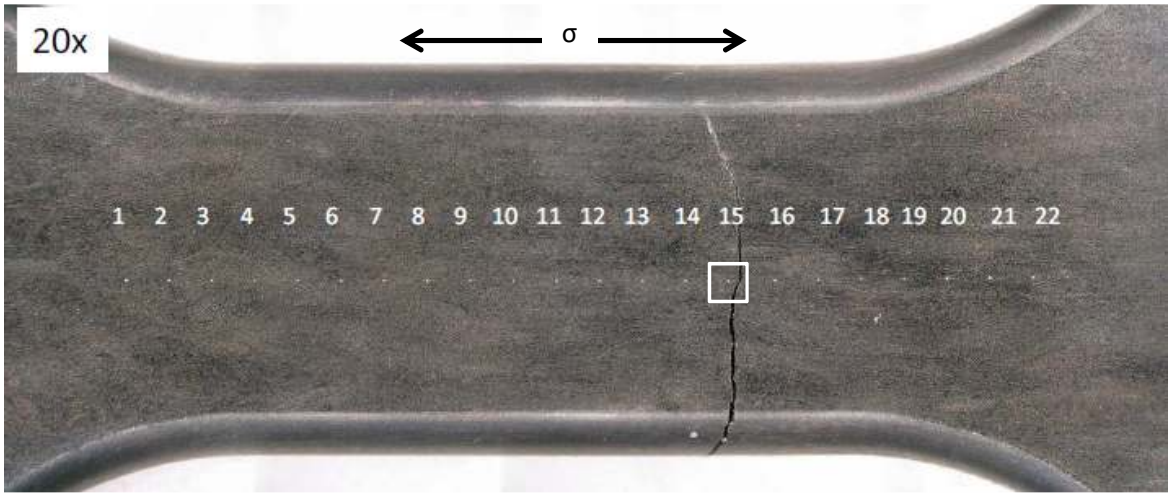

Figure 4.30: DIC specimen after failure. Crack propagation within the tracked Location 15 region

Accumulated global strain is shown for select cycles in Figure 4.31 which covered the full specimen gage length. As the fatigue test was run at complete strain reversal (R = -1), images were captured during both tensile and compressive cycles. Only those images believed to best approximate the peak strain amplitude are shown for ease of comparison. Due to issues with extensometer slippage, samples were run in position control rather than strain control. The target strain of +/- 0.375 % was estimated by moving the upper and lower crosshead and determining the position that resulted in achieving the target strain prior to starting the testing. While the applied target strain was +/- 0.375 %, the scale was fixed to -0.05 to 0.20 %, otherwise strain variations later in life would not be apparent. Numerous localized strain concentrations were observed up to the first few thousand cycles along the length and width of the specimen as shown in Figure 4.31 (a). While the average strain was near the target, localized areas were seen having negative strain with a difference of 0.250 %. After an

additional few thousand cycles, localized strain concentrations were gradually reduced in quantity shown in Figure 4.31 (b). Beyond 7,000 cycles, variations in strain across the width was no longer observed. Rather, a strain gradient was seen across the length of the specimen as in Figure 4.31 (c). The difference in localized strain regions was reduced to approximately 0.10%. An additional few thousand cycles reduced the localized strain gradient difference to approximately 0.030 % as shown in Figure 4.31 (d). It should be noted the images in Figure 4.31 represent the best approximation of the peak strain amplitude as the image recorder and fatigue rig controller were separate units and not linked together. Thus, variations in colour maps were observed within the cycle ranges described but are thought to be snap shots not of the peak strain amplitude.

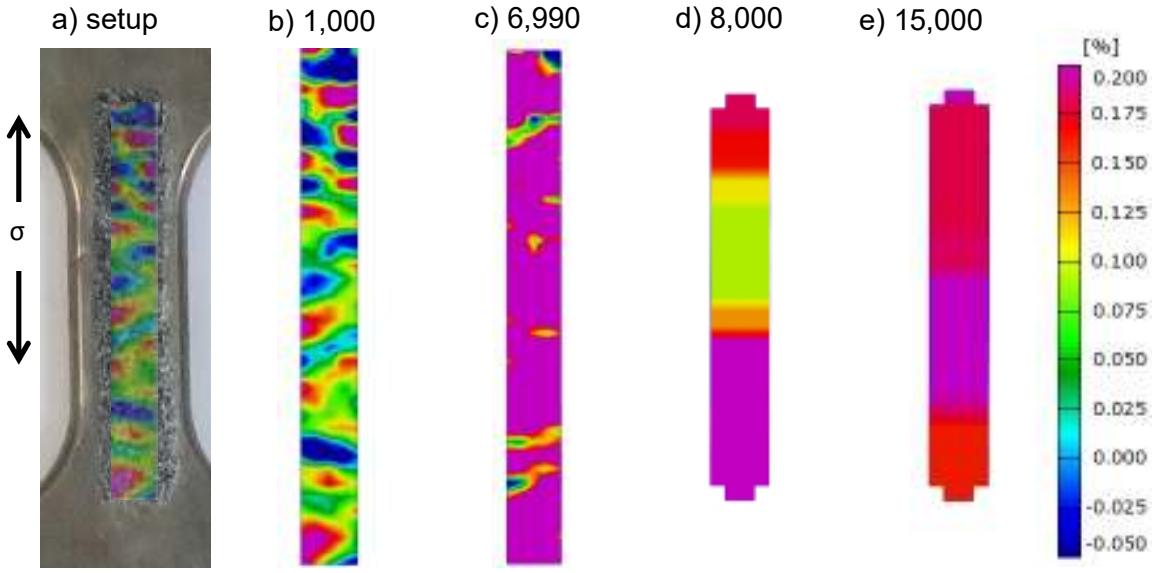

Figure 4.31: Global strain accumulation throughout gage length during HCF testing (a) of LT-B1 for cycles b) 1,000, c) 6,990, d) 8,000, and e) 15,000

CHAPTER 5: DISCUSSION

The goal of this research had three components: 1) to determine what are the dominating feature(s) (predictors) on fatigue life, 2) to determine if residual porosity affects fatigue, and 3) to evaluate combinations of predictors on fatigue life of forged Ti-6Al-4V made from BEPM. Firstly, the significance of microstructural features, interstitials (solute strengthening) and pore size on fatigue life are evaluated each individually by regression analysis. A comparison between texture for fatigue samples having the lowest and highest HCF strength, and a correlation of microstructure to fracture features is also discussed. Secondly, the effect of microstructural features on strain distribution from cyclic loading is reviewed for identification of a crack nucleation driver. Finally, using statistical analysis, combinations of predictors on fatigue life were evaluated, along with their weighting, and the significance compared to individual predictors.

5.1 Effect of Microstructure on Fatigue

A linear regression was performed on all individual microstructure features to determine what feature(s), when considered individually, had the most significant effect on fatigue life. The results in Appendix A show primary α volume fraction ($p<0.05$) was the most significant individual microstructural feature. Fatigue life increased linearly with decreasing primary volume fraction in the range 47 to 28 percent. These findings are in agreement with the literature presented in Chapter 2 specific to IM.

The remaining microstructural features did not have a statistically significant effect on fatigue life ($p>>0.05$). However, visual trends on fatigue life were observed for some features. In general, a decrease in the primary α width, α lath width and transformed beta colony size was beneficial to increasing fatigue life. These variables in combinations with others may aid in 'normalizing' the general trends observed such that they have an influence when considered in combination with other features. In particular, it is of interest to consider primary α width as previous literature on IM Ti-6Al-4V [19] has shown a correlation to fatigue life.

The visual trend in the number of primary α particles is of particular interest. With exception of sample L-C1, an increase in the number of primary α particles increased fatigue life. Yet sample L-C1, having the smallest primary α grain size yet twice as many primary α particles as the average, only achieved an average fatigue life. This observation of particle count may be related to a particle spacing threshold, beyond which primary α grains will impinge on one another. Adjoining primary α grains may then act as a single unit for slip, thus mitigating the benefit of a refined grain structure. When performing a statistical analysis on a combination of predictors of fatigue life, the number of primary α particles is therefore of interest.

It was shown that primary α volume fraction alone is an adequate predictor for fatigue life. However, from observations of visual trends for other variables, namely primary α width and number of primary α particles, it is of interest to

consider inclusion of additional terms when performing statistical analysis on fatigue. Further, the role of porosity must be explored before proposing that porosity does not affect fatigue, as would be implied by the regression analysis of primary α volume fraction.

5.2 Effect of Pore Size on Fatigue

Residual porosity inherent of the PM process was shown to influence fatigue life of PM Ti-6Al-4V in Chapter 2. A linear regression analysis of the average porosity length, determined as the pore major diameter, was performed to ascertain whether this relationship applied for the forged BEPM Ti-6Al-4V material of this study. The result in Figure A.10 shows porosity length was not a suitable predictor for fatigue life (p>>0.05). Additionally, the observed trend was that an increase in the pore length favoured an increase in the fatigue life. Intuitively, this observation appears fundamentally flawed and requires additional insight to explain the observed behaviour.

Previous attempts have been made to correlate porosity size to the fatigue endurance limit of Ti-6Al-4V made from PM. Ivasishin et al. [55] used the following model for on the endurance limit of HIPed Ti-6Al-4V made from titanium hydride powder:

$$\sigma_{-1} = \frac{\Delta K_{\text{th eff}}}{Y\sqrt{d}} \tag{2}$$

Where σ_{-1} is the endurance limit of a smooth specimen, $\Delta K_{\text{th eff}} = BE$, with B being a constant and E the Young's modulus, Y a function of the crack size and loading

conditions, and *d* the linear dimension of porosity. Ivasishin noted individual pores ranged from 50 to 60 μm, having an average value of 10 μm, which is similar to the range found in this study. However, the number of pores per field of view was greater in Ivasishin's work. Using the average porosity size, the calculated endurance limit was conservative when compared to the actual tested value. Nonetheless, the model was concluded to be valid. The argument is that holding constant all other variables, decreasing the pore diameter will increase the endurance limit. While intuitive, this observation of pore size on HCF strength does not agree with the observation for the material of the present study. Two possibilities are suggested, either there is a threshold value for porosity size, below which a crack will not nucleate, or, there is a competing structural parameter whose effect is greater than that of porosity.

To explore the function of porosity size on fatigue life, the maximum observed pore size from each sample from Figure 4.14 is firstly considered. The maximum pore length, determined as the major ellipse diameter, is shown in greater detail in Figure 5.1. The only sample that failed due to a fatigue crack that initiated from a pore, sample LT-C2, is also seen to have the largest pore, measuring at 50 μm. Thus, beyond a certain value, the size of porosity must have an influence on fatigue life. This 50 μm value was taken as the pore length on the fracture surface which nucleated the crack. Otherwise, the maximum size measured from metallography was 31 μm. In consideration of other samples, it cannot be stated with certainty that the largest pore measured by metallography

was indeed the largest for that sample. However, all maximum values from Figure 4.14, with exception to LT-A1, were well beyond the distribution range of the pores observed, with maximum values being separated by multiples of the IQR. This separation in IQR implies these large pores observed were a rarity, but otherwise were observed and are a valid measurement. Thus, the maximum values of the pores observed can be considered typical of the maximum value within the specimen.

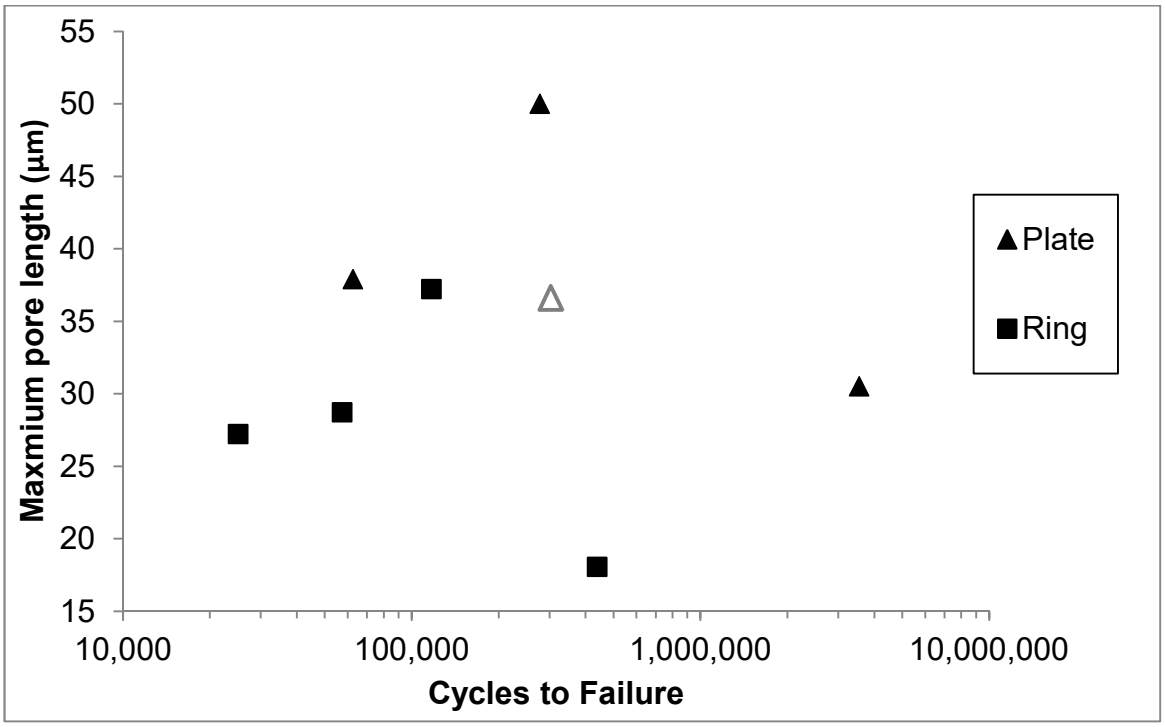

Figure 5.1: Maximum observed pore size (major ellipse diameter) of sintered and forged Ti-6Al-4V vs. cycles to failure at 0.325 – 0.350% strain. Maximum size measured from the microstructure of L-C1 (grey icon) corrected from the pore size seen on the fracture surface

In exploring the function of porosity on fatigue life, the concept of a competing microstructural parameter whose effect is more damaging on HCF

strength than the porosity is now considered. It is known that primary α volume fraction and/or width is the primary factor for HCF strength of IM, whereas for cast or otherwise porous material, the primary factor is the pore size. The microstructure of the material studied can be considered to lie between cast and IM. Therefore, the governing properties on HCF strength could also be considered to be a hybrid of the two, coupling both primary α volume fraction and pore size. In considering equation 2 proposed by Ivasishin et al., by limiting the structural parameter *d* in equation 2 to only porosity, it has not taken into account that other microstructural features may be the dominating feature for HCF strength. The validity of the concept for coupled microstructural parameters influencing HCF strength thus remains unanswered.

In applying the two preceding observations, it becomes necessary to identify possible competing structural parameters. From the literature on the HCF of IM in Chapter 2, it is known that primary α volume fraction and width were primary predictors of fatigue. Secondly, primary α volume fraction, when considered separately, was found to have a statistically significant linear correlation to HCF strength. Thus, the mechanism driving HCF strength of IM, together with that for a porous structure (the size of porosity), may have a combined influence on HCF strength. It is proposed that, should primary α volume fraction/width be sufficiently large, it may overshadow the benefits of having small pores. Similarly, larger pores may not be as detrimental to HCF strength if there is a refined microstructure of primary α volume fraction/width.

In Chapter 2, it was discussed how the (circularity) shape factor, F, of a pore was a suitable predictor of fatigue life as it correlated to the stress intensity of that pore. By definition, the shape factor ranges from 0 to 1. It is a quantity to describe the roundness of an object where a value of 1 is perfectly circular, and values decreasing closer to zero are increasingly linear, have rough edges, or both. The shape factor calculated for all pores previously in Figure 4.15 showed similar scatter, ranging generally from 0.1 to 0.9. Samples having the lowest average porosity shape factor did not result in the lowest fatigue life. Rather, there existed a visually decreasing trend in the average shape factor that generally improved fatigue life as shown in greater detail in Figure 5.2. Linear regression confirmed that the average pore shape factor was a suitable predictor of fatigue life ($p<0.05$, Figure A.9). This trend contradicts results of Yan [39] where for HIPed Ti-6Al-4V made from HDH and Armstrong powder, samples having the lowest shape factor (i.e. highest stress intensity) were found to have the lowest fatigue life. All of Yan's fatigue failures initiated cracks from pores, whereas only one sample in this study initiated a fatigue crack from a pore, it suggests a threshold value for porosity size below which fatigue life is not dictated by porosity, regardless of the shape factor. The observed trend in porosity shape factor is therefore determined to be an ineffective predictor of fatigue strength for this material.

An additional consideration of the counterintuitive trend in pore shape factor is that it is an indication of the degree of thermomechanical work. It was observed how the distribution for the average values of primary α volume fraction (Figure

4.5) and pore shape factor (Figure 5.2) were similar. As primary α volume fraction is dependent on the thermomechanical history, it is possible the same mechanism applies to the pore shape factor. An elongated pore could thus be related to a greater amount of thermomechanical work. It is understandable to argue an increase in thermomechanical work should heal pores, becoming more circular. However, it is possible the elongated pores that remained were unable to be fully healed due to entrapped gas or another mechanism. In consideration of the pore shape factor a correlation to the amount of mechanical work, the trend on fatigue strength then becomes intuitive.

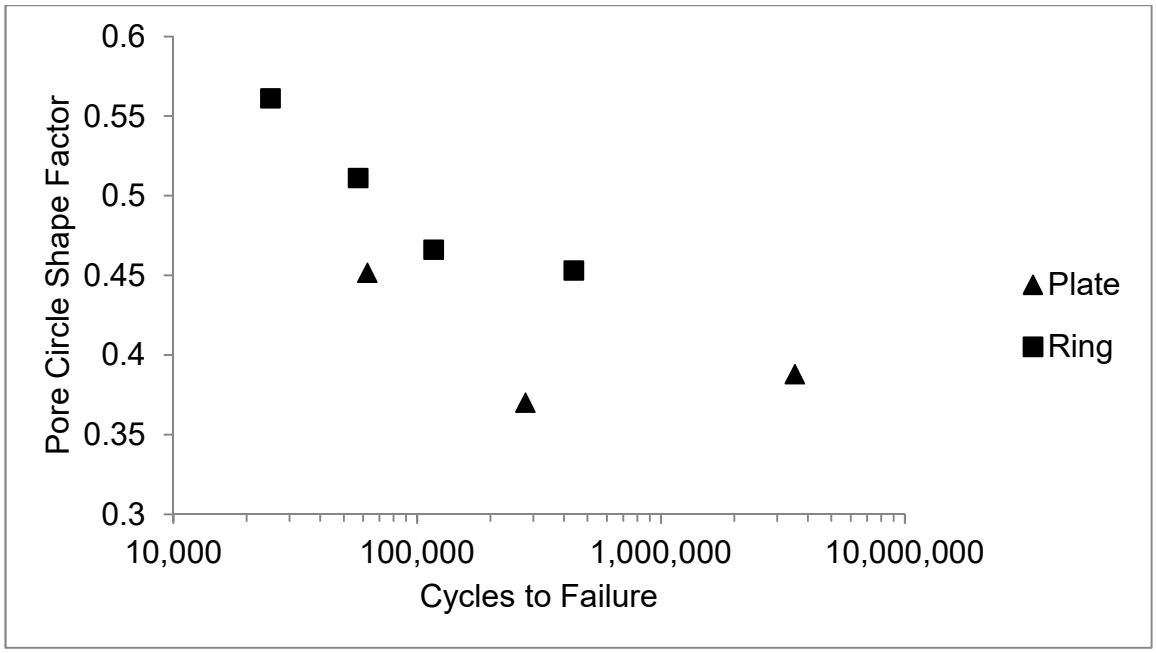

Figure 5.2: Pore shape factor (circularity) of sintered and forged Ti-6Al-4V vs. cycles to failure at 0.325 – 0.350% strain

5.3 Effect of Interstitials on Fatigue

As the hydrogen content was beyond the industry recommended maximum (150 ppm) after heat treating in air, it was of interest to investigate whether vacuum degassing was successful to reduce the hydrogen content so as not to influence fatigue life. As was shown in Figure 4.12, the hydrogen content of each sample after vacuum degassing was below 150 ppm. Further, the fracture surfaces did not show evidence of intergranular fracture, typically associated with hydrogen embrittlement. Thus, the vacuum treatment was successful at reducing the excessive hydrogen content.

When considered separately, oxygen, and nitrogen showed little correlation to fatigue life, as was shown for the individual plots of oxygen and nitrogen in Figure 4.12. However, in Chapter 2 it was discussed that oxygen, nitrogen and carbon have a combined, additive effect on strength and hardness. Thus, it is more beneficial to plot the oxygen equivalent (OE) versus fatigue life. As shown in Figure 5.3, a trend is observed whereby a decrease in the OE, from 0.33 to 0.19, resulted in an increase in fatigue life. Recall that carbon was not measured from for each individual sample, but rather taken from the materials certifications.

A regression analysis on OE (Figure A.8) showed the effect on fatigue life was not significant ($p>0.05$). However, the result from regression analysis does not indicate whether the OE, in combination with another variable, may result in an improved correlation for fatigue life. It is therefore of interest to investigate further the trend of decreasing OE on increasing fatigue.

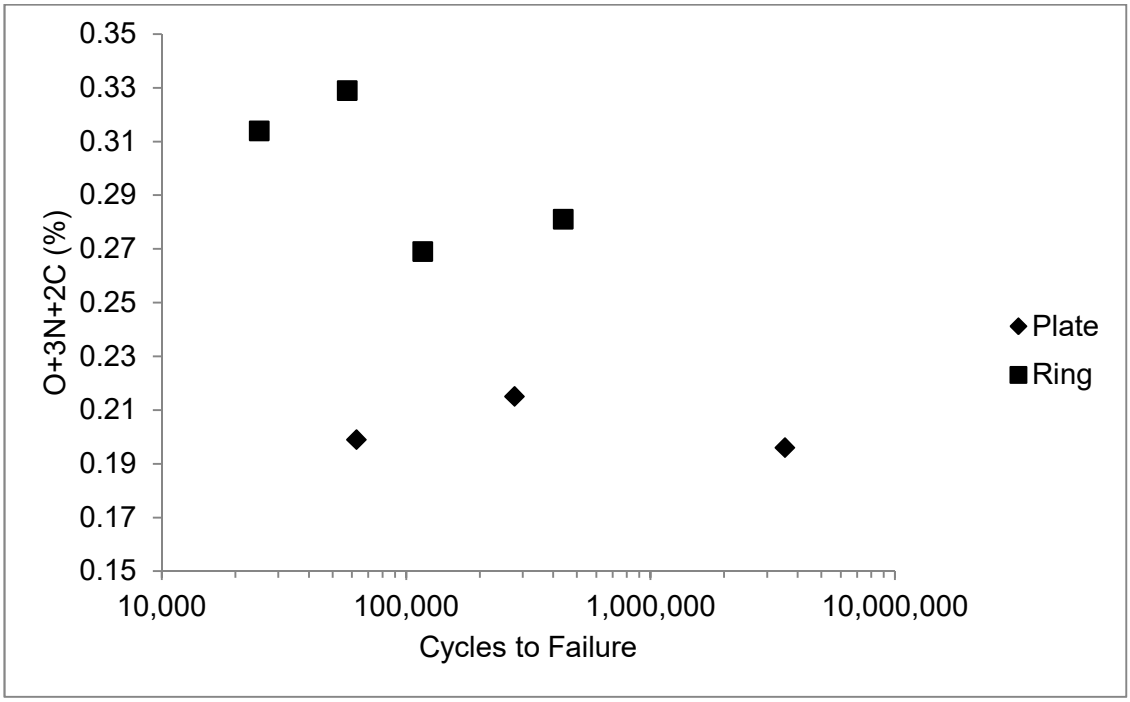

Figure 5.3: Oxygen equivalent versus cycles to failure.

Ivasishin et al. [55] had studied the effect of pore length on the fatigue endurance limit of HIPed BEPM Ti-6Al-4V having an elevated oxygen content compared to IM. The tensile strength was measured as 1020 – 1040 MPa, which is greater than IM (931 MPa [48]). They noted high oxygen and nitrogen (0.26 and 0.047 wt%) were likely responsible for achieving higher than expected static strength properties. Additionally, the endurance limit was found comparable to IM. They concluded the similarities in endurance limits was primarily driven by the β grain size of the PM versus IM, which for IM was much larger. The detriment of porosity combined with the benefit of a smaller β grain size was seen to counter balance one another. However, no conclusion was made as to whether the high oxygen content affected the endurance limit as it had with the

tensile properties. From the results of the present work, it remains inconclusive whether variations in solute strengthening may lessen or exacerbate the effect of a detrimental microstructure feature (porosity or primary α size / volume fraction) on HCF fatigue strength.

5.4 Effect of Texture on Fatigue

5.4.1 Observations on Texture

A clear difference in texture was observed between the samples that had the highest and lowest fatigue life. Recall these samples were extracted at different grain directions of the same forged ring. The sample having the highest fatigue life, L-A1, displayed a well dispersed, random distribution of HCP α grains. However, the sample with the lowest fatigue life, LT-A1, displayed banding of both the basal and prism planes. As these samples came from the same forging, it is believed the banding seen in LT-A1 is residual structuring from α+β upsetting and draw down. This dual-banding structure is believed to be caused by the final saddling operation exerting inconsistent wall reduction around the circumference of the ring, not realigning α grains in the primary forging direction or driving recrystallization. This is further supported by the swirling microstructure in Figure 4.3 having regions of primary α grains oriented with their long axis 90 degrees to one another. This structure would be expected after repeated upsetting and draw down operations where the forging direction is rotated 90 degrees. The banding observed demonstrates the ineffectiveness of saddling for fatigue critical

applications. However, the variation of texture achieved by saddle forging proved useful for the purpose of this study.

The banding, or macrozones, observed for LT-A1 agrees with the literature for being typical of bi-modal structured IM Ti-6Al-4V [14] [15] [16]. Banding of basal or prismatic planes, or certainly both in combination, would do little to resist crystallographic slip, and would promote a reduction in fatigue life. The increase in slip length from macrozones supports why L-A1, being devoid of macrozones, had an order of magnitude improvement in fatigue life than LT-A1. It is theorized that thermomechanical processing of fine grained sintered titanium alloys to eliminate macrozones can potentially lead to product that outperforms the fatigue performance of IM.

5.5 Correlation of Microstructure to Fracture Features

Cleavage fracture initiation seen on all but one fracture surface is typical of IM Ti-6Al-4V. Facets were shown to correlate with the size and shape of primary α for both product forms. The shift in crack initiation from surface to subsurface for samples with increasing fatigue life (beyond 60,000) cycles is also in agreement with the literature for IM Ti-6Al-4V [26]. The larger extent of cleavage fracture shown in Figure 4.23 and Figure 4.24 for samples having a lower fatigue life correlated to interconnected primary α. The lowest performing sample, LT-A1 shown in Figure 4.24, had the largest faceted region, believed to be a result of the swirling grain structure previously shown in Figure 4.3. Despite the primary α for the plate samples having a greater aspect ratio, it did not develop into

catastrophic facet formation, likely due to the lack of connectivity of heavily deformed primary α.

Only for one sample, L-C1 in Figure 4.21, did a crack initiate from a pore. This crack initiation was typical of castings or powder sintered and HIPed Ti-6Al-4V. No porosity was observed throughout the fracture surfaces of all other samples.

5.6 Digital Image Correlation

5.6.1 Global Strain Mapping

The observed global strain heterogeneity when strained below the yield stress is in agreement with the behaviour of IM Ti-6Al-4V [31]. The literature cited in Chapter 2 demonstrated that macrozones contribute to strain heterogeneity, with localized highly strained areas being larger than the macrozone size due to neighbouring effects. Variations of +/- 15 % in local strain reported in the literature for when IM Ti-6Al-4V is stressed to 356 MPa, measured by the photoelasticity method, is similar to that observed for cycles between 8,000 and 16,000 cycles, the maximum captured by DIC.

The diminishing magnitude of global strain heterogeneity should not be confused with a redistribution of strain at the micro level. While instantaneous global strain variations diminished in magnitude with increasing number of cycles, the micro strain continued to display inhomogeneity up to fracture. The mechanism for global strain redistribution was ultimately not identified, further study would be warranted.

5.6.2 Micro strain mapping

The ultimate goals for DIC were to determine whether pores had an effect on strain distribution, and whether a coarser microstructure having greater volume fraction of α grains resulted in similar or worsened strain inhomogeneity. Unfortunately, this could not be concluded for a number of reasons. Firstly, as the tracked sample surface was re-polished and etched for the final measurement, most porosity which was evident in prior fields had been polished through and was no longer visible. Secondly, the microstructure stochastic pattern and grey level did not have the spatial resolution necessary to resolve an area the size of pores. Setting of a fine facet size (8 μm resolution) resulted in abrupt 'jumps' in strain distribution correlating to the size of primary α grains. The jumps are believed to be false measurements from a best-fit approximation of the software for neighbouring facets. Increasing the facet size (20 μm resolution) resulted in a better perceived approximation of true strain distribution as there was greater overlap of neighbouring facets and less abrupt variations in strain (Figure 4.29). However, this resolution size was greater than the primary α size, and certainly greater than residual porosity. Finally, scratches on the sample surface from handling caused additional doubt when mapping at a fine resolution.

Despite the resolution limitations, the strain distribution following crack formation shown in Figure 4.29 (d) revealed repeating tensile and compressive bands forming in the direction of applied stress. These local strain inhomogeneities were up to +/- three times greater than the applied axial strain.

This is in agreement with DIC fatigue experiments of titanium alloys by Icoz [56] and Littlewood [57]. Icoz witnessed localized strain accumulations 3-4 times greater than the applied axial strain for a Ti-Al alloy having a lamellar and equiaxed α structure. Littlewood demonstrated localized strain nearly 6 times greater than the axial strain for mill annealed Ti-6Al-4V. By overlaying a Schmid factor map onto the strain map, Littlewood demonstrated hot spots as neighbouring α grains that had their c-axis parallel to the loading direction. Thus, a confirmation of the load shedding principle discussed in Chapter 2. This load shedding phenomenon is believed to apply equally for the current material being investigated as the mechanism for the development of local strain inhomogeneity. Linear bands crossing multiple primary α grains coincide with the observation of basal and prismatic banding and multi-faceted fatigue initiation on the fracture surface.

5.6.3 Effect of geometry of DIC

One of the objectives of DIC was to either confirm or disprove that crack initiation occurred by the same features as in IM Ti-6Al-4V, and whether porosity had an effect on crack initiation and growth. However, the specimen geometry and DIC sampling grid were inadequate to capture crack initiation and progression. Crack initiations favoured the radius of the gage length and could not be captured, despite rounded corners having a radius one-third the specimen thickness, and polishing to remove residual machining stresses. The specimen face for crack initiation also could not be controlled and progressed on the

opposite side being imaged during laboratory trials. Further, as the number of view fields needed to observe the full gage length was 22, it was impractical to create a grid to observe the gage length in its entirety.

An improvement in specimen geometry to try and best capture crack initiation and local strain at the crack tip is proposed in Figure 5.4. This geometry is based on ASTM E 606 [49] proportions of a continuous radius sample with the back and sides shot peened. Shot peening is intended to focus crack initiation on the observed face and away from the corners. Incorporating the high resolution imaging methods by Icoz et al. [56] and Littlewood [57] may further improve the accuracy of DIC measurements at the sub-grain level. DIC measurements using this geometry are presently ongoing and results may be featured in future work.

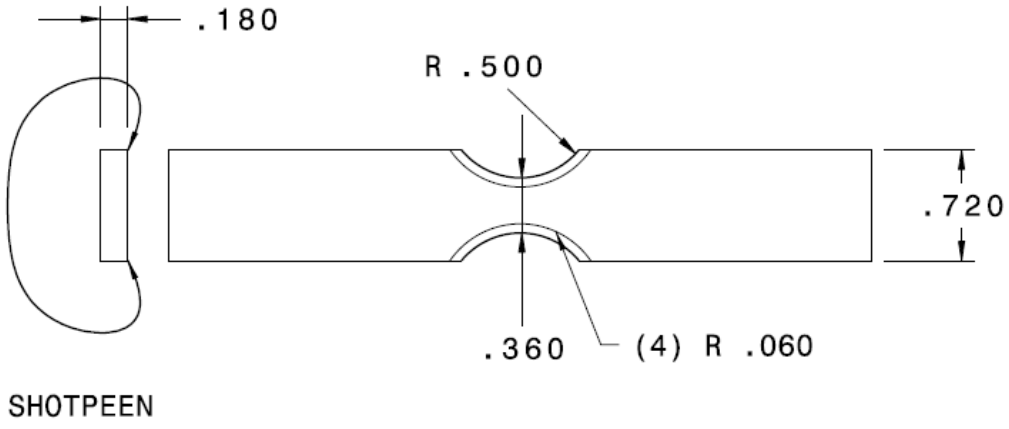

Figure 5.4: Drawing of flat continuous radius gage specimen for improved grain level interrupted DIC

5.7 Effect of Combinations of Predictors on Fatigue

5.7.1 Best Subsets Regression

In an attempt to correlate combinations of predictors on fatigue strength, a statistical software package was used to estimate which predictors to include in a multiple regression analysis. The number of variables input was limited to the number of observations on hand, as a result that incorporates an equal or greater number of variables as there are observations is statistically meaningless. Using Minitab (available from Minitab Inc.), a best subsets regression was performed for inputs of primary α volume fraction and width, number of primary α particles, OE, and pore length. These variables were chosen as they were identified in the literature for having a significant effect on fatigue, or were found to have trends that warranted further exploration. While texture was found to be significant, a texture parameter was not considered due to the difficulties in quantifying the observations from only the two measured samples, and to perform a texture analysis of all samples would have been cost prohibitive. The benefit of using a best subsets regression was the trial-and-error process of combining multiple predictors, and the regression weights, was automated. The chosen multiple regression equation was that which had the greatest fit (R^2 adj), significance (p-value) and predictive powers (R^2 pred and Mallow's Cp).

Results of best subsets regression in Appendix B show a two variable regression equation, incorporating primary α volume fraction and maximum pore length, was the most significant. The two regression equation had the lowest R^2

(pred) and Mallows' Cp, and a relatively high R^2 (adj). The R^2 (pred) and Mallows' Cp is a measure of the regression equation's ability to predict future responses. The R^2 (adj) is a measure of fit, much like R^2, but considers the number of predictors used, and thus serves as a more accurate comparison between multivariable regression equations having a different number of predictors.

A linear fit regression was performed on primary α volume fraction and pore length. Results of the linear fit regression in Appendix C show the result is statistically significant ($p<0.05$). Further, the two variable regression equation has a greater significance than primary α volume fraction alone ($p=0.012$ vs. $p=0.021$). Additionally, the p-value of the pore length term is significantly improved when coupled with volume fraction than when considered individually ($p=0.054$ vs. $p=0.552$). The regression weights given in Appendix C were multiplied into whole numbers, and shown in Figure 5.5 for reference, to arrive at the following multivariable regression equation for fatigue life:

$$Fatigue\ Index = D + 3.3V_f \quad (3)$$

Where D is the maximum pore length, V_f the primary α volume fraction and *Fatigue Index* an arbitrary label for the multivariable regression equation. The multivariable regression equation signifies that primary α volume fraction has a greater than three-fold influence on fatigue life than pore length. Further, an increase in either the pore diameter or primary α volume fraction would thus increase the *Fatigue Index* and lower cycles to failure, which is in keeping with fundamental thinking.

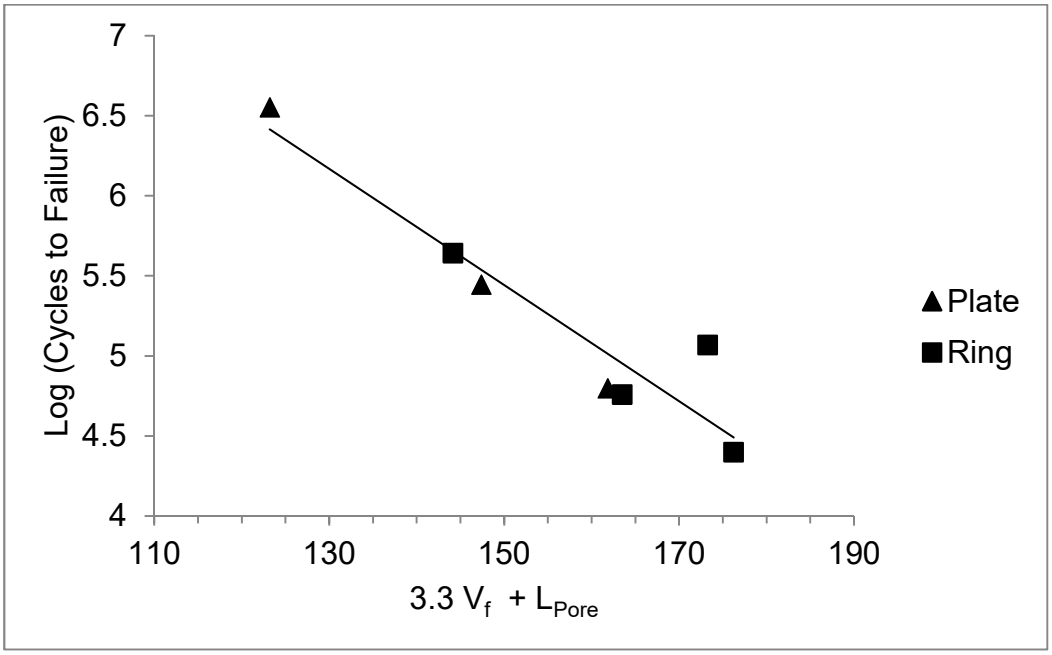

Figure 5.5: *Fatigue Index* versus log (cycles to failure). 29% < Primary α V_f < 47%, 18μm < Max. pore length < 50μm. R^2 = 83.4%, R^2 (adj) = 71.2%, p = 0.012.

5.7.2 Validation of the Multivariable Regression Equation

In Chapter 2, it was discussed for IM Ti-6Al-4V that primary α volume fraction (and/or the width) was the primary predictor on fatigue, while for HIPed or cast material, the pore size is the primary contributor. Although primary α volume fraction was the only standalone significant variable for this work, coupling both the primary α volume fraction and pore size resulted in an improved regression fit. This is partly intuitive, as the microstructure of the material studied can be considered to lie in between IM and castings: the pore size is small enough that primary α volume fraction dominates, although pores cannot be considered insignificant. This also supports the work of El-Soudani et al. [45] [46] [47] who proposed that microstructure refinement is as important as increasing

densification (decreasing pore size) to achieve acceptable fatigue life of forged BEPM Ti-6Al-4V.

The influence of primary α volume fraction on HCF of IM Ti-6Al-4V was studied by Wu et al. [19]. Their summary of 17 works related to fatigue of bi-modal microstructured IM Ti-6Al-4V, shown in Figure 5.6, revealed an optimum primary α volume fraction range of 30 – 50%, below or beyond which the fatigue life decreased. While not explicitly stated, the cause of the observed decrease in HCF with primary α volume fraction > 50% is related to an increase in slip length. This was supported by the observations in this thesis, whereby fracture surfaces with poor HCF had larger faceted regions, which correlated to their interconnected primary α grains acting as a single unit for slip. It was observed that interconnected primary α grains were typically associated with larger primary α volume fraction. However, the observation that HCF decreases with primary α volume fraction >30% suggested the proposed *Fatigue Index* may only be valid for the specific range studied (29 – 47%), and may not be linear for a wider range in volume fraction. Nonetheless, the observation by Wu et al. of a decrease in HCF for volume fractions ranging from 30 – 70% supports the finding of a linear trend of primary α volume fraction (29 – 47%) on HCF of the present study.

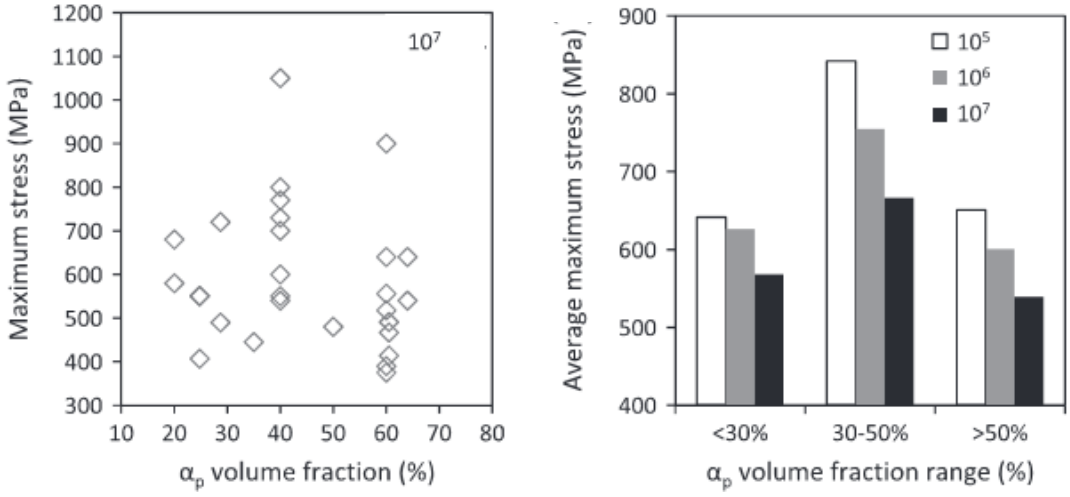

Figure 5.6: Summary of 17 studies on the effect of primary α volume fraction on HCF of bi-modal Ti-6Al-4V (R=-1 to 0.8). [19]

In an attempt to validate the proposed multivariable regression equation against existing works, image analysis of the bi-modal BEPM forged microstructures of El-Soudani et al. [46] [47] (Figure 2.11 and Figure 2.12) was performed. These photos were reduced in quality for the purpose of their original publication, which introduced error in measurement and thus the results could not be considered reliable. An inquiry was sent to the authors to obtain the original photos for the purpose of image analysis, but the originals were unavailable.

5.7.3 Suggested Improvements to the Multivariable Regression Equation

The primary α volume fraction term in the proposed multivariable regression equation was shown to be in agreement with existing literature on bi-modal microstructured IM. However, Lutjering and Williams [3] demonstrated a difference of 100MPa in the endurance limit of a bi-modal microstructured alloy having similar primary α volume fraction. The microstructures and resulting S-N

curve are shown in Figure 5.7 for reference. It can be observed the size of primary α particles is profoundly different, with a microstructure of fine and numerous particles having a higher endurance limit than larger particles that are larger and less in number. Wu et al. [19] reported similar findings on size of primary α particles, whereby larger particles decreased HCF as shown in Figure 5.8. However, the size of primary α particles (width) for the present study (for the limited range in primary α sizes available) was proven not to have a significant relation to fatigue life, whether considered solely or in combination with other variables. Thus, additional parameters may be influential on fatigue than that proposed in the *Fatigue Index* multivariable regression equation.

Due to the limited sample size, the validity of the proposed *Fatigue Index* multivariable regression equation is limited. Ideally, a study which could isolate and change individual parameters, or inclusion of a significantly larger sample size having different combination of variables, would be ideal to arrive at a unifying model for fatigue life. However, as the goal of the study was to identify the cause of the poor fatigue properties when compared to IM, the study was limited to the material provided.

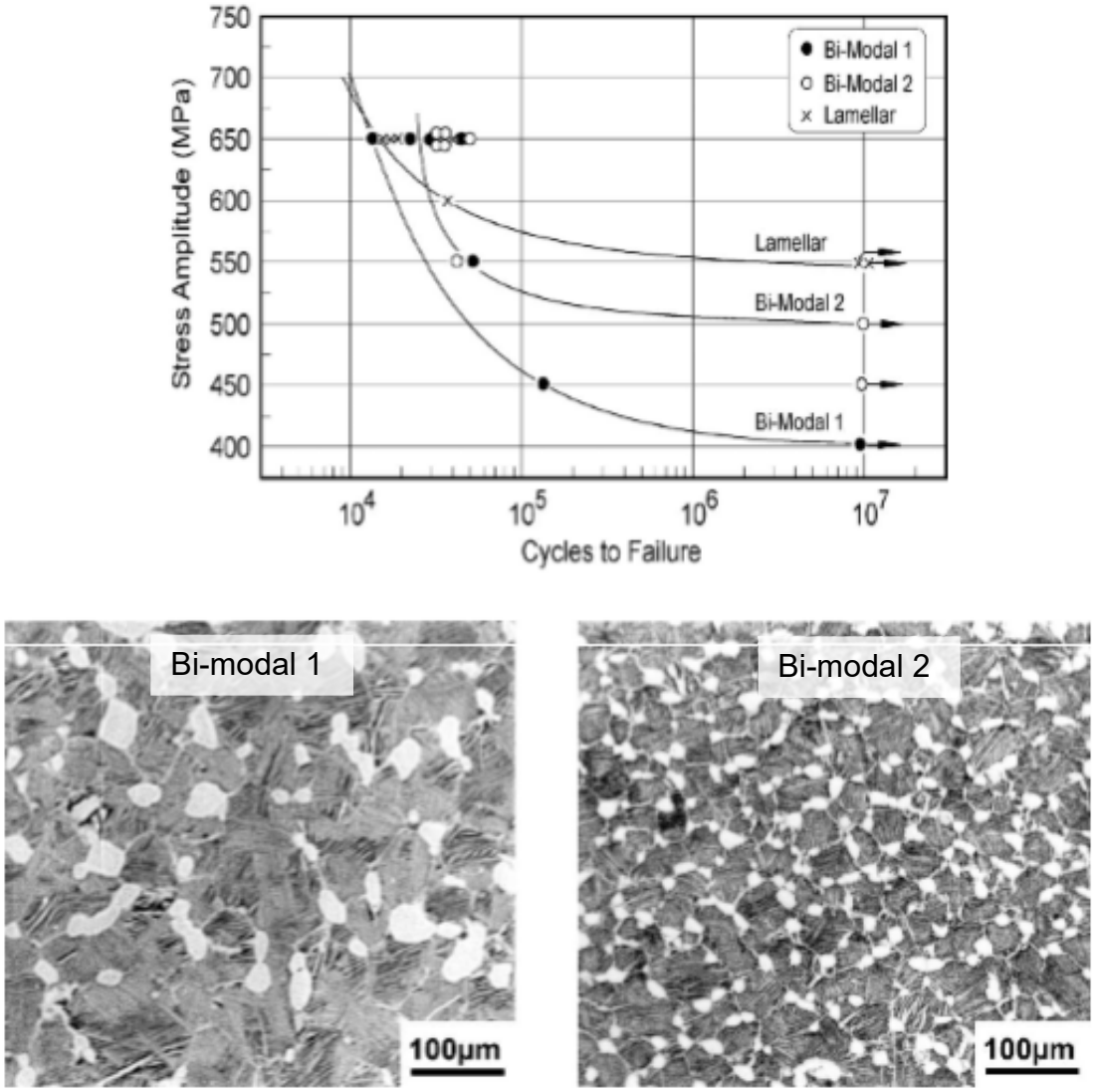

Figure 5.7: Effect of primary α grain size on HCF (R=-1) for α+β alloy IMI 834 with similar volume fraction having coarse (bi-modal 1) and fine (bi-modal 2) primary α grains [3]

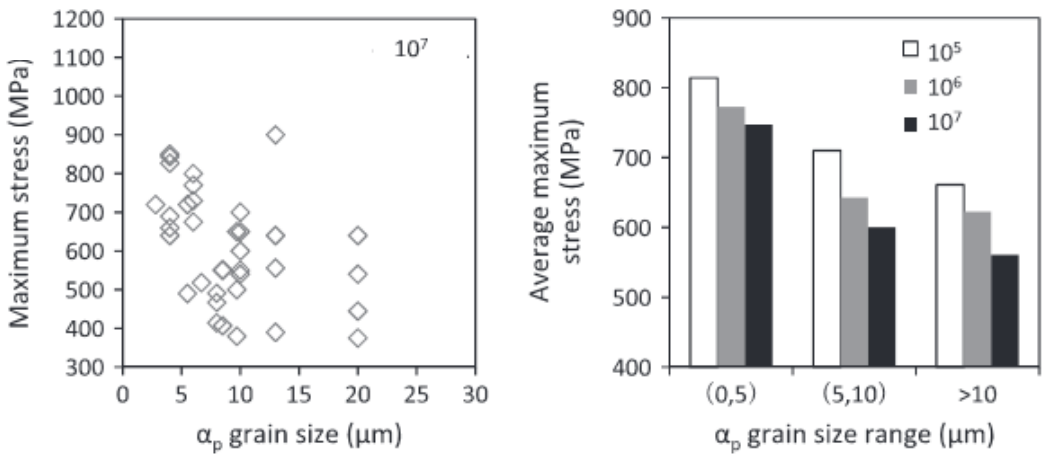

Figure 5.8: Summary of 17 studies on the effect of primary α grain size on HCF of bi-modal Ti-6Al-4V (R=-1 to 0.8). [19]

It is suggested by the author that a model incorporating a primary α quantity term (N) and OE term, in addition to primary α volume fraction and pore diameter, may better fit a larger data set. A primary α quantity term may better reflect observations in the literature on primary α particle size (i.e. V_f / N) on HCF strength. Inclusion of such a term may better fit a larger data set by being a better representation of the slip length. Regarding an OE term, Lutjering and Williams [3] stated increases in OE will increase HCF strength, and decrease LCF strength. As the majority of failure cycles in the present work were within the LCF regime, despite a low strain level, the observation in Figure A.8 of a decrease in OE generally favouring a higher fatigue life is supported by the literature. Thus, a model incorporating an OE and N term may better fit a larger data set than the proposed *Fatigue Index*.

5.7.4 Summary

This work proposes a multivariable regression equation of two predictors, primary α volume fraction and pore diameter, with an improved statistical significance (p-value) and trend fit than the most significant individual term: primary α volume fraction. A summary on the significance of fit for each is shown in Table 5.1.

Table 5.1: Summary of Linear Regressions for Volume Fraction and *Fatigue Index*

	R^2 (%)	R^2 (adj) (%)	p-value
Volume Fraction	68.7	62.4	0.021
Fatigue Index	83.4	71.2	0.012

The improved fit and significance of the multivariable regression equation supports the hypothesis that fatigue life is not controlled by one parameter alone. Further, that primary α volume fraction and pore size have a coupled influence on fatigue life. Consideration of porosity alone was not a reliable predictor of fatigue. The heavier weighting on primary α volume fraction than porosity (3.3:1), in addition to the combined effect of both parameters on fatigue life, demonstrate the detrimental effect of pores can be overcome by a refined microstructure.

Due to the limited number of observations available, further study would be needed to validate the multivariable regression equation. Nonetheless, the intuitive meaning of the multivariable regression equation, being a hybrid of primary contributors on fatigue for fully dense IM and porous material, appears

logical as the microstructure could be considered a hybrid of cast and wrought material.

A model incorporating additional terms, namely OE and number of primary α particles, may result in an improvement fit for a larger HCF dataset. It is noted in Appendix B that a four-term multivariable regression equation incorporating primary α volume fraction, width, OE and pore diameter, had the second best fit. However, no significance can be made regarding a four-term multivariable regression equation from the seven observations available. The suggestion to include these terms serves as guidance for future experiments.

CHAPTER 6: CONCLUSION

Strain controlled fatigue testing ranging from 0.325 - 0.350 % strain was conducted on BEPM Ti-6Al-4V to identify the primary predictor(s) on fatigue life. Two product forms were analyzed: forged ring and hot rolled plate. SEM analysis of the fatigue fracture surfaces revealed longer fatigue lives were associated with crack initiation at a single facet, and in one instance a pore, while shorter fatigue lives were associated with larger and more numerous facets. Optical microscopy correlated the size of facets to the size of primary α particle(s). Texture analysis (EBSD) revealed a strong basal and prismatic crystal orientation of HCP α (macrozones) near the fracture initiation site of the sample with the lowest cycle count, while the sample with the longest life had a well dispersed crystal orientation of HCP α.

DIC revealed global strain redistribution as cycling progressed, beginning with a random strain distribution to a more uniform distribution. Local micro-strain heterogeneities developed early on in fatigue cycling and continued to progress in magnitude up to three times the applied strain.

A variety of microstructural features were measured for each sample by optical microscopy. Notable observations were primary α volume fraction (29 – 47%) and maximum pore length (18 – 50 μm). A pore size of 50 μm was sufficient to promote crack nucleation, while pores smaller in size did not nucleate a fatigue crack. Analysis of carbon, oxygen and nitrogen for the determination of the oxygen equivalent (OE) revealed a range of 0.20 – 0.33 %.

The single most critical variable on fatigue crack nucleation was determined as primary α volume fraction. A multivariable regression equation for fatigue using two predictors, primary α volume fraction and maximum pore size, was proposed based on statistical analysis. The coefficients of the multivariable regression equation indicate that primary α volume fraction has an 3.3x greater effect on HCF strength than pore size. Further, the multivariable regression equation demonstrated the detrimental effects of porosity can be overcome by controlling the primary α volume fraction. Due to the limited number of observations, the validity of the multivariable regression equation for other literature data or parameters/values outside those tested cannot be stated with certainty.

Due to the limited number of observations, careful consideration was given not to propose a multivariable regression equation with a large number of terms. It is recommended future experimentation still consider number of primary α particles / primary α width and OE, in addition to primary α volume fraction and maximum pore size, to determine a model for HCF of BEPM Ti-6Al-4V.

REFERENCES

[1] R. R. Boyer, “Titanium for aerospace: rationale and applications”, *Advanced Performance Materials*, vol. 2, 1995, pp. 349-368.

[2] S. A. Kasparov, A. G. Klevtsov, A. I. Cheprasov, et al., “Semi-continuous magnesium-hydrogen reduction process for manufacturing of hydrogentated, purified titanium powder,” United States Patent US 8 007 562 B2, Aug. 30, 2011.

[3] G. Lutjering, J. C. Williams, *Titanium*, 2nd ed. New York, Springer, 2007, ch. 2 & ch. 5, pg. 24, 208-211.

[4] I. Weiss, S.L. Semiatin, “Thermomechanical processing of alpha titanium alloys – an overview,” *Materials Science Engineering A263*, 1999, pp. 243-256.

[5] P.J. Bania, “Beta titanium alloys and their role in the titanium industry,” *JOM*, Jul. 1994, pp.16-17.

[6] H.M. Flower, “Microstructural development in relation to hot working of titanium alloys,” *Material Science Technology*, vol. 6, 1990, pp. 1082–1092.

[7] M. Abdel-Hady Gepreel. (2013). “Texturing tendency in β-type Ti-alloys” in *Recent developments in the Study of Recrystallization*, P. Wilson (Ed.), InTech, ch. 4, DOI: 10.5772/53588.

[8] M. J. Donachie, Jr., “Understanding Ti’s Metallurgy” in *Titanium: A Technical Guide*, 1st ed. Ohio, ASM International, 1988, ch. 3, pg. 27.

[9] S.L. Semiatin, V. Seetharaman, I. Weiss, “The thermomechanical processing of alpha/beta titanium alloys,” *JOM*, June 1997.

[10] F. H. Froes, ed., “Principles of beta transformation and heat treatment of titanium alloys,” in *Titanium-Physical Metallurgy, Processing and Applications, 1st ed.* Ohio, ASM International, 2015, ch. 4, pg 80.

[11] G. Lutjering, “Influence of processing on microstructure and mechanical properties of (alpha + beta) titanium alloys,” *Materials Science Engineering A243*, 1998, pp. 32-45.

[12] M. Peters, A. Gysler, G. Lutjering, “Influence of texture on fatigue properties of Ti-6Al-4V,” *Metallurgical Transactions A*, vol. 15A, November 1983, 1597 – 1605.

[13] S. Balasubramanian, L. Anand, “Plasticity of initially textured hexagonal polycrystals at high homologous temperatures: application to titanium,” *Acta Materialia*, vol. 50, 2002, pp. 133-148.

[14] F. Bridier, P. Villechaise, J. Mendez, “Slip and fatigue crack formation processes in an α/β titanium alloy in relation to crystallographic texture on different scales,” *Acta Materialia*, vol. 56, 2008, pp 3951 – 3962.

[15] I. Bantounas, T. C. Lindley, D. Rugg, et al., “Effect of microtexture on fatigue cracking in Ti-6Al-4V,” *Acta Materialia*, vol. 55, 2007, pp 5655-5665.

[16] K. L. Biavant, S. Pommier, C. Prioul, “Local texture and fatigue crack initiation in a Ti-6Al-4V titanium alloy,” *Fatigue Fract Enging Mater Struct*, vol. 25, 2002, pp. 527-545.

[17] W. Cui, “A state-of-the-art review on fatigue life prediction methods for metal structures,” *J Mar Sci Technol*, vol. 7, 2002, pp. 43 – 56.

[18] S. D. Henry et al., Eds. “Ti-6Al-4V,” in *Fatigue Data Book: Light Structural Alloys*, 1st ed. Materials Park, OH: ASM International, 1995, pp 271-303.

[19] G. Q. Wu, C.L. Shi, A.X. Sha, H.R. Jiang, “Effect of microstructure on the fatigue properties of Ti-6Al-4V titanium alloys,” *Materials and Design*, vol. 46, 2013, pp. 668-674.

[20] J. J. Lucas, P. P. Konieczny, “Relationship between alpha grain size and crack initiation fatigue strength in Ti-6Al-4V,” *Metallurgical Transactions*, vol. 2, 1971, pp. 911-921.

[21] M. A. Imam, C. M. Gilmore, “Fatigue and microstructural properties of quenched Ti-6Al-4V,” *Metallurgical Transactions A*, vol. 14A, 1983, pp. 233-240.

[22] R. K. Nalla, B. L. Boyce, J.P. Campbell, et al. “Influence of microstructure on high-cycle fatigue of Ti-6Al-4V: Bimodal vs. lamellar structures,” *Metallurgical and Materials Transactions A*, vol. 33A, March 2002, pp. 899-918.

[23] J. Sieniawski, W. Ziaja, K. Kubiak, et al., “Microstructure and mechanical properties of high strength two-phase titanium alloys”, Chapter 4 Titanium alloys – Advances in Properties Control, http:/dx.doi.org/10.5772/56197.

[24] C. P. Przybyla, D. L. McDowell, “Simulated microstructure-sensitive extreme value probabilities for high cycle fatigue for bi-modal Ti-6Al-4V,” *International Journal of Plasticity*, 2001, pp. 1871-1895.

[25] A.N. Stroh, “The formation of cracks as a result of plastic flow,” *Proc Roy Soc Lond*, vol. 233, 1954, pp. 404-414.

[26] J.H. Zuo, Z.G. Wang, E.H. Han, “Effect of microstructure on ultra-high cycle fatigue behaviour of Ti-6Al-4V,” *Matls Sci and Eng A*, 473, 2008, 147-152.

[27] C.A. Stubbington, A.W. Bowen, “Improvements in the fatigue strength of Ti-6Al-4V through microstructure control,” *Journal of Materials Science*, vol. 9, 1974, pp. 941-947.

[28] M. R. Bache, “Processing titanium alloys for optimum fatigue performance,” *International Journal of Fatigue*, vol. 21, 1999, pp. S105-S111.

[29] M. R. Bache, W. J. Evans, “Impact of texture on mechanical properties in an advanced titanium alloy,” *Materials Science and Engineering A*, 2001, pp. 409-414.

[30] I. Bantounas, D. Dye, T. Lindley, “The role of microtexture on the faceted fracture morphology in Ti-6Al-4V subjects to high-cycle fatigue,” *Acta Materialia*, vol. 58, 2010, pp. 3908-3918.

[31] K. Le Biavant, S. Oimmier, C. Prioul, “Local texture and fatigue crack initiation in a Ti 6Al-4V titanium alloy,” *Fatigue Fract Engng Mater Struct*, 25, pp. 527-545.

[32] H. R. Ogden, R. I. Jaffee, “The effects of carbon, oxygen, and nitrogen on the mechanical properties of titanium and titanium alloys,” Battelle Memorial Institute, Columbus, Ohio, Report No. 20, October 1955.

[33] D. Harwig, W. Ittiwattana, H. Castner, “Advances in oxygen equivalent equations for predicting the properties of titanium welds,” *Welding Research Supplement*, May 2011, pp. 126-136.

[34] Z. Liu, G. Welsh, “Effects of oxygen and heat treatment on the mechanical properties of alpha and beta titanium alloys,” *Metallurgical Trans A*, vol. 19A, March 1988 pp 557- 542.

[35] F. H. Froes and D. Eylon, “Powder metallurgy of titanium alloys – a review,” in: F. H. Froes, D. Eylon, and H. B. Bomberger (Eds.), *Titanium Technology*: *Present Status and Future Trends*, Warrendale (1985), pp. 49– 59.

[36] O. M. Ivasishin, K. A. Bondareva, V. I. Bondarchuk, et al., “Fatigue resistance of powder metallurgy Ti-6Al-4V Alloy,” *Strength of Materials*, vol. 36, no. 4, 2004, 225-230.

[37] W. J. Evans, “Optimizing mechanical properties in alpha + beta titanium alloys,” *Materials Science and Engineering A243*, pp. 89-96, 1998.

[38] F. Cao, P. Kumar, M. Koopman, et al., “Understanding competing fatigue mechanisms in powder metallurgy Ti-6Al-4V alloy: Role of crack initiation and duality of fatigue response,” *Matls Sci Eng A*, vol. 630, 2015, pp. 139-145.

[39] Y. Yan, G. L. Nash, P. Nash, “Effect of density and pore morphology on fatigue properties of sintered Ti-6Al-4V,” *International Journal of Fatigue*, vol. 55, 2013, pp. 81-91.

[40] F. H. Froes, D. Eylon, “Powder metallurgy of titanium alloys,” *International Materials Reviews*, vol. 35, no. 3, 1990, pp. 192 – 184.

[41] V. Moxson, P. Sjoblom, M. Trzcinski, “Ti-6Al-4V properties achieved via extra low chlorine titanium powder,” *Advances in Powder Metallurgy*, vol. 6, 1992, pp. 125-140.

[42] K. Zhang, J. Mei, N. Wain, et al., “Effect of hot-isostatic-pressing parameters on the microstructure and properties of powder Ti-6Al-4V hot-isostatically-pressed samples,” *Metallurgical Materials Trans A*, vol. 41A, April 2010, pp. 1033-1045.

[43] R. Guo, et al., “Microstructure evolution and mechanical properties of powder metallurgy Ti-6Al-4V alloy based on heat response,” Materials Science Engineering A, vol. 639, 2015, pp. 327-334.

[44] C. Lavender, V. Joshi, A. Devaraj et al., “Recent progress in the development of titanium alloys processed using low cost ADMA TiH2 powder,” in *Proc. TMS 2013*, San Antonio: Texas, March 2013.

[45] S. M. El-Soudani, K. Yu, E. M. Crist, el. al. “Optimization of blended-elemental powder-based titanium alloy extrusion for aerospace applications,” *Metallurgical and Materials Trans A*, vol. 44A, February 2013, pp. 899-910.

[46] S. M. El-Soudani, J. Fanning, M. Harper, et al. “Rolled product form development and optimization using blended-elemental powder-based billets of Ti-6Al-4V alloy,” in *Proc. Aeromat 2012*, Charlotte: North Carolina, June 2012.

[47] S. M. El-Soudani, K. Yu, E. M. Crist, et al. “Development and optimization of rolled product forms using blended-elemental powder-based Ti-6Al-4V,” in *Proc. Aeromat 2012*, Charlotte: North Carolina, June 2012.

[48] *Titanium alloy sheet, strip and plate, 6Al – 4V, annealed*, SAE Aerospace Standard AMS 4911 L, Jun 2007.

[49] *Standard Test Method for Strain Controlled Fatigue*, ASTM Standard E 606-12, September 2012.

[50] *Standard Test Methods for Tension Testing of Metallic Materials*, ASTM Standard E 8-04, April 2004.

[51] A. El Bartali, V. Aubin, S. Degallaix, “Fatigue damage analysis in a duplex stainless steel by digital image correlation technique,” *Fatigue Fracture Engineering Materials Structures*, 2008, pp. 137-151.

[52] M. A. Sutton, J. Orteu, H. W. Schreier, *Image correlation for shape, motion and deformation measurements*, 1st ed. Springer, New York, 2009.

[53] *Standard Test Method for Determination of Hydrogen in Titanium and Titanium Alloys by Inert Gas Fusion Thermal Conductivity/Infrared Detection Method*, ASTM Standard E 1447-09, March 2009.

[54] *Standard Test Method for Determination of Oxygen and Nitrogen in Titanium and Titanium Alloys by the Inert Gas Fusion Technique*, ASTM Standard E 1409-13, 2013.

[55] O.M. Ivasishin et al., “Fatigue resistance of powder metallurgy Ti-6Al-4V alloy,” *Strength Materials*, vol. 36, no. 4, 2004, pp. 225-230.

[56] C. Icoz, L. Patriarca, M. Filippini, et al., “Strain accumulation in TiAl intermetallics via high-resolution digital image correlation (DIC)”, *Procedia Engineering*, vol. 74, 2014, pp. 443-448.

[57] P. D. Littlewood, A.J. Wilkinson, “Local deformation patterns in Ti-6Al-4V under tensile, fatigue and dwell fatigue loading,” *International Journal of Fatigue*, vol. 43, 2012, pp. 111-119.

APPENDIX A: REGRESSION ANALYSES

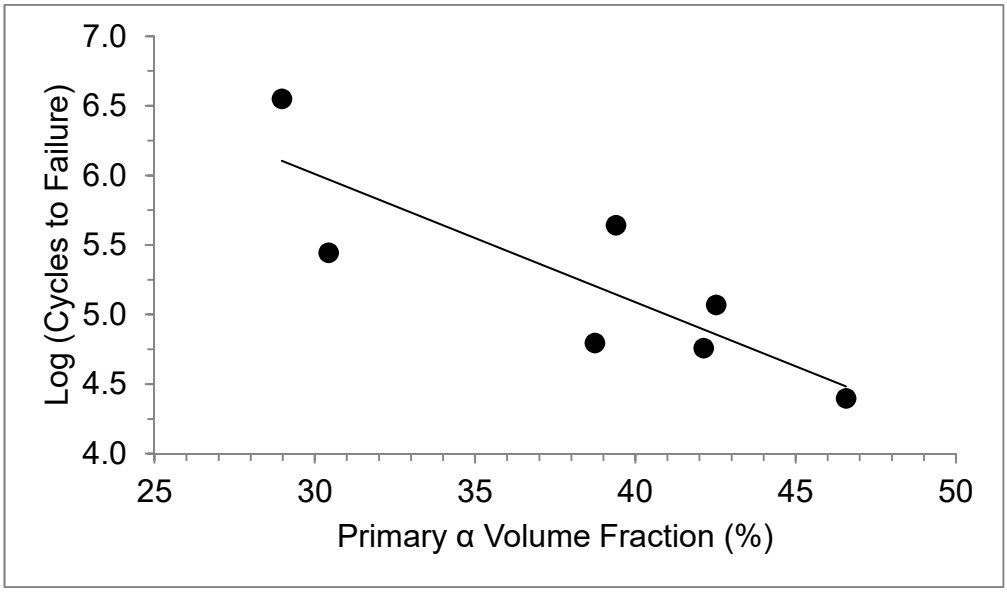

Figure A.1: Percent area of primary α versus cycles to failure. R^2 = 68.7%, R^2 (adj) = 62.4%, p = 0.021.

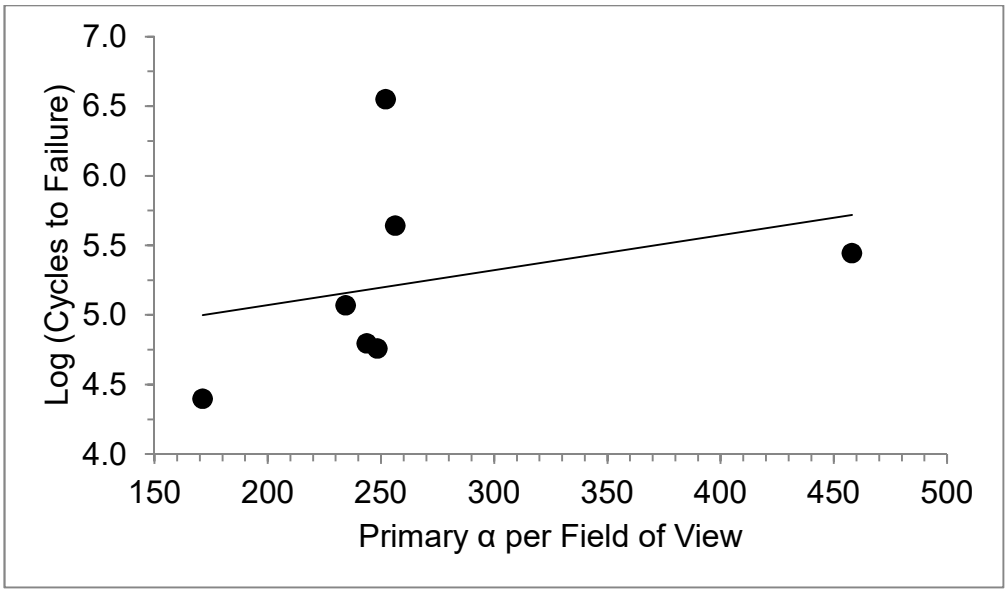

Figure A.2: Quantity of primary α per individual view field versus cycles to failure. R^2 = 9.9%, R^2 (adj) = 0.0%, p = 0.492

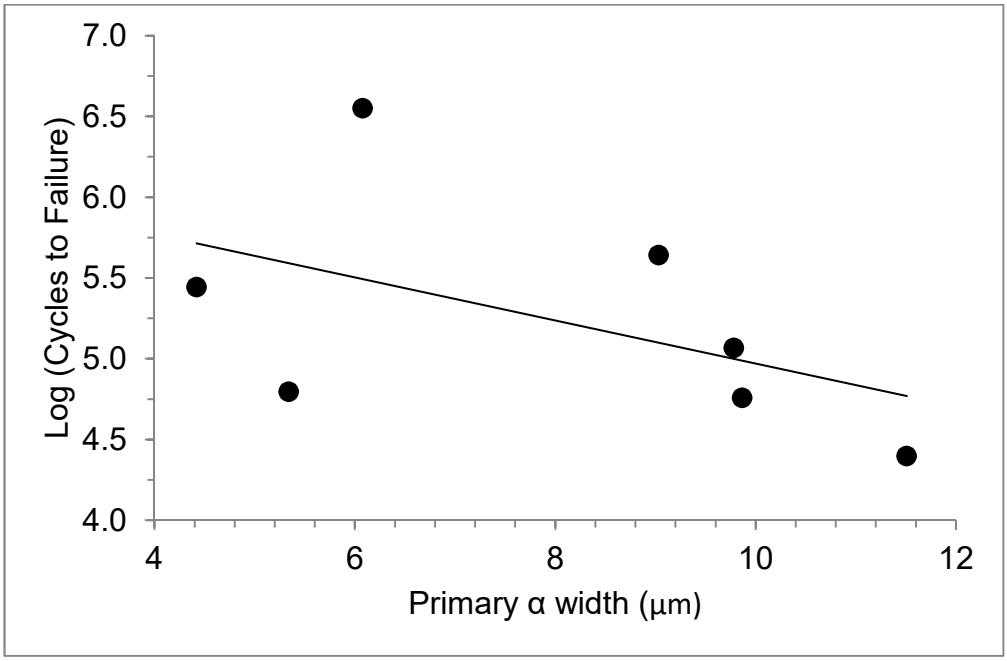

Figure A.3: Primary α width versus cycles to failure. R^2 = 25.1%, R^2 (adj) = 10.1%, p = 0.252.

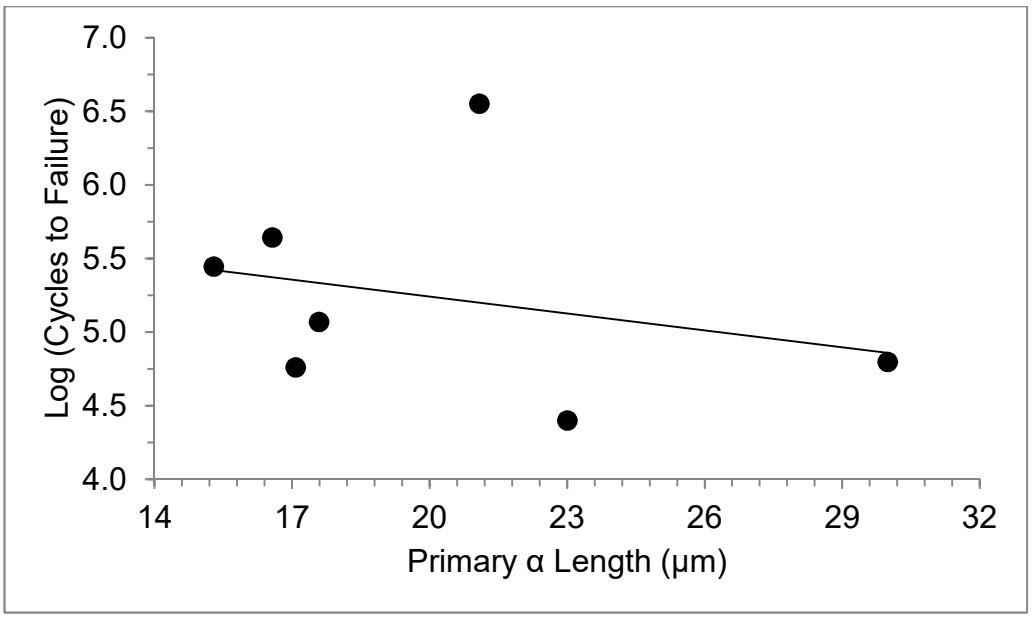

Figure A.4: Primary α length (ellipse major diameter) versus cycles to failure. R^2 = 7.5%, R^2 (adj) = 0.0%, p = 0.552.

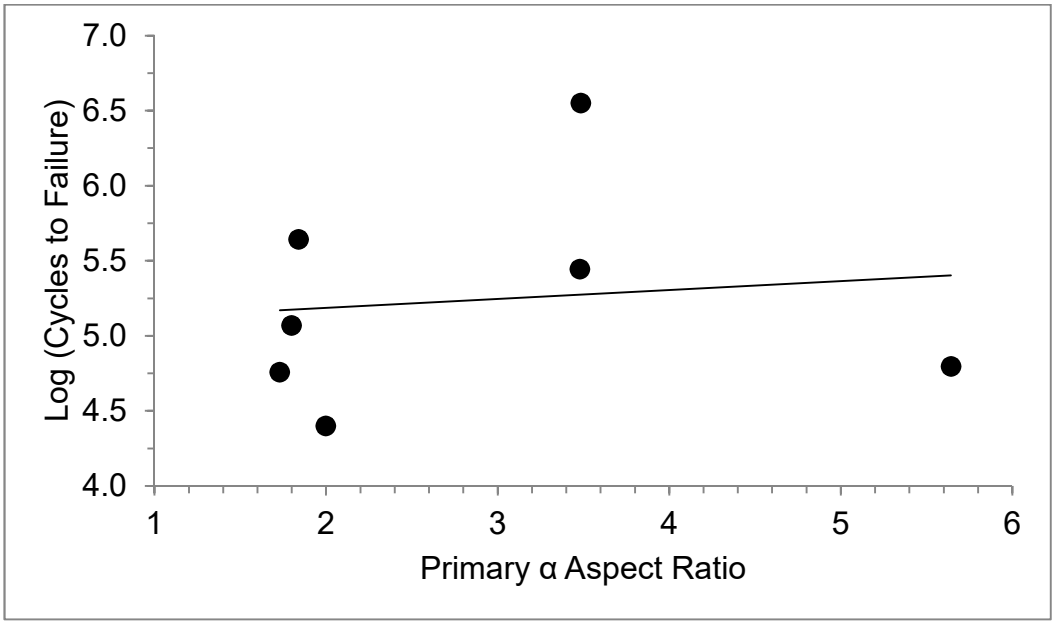

Figure A.5: Aspect ratio versus cycles to failure for forged ring and rolled plate. R^2 = 1.4%, R^2 (adj) = 0.0%, p = 0.798

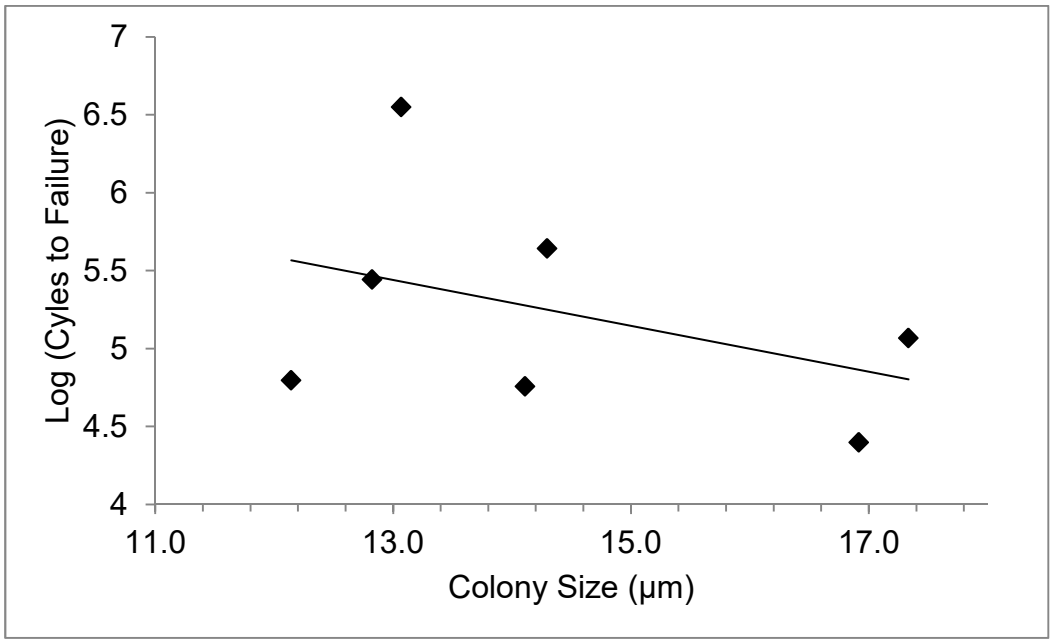

Figure A.6: Colony size per individual view field versus cycles to failure. R^2 = 17.1%, R^2 (adj) = 0.5%, p = 0.357

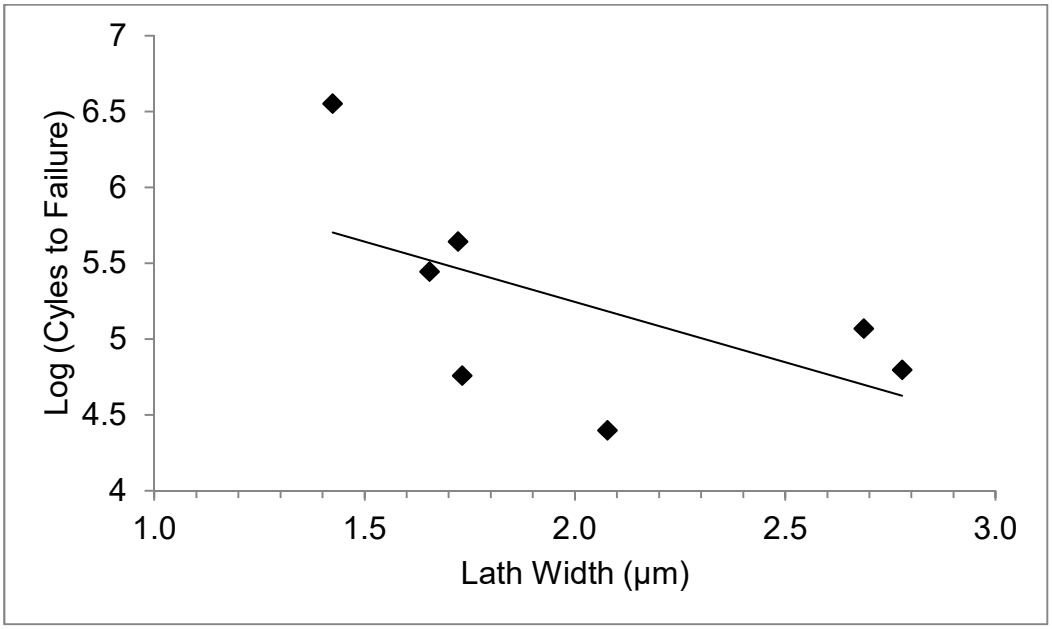

Figure A.7: Lamella width per individual view field versus cycles to failure. R^2 = 9.6%, R^2 (adj) = 0.0%, p = 0.500

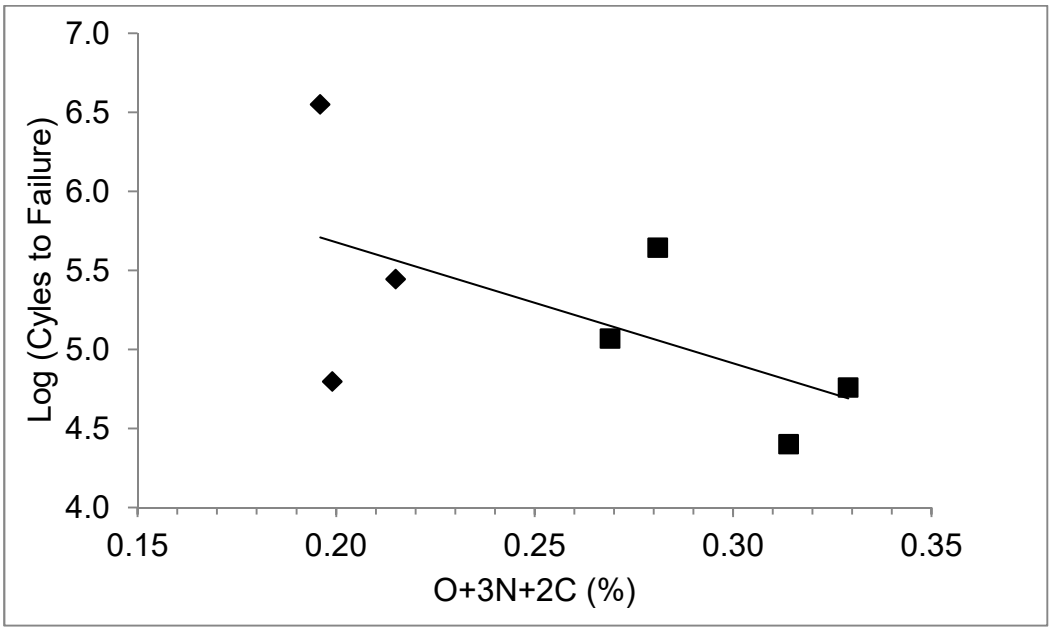

Figure A.8: Oxygen equivalent versus log(cycles to failure). R^2 = 34.2%, R^2 (adj) = 21.0%, p = 0.168.

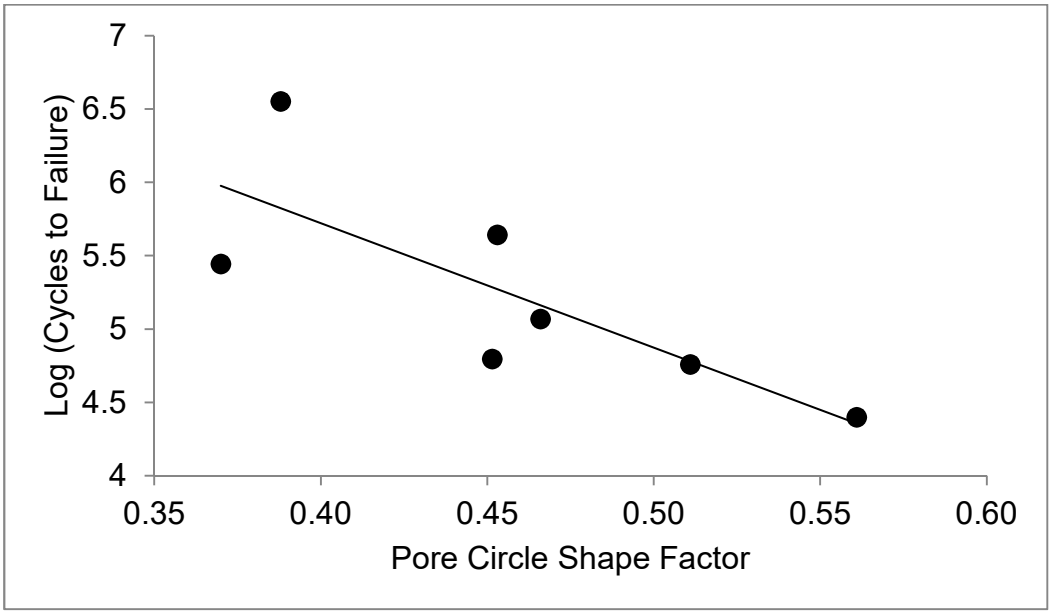

Figure A.9: Pore shape factor versus log(cycles to failure). R^2 = 61.2%, R^2 (adj) = 53.4%, p = 0.038.

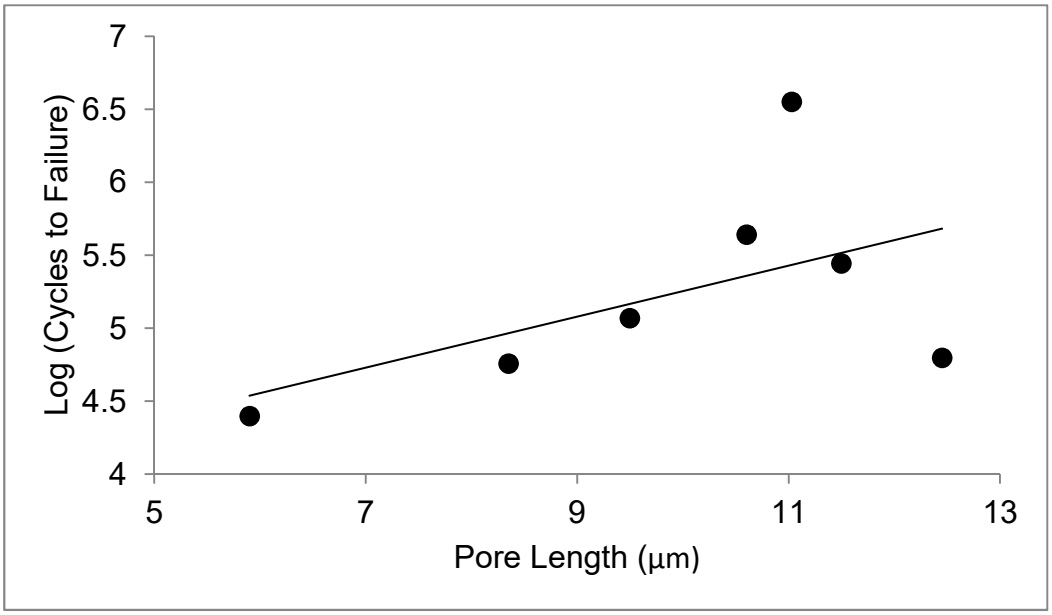

Figure A.10: Pore median length (major ellipse diameter) versus log(cycles to failure). R^2 = 29.1%, R^2 (adj) = 14.9%, p = 0.211.

APPENDIX B: BEST SUBSETS REGRESSION ON FATIGUE LIFE

The data below is the result of a best subset regression analysis, as output by Minitab. Variables input were the primary α volume fraction (Vol f), number of primary α particles (N), primary α width (Alpha W), oxygen equivalent (OE) and maximum pore length (Max Pore L). Each row represents an expression. The left most column indicates how many variables are included in the tested expression. The 'X's in the right most columns indicate which variables are included in the expression. The highlighted row (two variable regression; primary α volume fraction and maximum pore length) is the most significant of all combinations, on the basis of having the highest R-Squared (predictive) and relatively high R-Square (adjusted) values.

Best Subsets Regression: Log NF versus Vol f, N, Alpha W, OE, Max Pore L

Response is Log NF

Vars	R-Sq	R-Sq (adj)	R-Sq (pred)	Mallows Cp	S	Vol f	N	Alpha W	OE	Max Pore L
1	68.7	62.4	27.4	8.4	0.43954	X				
1	34.2	21.0	0.0	21.1	0.63737				X	
2	88.9	83.4	71.2	3.0	0.29221	X				X
2	85.6	78.4	32.5	4.3	0.33339	X		X		
3	92.3	84.6	64.4	3.8	0.28152	X		X		X
3	91.0	82.0	60.3	4.3	0.30409	X		X	X	
4	96.5	89.5	65.3	4.3	0.23196	X		X	X	X
4	93.4	80.2	0.0	5.4	0.31896	X	X	X		X
5	97.3	83.6	0.0	6.0	0.29046	X	X	X	X	X

APPENDIX C: MULTIVARIABLE REGRESSION ANALYSIS ON FATIGUE LIFE

The data below is the result of the linear multivariable regression analysis for primary α volume fraction (Vol f) and maximum pore length (Max Pore L), as output by Minitab. Fatigue cycles-to-failure (NF) were log transformed.

Regression Analysis: Log NF versus Vol f, Max Pore L

Analysis of Variance

Source	DF	Adj SS	Adj MS	F-Value	P-Value
Regression	2	2.7442	1.37208	16.07	0.012
Vol f	1	2.7389	2.73890	32.08	0.005
Max Pore L	1	0.6244	0.62443	7.31	0.054
Error	4	0.3416	0.08539		
Total	6	3.0857			

Model Summary

S	R-sq	R-sq(adj)	R-sq(pred)
0.292213	88.93%	83.40%	71.23%

Coefficients

Term	Coef	SE Coef	T-Value	P-Value	VIF
Constant	10.86	1.06	10.29	0.001	
Vol f	-0.1161	0.0205	-5.66	0.005	1.24
Max Pore L	-0.0355	0.0131	-2.70	0.054	1.24

Regression Equation

Log NF = 10.86 - 0.1161 Vol f - 0.0355 Max Pore L

Regression Analysis: Log NF versus Fatigue Index

```
The regression equation is
Log NF = 10.86 - 0.03551 Fatigue Index


S = 0.261364   R-Sq = 88.9%   R-Sq(adj) = 86.7%


Analysis of Variance

Source       DF       SS       MS      F      P
Regression    1  2.74416  2.74416  40.17  0.001
Error         5  0.34156  0.06831
Total         6  3.08572
```

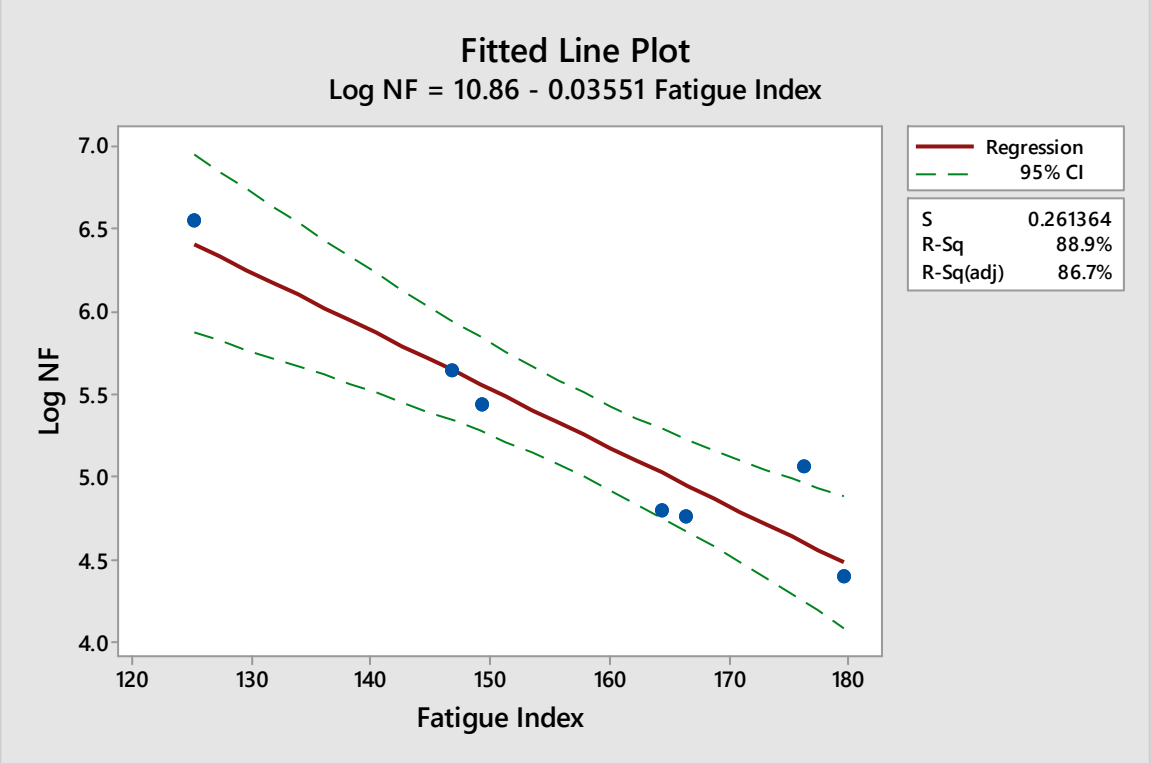

Figure C.1: Linear regression on Fatigue Index with upper and lower 95% confidence interval limits